

**GROWTH AND CHARACTERIZATION OF III-NITRIDE
SEMICONDUCTORS FOR HIGH-EFFICIENT LIGHT-EMITTING
DIODES BY METALORGANIC CHEMICAL VAPOR DEPOSITION**

A Ph.D Dissertation
Presented to
The Academic Faculty

by

Jeomoh Kim

In Partial Fulfillment
of the Requirements for the Degree
Doctor of Philosophy in the
School of Electrical and Computer Engineering

Georgia Institute of Technology
August 2014

Copyright © 2014 by Jeomoh Kim

**GROWTH AND CHARACTERIZATION OF III-NITRIDE
SEMICONDUCTORS FOR HIGH-EFFICIENT LIGHT-EMITTING
DIODES BY METALORGANIC CHEMICAL VAPOR DEPOSITION**

Approved by:

Dr. Russell D. Dupuis, Advisor
School of Electrical and Computer
Engineering
Georgia Institute of Technology

Dr. Shyh-Chiang Shen
School of Electrical and Computer
Engineering
Georgia Institute of Technology

Dr. Oliver Brand
School of Electrical and Computer
Engineering
Georgia Institute of Technology

Dr. Douglas P. Yoder
School of Electrical and Computer
Engineering
Georgia Institute of Technology

Dr. Jae-Hyun Ryou
Department of Mechanical
Engineering
University of Houston

Date Approved: 16 April 2014

ACKNOWLEDGEMENTS

I would like to express the deepest appreciation to all those who have helped me along the way in making this work and dissertation possible. First, I would like to thank my advisor, Dr. Russell D. Dupuis, for his guidance and for providing me with the valuable opportunity to participate in the field of MOCVD. I am very proud of being one of his students and I am honored to have worked for his Advanced Materials and Devices Group (AMDG) at Georgia Institute of Technology.

I would like to thank to my committee members, Dr. Douglas P. Yoder, Dr. Shyh-Chiang Shen, Dr. Oliver Brand, and Dr. Jae-Hyun Ryou, for the valuable comments and suggestions. It is a great honor to have your names on my thesis.

I am also thankful to my past and current members in AMDG: Dr. Jianping Liu, Dr. Hee Jin Kim, Dr. Suk Choi, Dr. Yong Huang, Dr. Zachery Lochner, Dr. Theeradetch Detchprohm, Nordine Sebki, Rumin Gong, Mi Hee Ji, Xiaohang Li, Kevin Liu, and Devin Justice. I was lucky to have the members of Dr. Shen's and Dr. Yoder's research group including Yi-Che (Steven) Lee, Tsung-Ting (Louis) Kao, and Cheng-Yin (Sam) Wang, and Mahbub Sattar. I would especially like to thank Dr. Jae-Hyun Ryou for many years of personal, professional, and technical guidance.

I am very grateful to all members in Hypen9 and Dokdo-United FC for being great friends in my life at Georgia Tech.

Finally, I would like to thank my family for their everlasting love and support. This accomplishment would not be possible without the patience and unconditional support of my loving wife, Se-Jeong, who has had hard time to bring up our lovely daughter and son, Ha-Eun and Ha-Eul almost by herself.

TABLE OF CONTENTS

	Page
ACKNOWLEDGEMENTS	iii
LIST OF TABLES	vii
LIST OF FIGURES	viii
SUMMARY	xii
 <u>CHAPTER</u>	
1 INTRODUCTION	1
1.1 III-nitride Materials Properties	2
1.2 Metalorganic Chemical Vapor Deposition Process and System	7
1.3 Efficiency Droop in Visible Light-emitting Diodes	11
1.4 Growth of the InAl(Ga)N Quaternary Alloys	17
1.5 Improvement of Light-extraction Efficiency by Surface Texturing	19
1.6 Scope of this Dissertation	21
2 MATERIAL AND DEVICE CHARACTERIZATION	23
2.1 Introduction	23
2.2 <i>In-situ</i> Temperature and Reflectance Measurement	23
2.3 Atomic Force Microscopy	31
2.4 Scanning Electron Microscopy	33
2.5 Secondary Ion Mass Spectrometry	34
2.6 Rutherford Backscattering Spectrometry	35
2.7 Photoluminescence	36
2.8 Electroluminescence	37
2.9 Transmission Line Measurement	38

2.10 X-ray Diffraction	41
3 IMPROVEMENT OF HOLE TRANSPORT AND DISTRIBUTION IN THE VISIBLE LIGHT-EMITTING DIODES	45
3.1 Introduction	45
3.2 Growth and Fabrication of the LED Structures	46
3.3 Characterization of the Dual-wavelength LEDs	52
3.4 Characterization of the Triple-wavelength LEDs	57
3.5 Effect of Si Doping in a Selected Quantum-well Barrier	63
3.6 Discussion on the Possible Mechanism of Improved Hole Transport ..	65
3.7 Summary	67
4 GALLIUM AUTO-INCORPORATION IN AN InAl(Ga)N LAYER	69
4.1 Introduction	69
4.2 Growth of the InAl(Ga)N Layer by MOCVD	71
4.3 Effects of the Underlying and Regrown Layers	74
4.4 Effects of the Growth Chamber Coating Conditions	79
4.5 Discussion on the Gallium Auto-incorporation	84
4.5.1 Comparison of Gallium Mole Fraction in the InAl(Ga)N Layers	84
4.5.2 Equilibrium Vapor Pressure of Gallium	86
4.5.3 Partial Pressure and Incorporation Efficiency of Group-III Precursors	88
4.5.4 Origins and a Mechanism of Gallium Auto-incorporation	90
4.6 Summary	91
5 IMPROVEMENT OF LIGHT EXTRACTION EFFICNECY OF THE VISIBLE LIGHT-EMITTING DIODES	93
5.1 Introduction	93
5.2 Growth and Fabrication of the Blue LEDs	95

5.3 Direct Surface Patterning by Three-beam Interference Laser Ablation .	97
5.4 Surface Characterization of the Laser-patterned LEDs	98
5.5 Electrical Characterization of the Laser-patterned LEDs	103
5.6 Device Electroluminescence Measurement Results	106
5.7 Theoretical Confirmation of the Enhanced Light-extraction Efficiency	110
5.8 Summary	112
6 RESEARCH SUMMARY	114
REFERENCES	119
VITA	129

LIST OF TABLES

	Page
Table 1.1: Lattice parameter values for hexagonal wurtzite structure of III-nitride semiconductors.	3
Table 1.2: Calculations of the bandgap energies of group III-nitride ternary alloys by Vegard's law.	4
Table 3.1: The sheet resistance and specific contact resistance of the <i>p</i> -type and <i>n</i> -type layers in the LEDs with <i>p</i> -GaN and <i>p</i> -In _{0.035} Ga _{0.965} N layers.	51
Table 4.1: Layer structures and growth parameters of the samples grown in this study.	73
Table 4.2: Mole fractions of GaN in InAl(Ga)N layers grown using same growth parameters, but using different chamber conditions, underlayers, and wafer susceptor/carrier conditions.	85
Table 4.3: The Antonie equation constants for the selected Group-III elements.	87
Table 4.4: Equilibrium vapor pressure of the Ga and the partial pressure of Group-III precursors in the reaction chamber at the growth temperature (T=890 °C) and the growth pressure (300 Torr) to grow InAl(Ga)N layer.	90

LIST OF FIGURES

	Page
Figure 1.1: Bandgap energy vs. lattice constant of III-nitride semiconductors at room temperature.	1
Figure 1.2: Unit cell of the hexagonal wurtzite structure of III-nitride semiconductors.	3
Figure 1.3: Direction of spontaneous polarization in III-nitride semiconductors with respect to the polarity (Ga- and N-polar) along the [0001] direction.	5
Figure 1.4: Basic diagram of the MOCVD reactor system.	9
Figure 1.5: Schematic illustration of MOCVD process in a vertical-flow system.	10
Figure 1.6: Schematic diagram of direct intra-band and direct inter-band Auger recombination processes.	13
Figure 1.7: Schematic illustration of indirect Auger recombination process.	14
Figure 1.8: Conduction-band energy of (a) a conventional LED structure and (b) a polarization-matched LED structure.	15
Figure 2.1: Thermal radiation of a black body according to Planck's Law.	25
Figure 2.2: True temperature measurement during the growth of the heteroepitaxial layer.	27
Figure 2.3: Reflections of the incident beam at the surface of transparent layer and the substrate.	29
Figure 2.4: Schematic illustration of the operation of an AFM system.	31
Figure 2.5: Schematic illustration of a SIMS measurement.	34
Figure 2.6: A typical linear TLM pattern showing the semiconductor mesa with metal contact pads separated by different distances.	39
Figure 2.7: Plot of the measured resistance as a function of the distance between the metal contact pads.	40
Figure 2.8: Schematic diagram of a typical configuration of a HR-XRD system.	43

Figure 3.1:	Schematic illustration of epitaxial layers of double-wavelength (DW) and triple-wavelength (TW) light-emitting diodes (LEDs) with different indium (In) mole fractions ($x_{\text{In}} = 0, 1.5, 2.5, \text{ and } 3.5\%$) in p -type layers.	47
Figure 3.2:	The bright-field, cross-section HR-TEM image of the triple-wavelength (TW) emitting MQW active region in a TW-LED structure on [11-20] zone axis.	48
Figure 3.3:	An optical microscope image of a wafer-level LED chip with the device size of $350 \times 350 \mu\text{m}^2$	49
Figure 3.4:	TLM I - V comparisons for p -layers and n -layers of the LEDs with different p -type layers.	50
Figure 3.5:	The comparison of photoluminescence (PL) spectra on each set of DW-LEDs having different MQW active region structures of (a) $n/\text{BBBBB}/p$ and (b) $n/\text{VVVVB}/p$ with p -GaN and $p\text{-In}_{0.035}\text{Ga}_{0.965}\text{N}$ layers.	53
Figure 3.6:	Ratio of integrated electroluminescence (EL) intensity of V-QWs to total integrated EL intensity at $I=80$ mA, depending on combinations of V-QWs and B-QWs in LEDs with p -GaN and $p\text{-In}_{0.035}\text{Ga}_{0.965}\text{N}$ layers.	54
Figure 3.7:	The ratio of total integrated EL intensities of DW-LEDs with $p\text{-In}_{0.035}\text{Ga}_{0.965}\text{N}$ layers to those with p -GaN layers according to the MQW active region design, at $I=80$ mA.	56
Figure 3.8:	(a) HR-XRD ω - 2θ scan results with (002) diffraction and (b) photoluminescence results for TW-LEDs with $p\text{-In}_{0.015}\text{Ga}_{0.985}\text{N}$, $p\text{-In}_{0.025}\text{Ga}_{0.975}\text{N}$, and $p\text{-In}_{0.035}\text{Ga}_{0.965}\text{N}$ layers for LED A, LED B, and LED C, respectively.	58
Figure 3.9:	EL spectra of (a) LED A, (b) LED B, and (c) LED C with $p\text{-In}_{0.015}\text{Ga}_{0.985}\text{N}$, $p\text{-In}_{0.025}\text{Ga}_{0.975}\text{N}$, $p\text{-In}_{0.035}\text{Ga}_{0.965}\text{N}$ layers, respectively, at different injection currents.	60
Figure 3.10:	Normalized EL emission intensity of each QW in the LED A, B, and C with $p\text{-In}_{0.015}\text{Ga}_{0.985}\text{N}$, $p\text{-In}_{0.025}\text{Ga}_{0.975}\text{N}$, and $p\text{-In}_{0.035}\text{Ga}_{0.965}\text{N}$ layers, respectively, at an injection current of 80 mA.	62
Figure 3.11:	EL spectra of LEDs at $I=80$ mA, employing a $p\text{-In}_{0.025}\text{Ga}_{0.975}\text{N}$ layer with Si doping in a selected QW barrier (QWB) of TW-LEDs consisting of $n/\text{V}(\text{QW1})\text{B}(\text{QW2})\text{C}(\text{QW3})/p$. The location of Si doping in a selected QWB is shown in the inset.	64

Figure 3.12:	Ratio of EL integrated intensity from each QW of TW-LEDs A and C consisting of $n/V(QW1)B(QW2)Cy(QW3)/p$ and ratio of total EL intensity of the LED C to that of the LED A with increasing current.	66
Figure 4.1:	Bandgap energy vs. lattice constant and strain status of III-nitride compound semiconductors.	69
Figure 4.2:	High-resolution X-ray diffraction (HR-XRD) ω - 2θ scans near the (00•2) diffraction condition of templates for (a) an InAl(Ga)N layer grown on an AlN template (sample A) and (b) InAl(Ga)N layers grown on GaN templates without and with a GaN regrown layer (samples B and C, respectively).	75
Figure 4.3:	Schematic view showing possible sites leading to Ga auto-incorporation in a growth chamber with close-coupled showerhead. The possible sites consist of (1) a Ga-containing III-N epitaxial underlayer, (2) a wafer susceptor/carrier, (3.1) quartz liner, and (3.2) stainless-steel showerhead and chamber walls.	77
Figure 4.4:	HR-XRD ω - 2θ scans near the (00•2) diffraction condition of wurtzite GaN of InAl(Ga)N layers grown under various Cp_2Mg molar flow rates; corresponding to sample C, D, E, and F.	79
Figure 4.5:	Asymmetric RSM using (10•5) diffraction condition of wurtzite GaN for the InAl(Ga)N layers of (a) sample C, (b) sample D, (c) sample E, and (d) sample F grown under various Cp_2Mg molar flow rates.	80
Figure 4.6:	The variation in mole fraction of each Group-III element obtained by RBS in InAl(Ga)N layers with different D/III ratios; corresponding to sample C, D, E and F.	81
Figure 4.7:	SIMS distribution profiles of Group-III elements and Mg for (a) an InAl(Ga)N:Mg layer grown on a GaN:ud layer (sample E') and (b) an InAl(Ga)N:ud layer grown on a GaN:Mg layer (sample G).	83
Figure 5.1:	Schematic illustration of epitaxial layer structure of a blue LED. ...	96
Figure 5.2:	Schematic illustration of the configuration for the three-beam interference laser ablation.	98
Figure 5.3:	Surface image of the laser-patterned LED; showing periodic array of 2-dimensional pattern measured by SEM.	99
Figure 5.4:	(a) Surface image and (b) depth profile of the laser-patterned LED; showing inverted-cone-shaped holes at the top p -GaN layer measured by AFM.	100

Figure 5.5:	The current-voltage (I - V) measurement results of the laser-patterned LED and the conventional (non-patterned) LED.	103
Figure 5.6:	The TLM plots for the laser-patterned LED and the conventional (non-patterned) LED.	105
Figure 5.7:	Plots of the integrated EL intensity according to injection current for the laser-patterned LED and the conventional LED.	107
Figure 5.8:	Comparison of the EL spectra at an injection current of $I=80$ mA for the laser-patterned LED and the conventional LED.	108
Figure 5.9:	PL spectra for (a) the laser-patterned LED and (b) the conventional LED.	109
Figure 5.10:	Cross-sectional ray-tracing views of (a) the conventional LED and (b) the laser-patterned LED, and (c) the Far-field patterns of LEDs with and without surface texture calculated by Monte-Carlo ray-tracing simulation.	111

SUMMARY

III-Nitride based visible light-emitting diodes (LEDs) present a huge opportunity for next generation solid-state lighting because of the advantages of high power output, low power consumption, long lifetime, and eco-friendly characteristics. However, the decrease in the quantum efficiency of III-nitride based LEDs with increasing drive currents after rapidly arriving at the peak efficiency at low current density, commonly referred to as “efficiency droop” poses a major technical challenge for LED lamps used in high power lighting. The origin of the efficiency droop is still controversial while several possible mechanisms have been suggested; including electron spill-over, high defect density, and Auger recombination. However, most of the discussions on the efficiency droop in III-nitride LEDs point out the importance of the carrier injection into the active region, the distribution of carriers across the active region, and the densities of carriers in the QWs. To understand the carrier injection and transport in the MQW active region, the engineering of carrier dynamics by modifying the *p*-type layers that do not belong to the active region is described in this dissertation. Especially, the effect on the hole transport in the active region and resulting hole distribution among the MQWs by controlling the indium (In) mole fraction in *p*-type $\text{In}_x\text{Ga}_{1-x}\text{N}:\text{Mg}$ layers of the LED structures was focused on. A dual-wavelength (DW)- and a triple-wavelength (TW)-emitting MQW design containing different-color $\text{In}_x\text{Ga}_{1-x}\text{N}$ QWs, allowing that each QW emits its own characteristic wavelength, was employed to effectively trace the emitted photons from the active region. It was found that the holes are preferentially injected into the QW adjacent to the *p*-type layer with lower In-mole-fraction $p\text{-In}_x\text{Ga}_{1-x}\text{N}:\text{Mg}$ layer. Enhanced hole transport with increasing In mole fraction in the $p\text{-In}_x\text{Ga}_{1-x}\text{N}:\text{Mg}$ layer has

been shown by analyzing the EL spectra. The improved hole transport and corresponding uniform distribution was achieved presumably by potential barrier near *p*-type layer and MQW active region. This is because the holes injected into the MQW active region achieve kinetic energy depending on the potential barrier between the last GaN QW barrier and the *p*-type $\text{In}_x\text{Ga}_{1-x}\text{N}:\text{Mg}$ layer, resulting in a hole transport favorable environment in the MQW active region. At the same time, the limited hole injection due to the potential barrier for hole can be overcome under high injection conditions.

The InAlN layers are widely used as an alternative high quality electron blocking layer in InGaN/GaN based visible LED structures. However, the Ga auto-incorporation of the InAlN layers has been recently reported during the growth of epitaxial layers by both MOCVD and MBE. To identify the possible origins and a mechanism of Ga auto-incorporation of InAlN epitaxial layers, the quaternary InAl(Ga)N epitaxial layers that were intended to be ternary InAlN layers were systematically investigated in this dissertation. It was found that the Ga-containing deposition on a wafer susceptor/carrier is the most dominant precursor for Ga auto-incorporation and the deposition on surrounding surfaces of quartz parts in a growth chamber is the other dominant source, while the effect of stainless-steel parts and interdiffusion of Ga atom from GaN underlayer are not critical. In addition, Mg or Cp_2Mg in the growth chamber during InAl(Ga)N layer growth facilitates the auto-incorporation of Ga by modifying deposition conditions of GaN on surrounding surfaces and a wafer susceptor/carrier. Based on experimental data of various cases, a mechanism for Ga auto-incorporation in InAl(Ga)N has been proposed. The mechanism includes (i) In-Ga eutectic formation on Ga-containing deposition with abundant In and (ii) desorption of Ga (and In) from a liquid

phase from surrounding surfaces into gas-phase Ga, followed by (iii) adsorption of Ga on a growing InAlN epitaxial layer. Therefore, Ga-containing deposition on any hot surfaces that are also exposed to In precursor to form a liquid phase is believed to be major origins of Ga auto-incorporation.

In an effort to enhance the light extraction efficiency (LEE) in the LEDs, the direct patterning on the top surface of a LED structure, using laser interference ablation technique, has been studied in this study. The 2-dimensional hexagonal lattice array of surface patterns was simply generated by direct irradiation of the laser source which is the interference of three laser beams onto the top *p*-GaN surface, without deterioration of electrical property of *p*-type layer and optical properties of MQW active region. The experimental results showed approximately 20 % improved LEE of the laser-patterned LED structure compared to the conventional LED structure without surface textures. Furthermore, the theoretical calculation using Monte-Carlo ray-tracing simulation confirmed the enhancement of LEE of the laser-patterned LED structure. The laser interference ablation technique using three or more laser beams can offer the possibility to realize homogenous microstructures having complex patterns on the large surface area.

CHAPTER 1

INTRODUCTION

Group III-nitride semiconductors such as GaN, InN, AlN, and their ternaries along with quaternary alloys have drawn enormous attention as one of the most important semiconductors after Silicon that is the most commonly known semiconductor because of their direct- and wide-bandgap nature. The bandgap energies of III-nitride semiconductors can be tunable from 0.7 eV to 6.2 eV by the combination of the binary alloys. This range of bandgap energy covers a wide range of the electromagnetic spectrum ranging from the deep ultraviolet (AlN, $E_g = 6.2$ eV) through the visible and the ultraviolet (GaN, $E_g = 3.4$ eV) to the infrared range (InN, $E_g = 0.7$ eV), as shown in Figure 1.1.

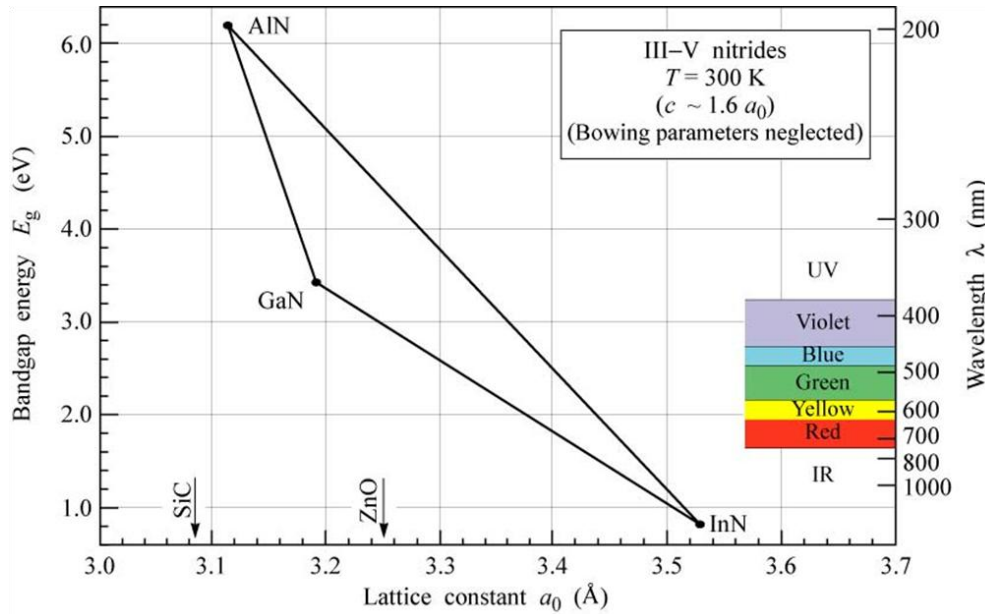


Figure 1.1: Bandgap energy vs. lattice constant of III-nitride semiconductors at room temperature.

This property allows the III-nitride semiconductors to be used as a basic material for the photonic devices such as laser diodes and light-emitting diodes. In addition, the intrinsic high carrier mobility, high breakdown field, and capability of forming heterostructures of III-nitride semiconductors enable high-speed and high-power electronic devices such as heterojunction bipolar transistor and high-electron-mobility transistor. Moreover, the superior thermal and chemical stability of III-nitride semiconductors even at elevated temperatures make them excellent candidate for a device operation at high temperature and harsh environment. From these beneficial properties, the electronic and photonic devices based on III-nitride semiconductors have attracted much attention in a variety of applications such as high-density optical storage, solid-state lighting, water purification, medical equipment, and for the space and military industries.

1.1 III-nitride Materials Properties

The crystallographic structure of the group III-nitride semiconductor materials can be of either a hexagonal wurtzite, cubic zinc-blende, or rock-salt structure. Under ambient conditions, the hexagonal wurtzite structure is thermodynamically the most stable crystalline structure for the III-nitride semiconductors compared to the cubic zinc-blende and rock-salt structure [1]. The hexagonal wurtzite structure of III-nitride materials is composed of two interpenetrating hexagonal close-packed (HCP) sub-lattices, and each HCP sub-lattice contains six atoms of each type. The crystal lattice of the hexagonal wurtzite structure can be described by two lattice constants, a in the basal plan and c in the perpendicular direction to the basal plane, and a microscopic dimensionless parameter u , as schematically illustrated in Figure 1.2.

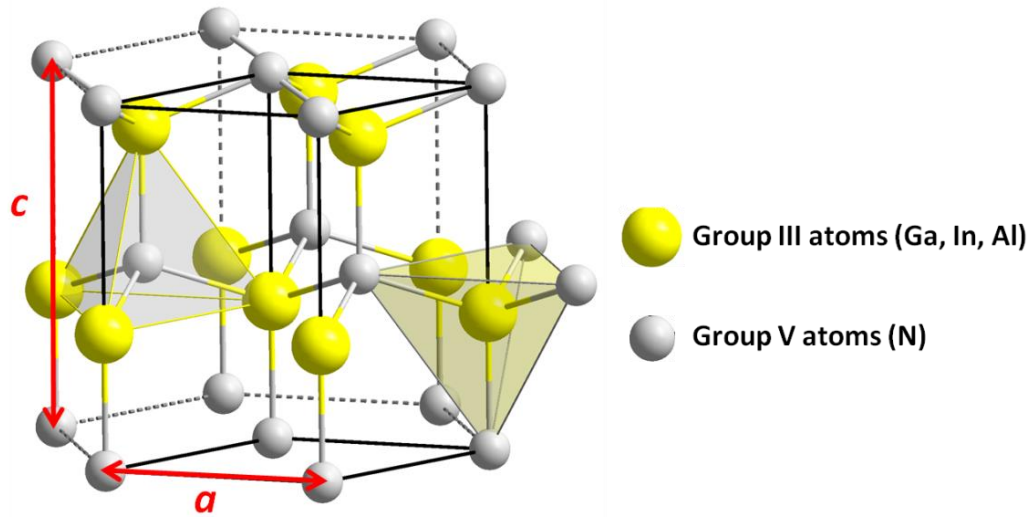


Figure 1.2: Unit cell of the hexagonal wurtzite structure of III-nitride semiconductors.

The internal parameter u is the interatomic distance in the basic unit cell of a hexagonal wurtzite structure, which is defined as the bond length between cation and anion divided by c lattice parameter. The lattice parameter values for wurtzite III-nitride semiconductors are shown in Table 1.1. In the ideal wurtzite structure, the internal parameter u is always equal to $3/8=0.375$, and the ratio of c/a is always 1.633. However, III-nitride semiconductors are not ideal wurtzite structures due to the strong ionic bonding resulting from the large differences in the electronegativity of the Group III metal atoms and nitrogen atoms. Thus, the parameter u is always higher than 0.375 and the c/a is always lower than 1.633, as shown in Table 1.1.

Table 1.1: Lattice parameter values for hexagonal wurtzite III-nitride semiconductors [2, 3].

Binary alloy	a (Å)	c (Å)	c/a ratio	u
InN	3.5170	5.6850	1.616	0.379
GaN	3.1894	5.1861	1.626	0.3789
AlN	3.1120	4.9808	1.600	0.3869

The distortion of the unit cell from the ideal wurtzite structure generates polarization charge along the c -axis. This is called spontaneous polarization and the value changes from 0.034 C/m^2 for GaN through 0.042 C/m^2 for InN to 0.090 C/m^2 for AlN along the opposite to the $[0001]$ direction. In addition, due to the lack of inversion symmetry in the unit cell of a wurtzite group III-nitride semiconductor, the polarity of a structure needs to be dealt with. The directions of spontaneous polarization in III-nitride semiconductors having different polarity, Ga-polar and N-polar, are schematically shown in Figure 1.3 relative to the $[0001]$ direction.

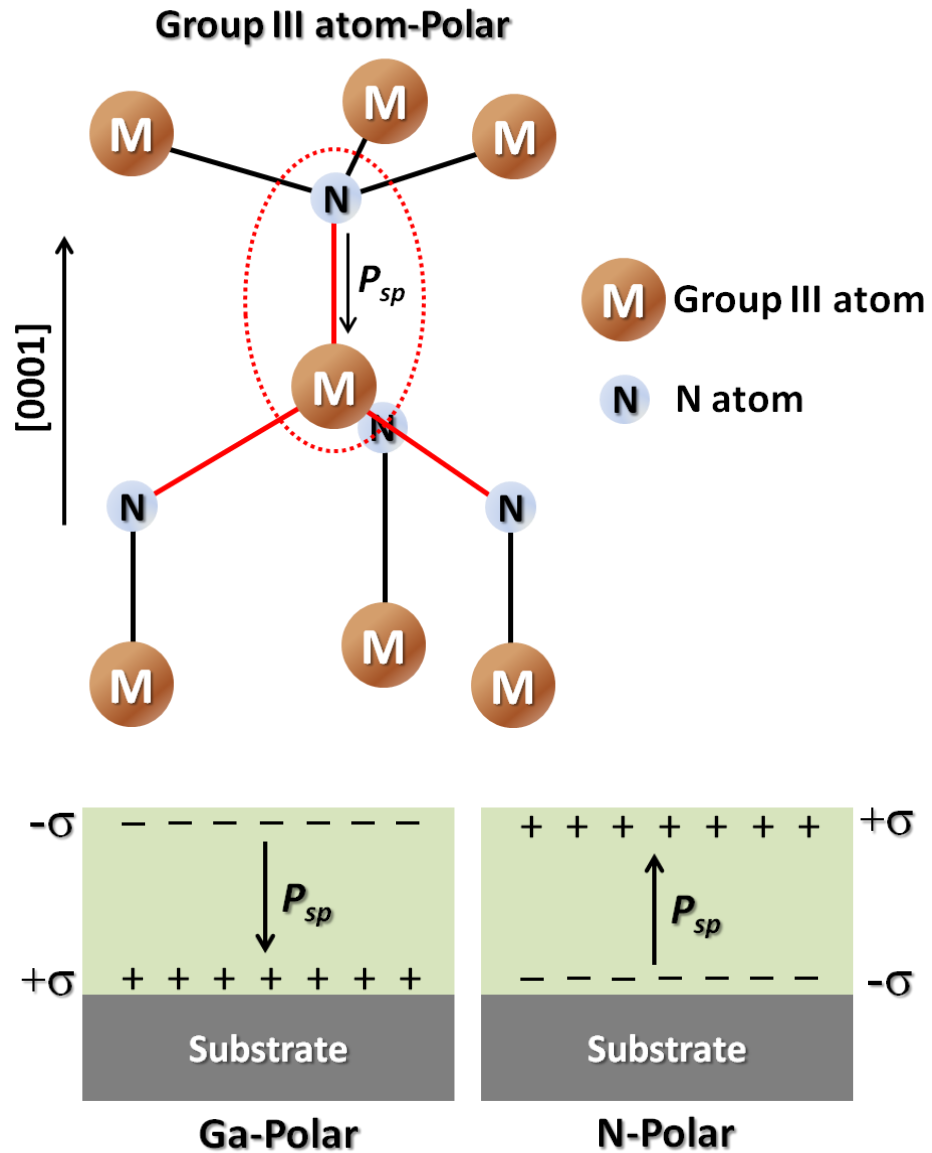


Figure 1.3: Direction of spontaneous polarization in III-nitride semiconductors with respect to the polarity (Ga-polar and N-polar) along the [0001] direction.

The strong ionic bonding in the group III-nitride semiconductors is resulted from the large differences in the electronegativity between the group III metal cations and nitrogen anions [4]. The large differences in the ionic radii and bonding energies of the group III atoms (cations) lead to different lattice constants, bandgap energies, and

electron affinities of the III-nitride semiconductors. Furthermore, the superior thermal- and chemical stability of the wurtzite III-nitride semiconductors are also contributed by their strong bond strength. These characteristics of III-nitride semiconductors play an important role to be a promising candidate for photonic- and electronic-devices used for the device operation under high power and high-temperature environment.

The wurtzite III-nitride alloys are direct bandgap semiconductor having wide bandgap energy. The bandgaps of III-nitride binary alloys are known as 0.7 ± 0.05 eV [2, 5], 3.52 ± 0.1 eV [4], and 6.1 ± 0.1 eV [4] for InN, GaN, and AlN, respectively. In addition, the bandgap energy can be further engineered by controlling the mole fraction of each binary component in the ternary or quaternary alloys. The ternary combinations, such as $\text{In}_x\text{Ga}_{1-x}\text{N}$, $\text{Al}_x\text{Ga}_{1-x}\text{N}$, and $\text{In}_x\text{Al}_{1-x}\text{N}$, can be determined by Vegard's Law with the mole fraction of the binary alloys and their fundamental bandgap energies, as shown in equation (1.1):

$$E_g(\text{A}_x\text{C}_{1-x}\text{N}) = x \cdot E_g(\text{A}) + (1-x) \cdot E_g(\text{C}) - b \cdot x \cdot (1-x), \quad (1.1)$$

where $E_g(\text{A}_x\text{C}_{1-x}\text{N})$ is the bandgap energy of a ternary alloy, $E_g(\text{A})$ and $E_g(\text{C})$ are the bandgap energies of binary alloy A and C, respectively, x is the alloy mole fraction in a $\text{A}_x\text{C}_{1-x}\text{N}$ alloy, and b is the bandgap bowing parameter that is specific to each compound and determined experimentally. The bandgap energies of each binary alloy and the bowing parameters for group III-nitride ternary alloys are shown in the Table 1.2.

Table 1.2: Calculations of the bandgap energy of the group III-nitride ternary alloys by using Vegard's Law [2, 4-7]

$A_xC_{1-x}N$	E_g of A (eV)	E_g of C (eV)	b^*
$In_xGa_{1-x}N$	0.7 ± 0.05	3.52 ± 0.1	1.6 ± 0.2
$Al_xGa_{1-x}N$	6.1 ± 0.1	3.52 ± 0.1	0.7 ± 0.1
$In_xAl_{1-x}N$	0.7 ± 0.05	6.10 ± 0.1	$3.4x \pm 1.2$

Therefore, the range of bandgap energy of III-nitride semiconductors can cover a wide span of electromagnetic spectrum ranging from the deep ultraviolet through the visible and the ultraviolet to the infrared by the combination of each binary or ternary component, as shown in the Figure 1.1.

1.2 Metalorganic Chemical Vapor Deposition Process and System

Metalorganic chemical vapor deposition (MOCVD) is a well-established growth method for the growth of III-nitride semiconductors [8]. The MOCVD process was initially developed by Manasevit et al. [9] in late 1960's, and the first practical devices such as AlGaAs/GaAs-solar cells and quantum-well injection laser were grown using MOCVD by Dupuis et al. in 1977 and 1978 [10,11]. Due to the major breakthroughs provided in the late 1980's, the growth of III-nitride semiconductor using MOCVD was rapidly improved. Amano et al. provided two step growth in 1986 [12] and achieved p-doping in GaN successfully in 1989 [13]. In addition, Nakamura et al. developed the

InGaN layer grown on GaN layer with high crystal quality for the blue and green optoelectronic devices via two-flow reactor design [14]. Recently, the MOCVD growth technique is widely accepted to grow epitaxial layer of the III-nitride compound semiconductors for photonic- and electronic-devices because of the advantages including high-quality grown layers, high throughput and flexibility, and suitable for the growth of hetero-structures.

The MOCVD system used for this study is a Thomas Swan 6 x 2” rotating disk reactor with a close coupled showerhead (CCSTM). The reaction chamber is made of a material that stands up to high temperatures and does not react with the chemicals being used. The reaction chamber is composed of reactor wall, close coupled showerhead, quartz liner, heating element, gas injection system, and a wafer carrier/susceptor. Since the MOCVD used in this study is a type of hot-wall CVD, the temperature of the entire reaction chamber can be increased up to ~1100 °C. Thus, the reactor wall is equipped with an active water cooling system to prevent overheating. The molar flow rates of metalorganic and hydride sources are controlled by gas inlet and switching system which is composed of mass flow controller, pressure controller, and manual or automatic switching valves. In addition, the toxic waste matter generated by the chemical reaction in the chamber can be safely disposed by the gas exhaust and cleaning system. A basic diagram of this MOCVD system is schematically described in Figure 1.4.

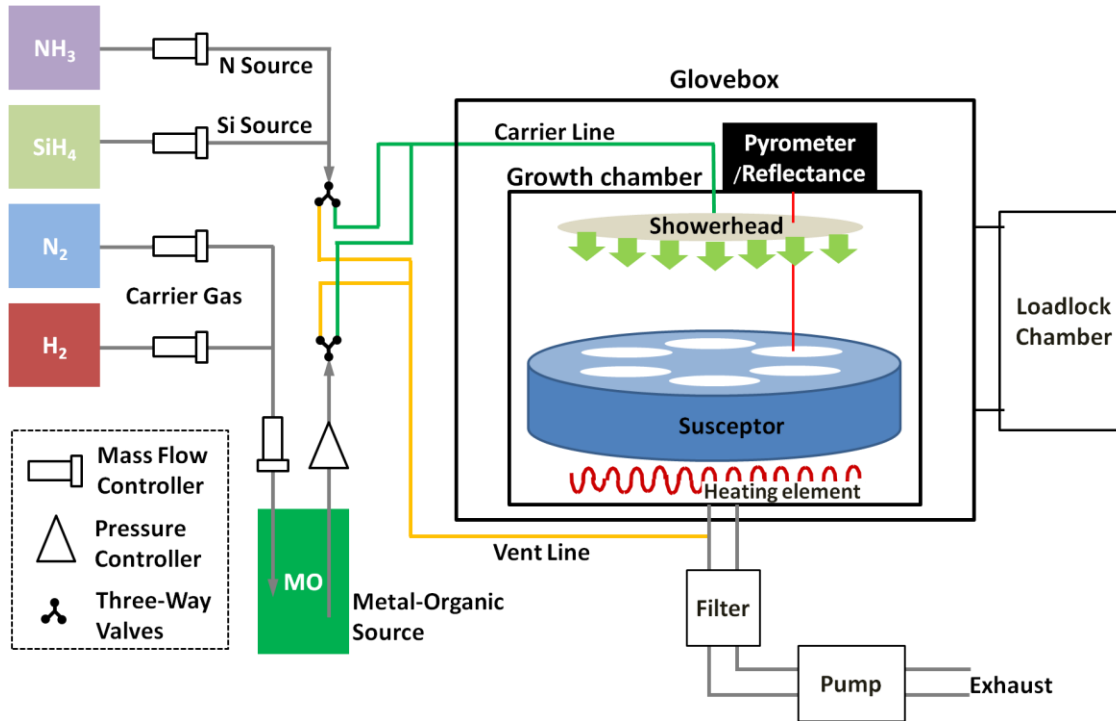


Figure 1.4: Basic diagram of the MOCVD reactor system.

In MOCVD, ultra pure precursors are transported to the reaction chamber by carrier gas, N_2 or H_2 , and then the reactant gases generated by pyrolysis are chemically react with each other to form an epitaxial layer of the desired group-III-nitride compound on a substrate surface. The pyrolysis is thermo-chemical decomposition of an organic material at elevated temperature in the absence of oxygen in the growth chamber. The trialkyls, trimethylgallium (TMGa) and triethylgallium (TEGa), trimethylaluminum (TMAI), and trimethylindium (TMIIn) are commonly used as the group III precursors. Ammonia (NH_3) is typically used as the precursor for the nitrogen. The chemical reaction between metalorganic precursor and NH_3 to form an III-nitride-based epitaxial layer can be expressed by following chemical reaction formula (1.2):



where A is the alkyl group of methyl (CH_3) or ethyl (C_2H_5), M is the group III metal such as gallium (Ga), aluminum (Al), or indium (In), and H is hydrogen. The MOCVD process in a vertical-flow system is schematically illustrated in Figure 1.5.

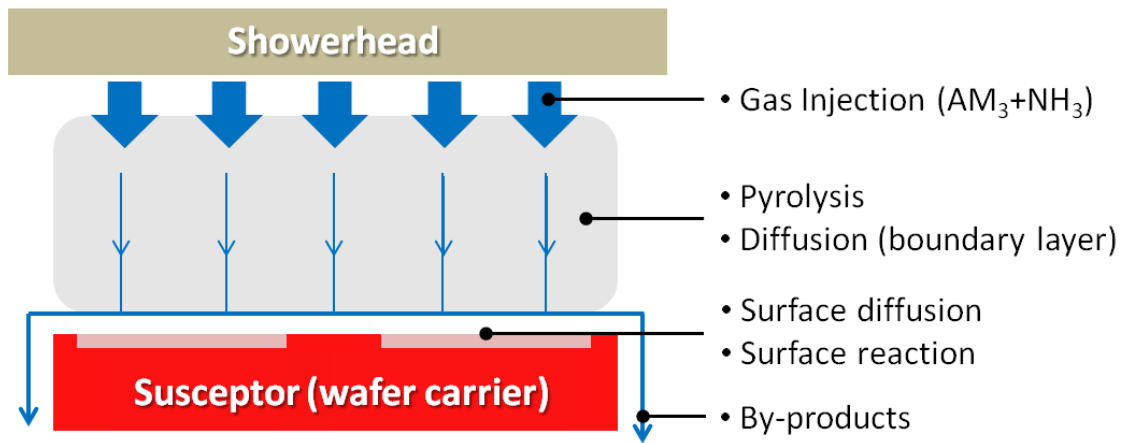


Figure 1.5: Schematic drawing of MOCVD process in a vertical-flow system.

The metalorganic precursors, composed of trialkyls and group III metal atoms, and hydrides are decomposed into each chemical element by pyrolysis at near the surface where reactants are combined together. The pyrolysis leaves the group III metal and nitrogen atoms on the surface of a substrate and those atoms bond together to form a new crystalline epitaxial layer. Since the MOCVD process is typically used in the mass transport limited regime, the concentration of the source material in the reaction and the growth rate depend on the amount of metalorganic source injected into the reaction chamber [15]. The molar flow rate of the metalorganic source transported into the

reaction chamber depends on the equilibrium vapor pressure of the precursor, the pressure of the metalorganic source container, and the flow rates of carrier gases.

1.3 Efficiency Droop in Visible Light-emitting Diodes

Group III-nitride (III-N)-based visible light-emitting diodes (LEDs) are currently widely employed in display- and general-lighting applications because of their low power consumption, long lifetime, and eco-friendly characteristics. The significant improvements in the internal and external quantum efficiencies have played an important role in achieving high brightness LEDs, replacing conventional lighting sources such as incandescent and fluorescent lamps. Recently, the best blue LEDs exhibit the internal quantum efficiency (IQE) over 80 % at the current density of $\sim 35 \text{ A/cm}^2$. While the peak luminous efficiencies of LED-based lamps at relatively low currents far exceed those of incandescent and fluorescent lamps, the efficiency of LED lamps at high currents diminishes with increasing drive currents, commonly referred to as an efficiency droop. The efficiency droop is a common feature of all III-N-based LEDs and poses a major technical challenge for LED lamps used in high-power lighting. The most advanced devices developed currently still exhibit significant efficiency droop at high current densities around 100 A/cm^2 . Even though it has been widely accepted that the efficiency droop is not a thermal issue (*i.e.*, Joule heating) [16], but a fundamental problem associated with III-nitride materials and their heterostructures, the origin of the efficiency droop is still controversial, and several possible mechanisms to correct this problem have been suggested.

It has been reported that the efficiency droop might be related to the interaction between threading dislocations and carrier delocalization [17, 18]. In the InGaN-based multiple quantum wells (MQWs), the injected carriers fill the localized states caused by indium composition fluctuation before being trapped into nonradiative recombination centers such as crystal defects. At relatively high injection current densities, however, the delocalized carriers from the localized states are transferred to threading dislocations, where they can recombine nonradiatively, resulting in efficiency droop. Thereafter, Schubert et al. argued that the dislocations do not strongly impact high current performance; instead these dislocations contribute to the increased nonradiative recombination at lower currents and suppression of peak efficiency [19].

Shen et al. claimed that Auger recombination as the origin of efficiency droop, while delocalization and overflow of carriers are not playing a role in the drop in efficiency at high current densities [20]. In addition, less efficiency droop was demonstrated by using double-heterostructure active regions. This approach allows lower carrier density in the active region and thus, minimizes the effect of Auger recombination [21]. The Auger recombination process usually involves two carriers recombining and transferring the energy to a third carrier instead of emitting the energy as a photon, as shown in Figure 1.6. Since this process requires three carriers, the Auger recombination tends to take place at high carrier densities. The difference between intra-band process and inter-band process in the direct Auger recombination depends on whether the final state of the scattered carrier locates in the same band (direct intra-band) or different band (direct inter-band) as the initial state [22], as compared in Figure 1.6.

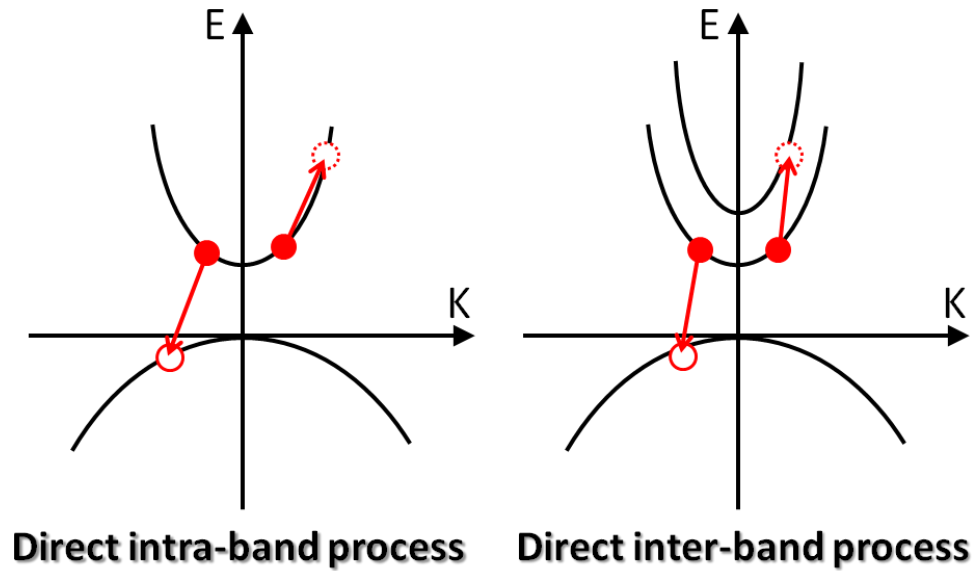


Figure 1.6: Schematic diagram of direct intra-band and direct inter-band Auger recombination.

However, many reports have suggested that the direct Auger recombination process may not be the reason for the efficiency droop [23-25]. This is because the direct intra-band Auger effect has been shown to be extremely small according to theoretical many-particle calculation, and the direct inter-band Auger recombination process can explain the efficiency droop only in certain indium composition. The indirect Auger recombination process, assisted by electron-phonon coupling and alloy scattering, has been suggested to explain the efficiency droop instead of direct Auger recombination process [25]. In the case of the indirect Auger recombination, the process is mediated by the scattering process such as the electron-phonon coupling, alloy disorder, or Coulomb scattering by charged defects [25], as schematically described in Figure 1.7.

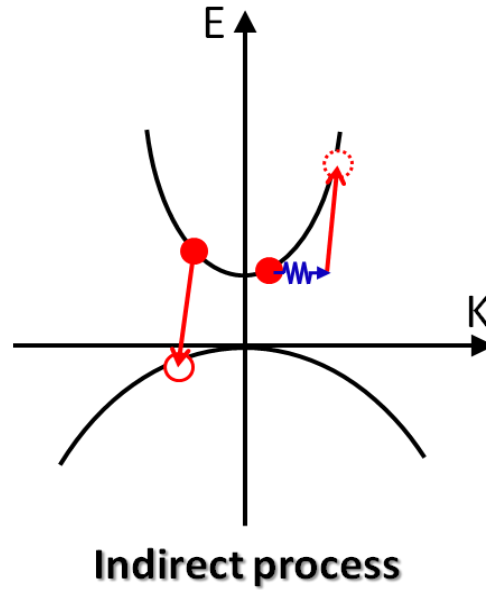


Figure 1.7: Schematic illustration of indirect Auger recombination process [25].

Recently, the phonon-assisted indirect Auger recombination process is getting more attention as a fundamental origin of the efficiency droop, while the direct Auger recombination process has now been generally discounted.

As a result of inefficient electron confinement in the active region, carrier spill-over has been suggested as a suspect of the origins of the efficiency droop. The carrier spill-over in a LED structure is schematically described in Figure 1.8(a) and (b) according to the different polarization field in the MQW active region.

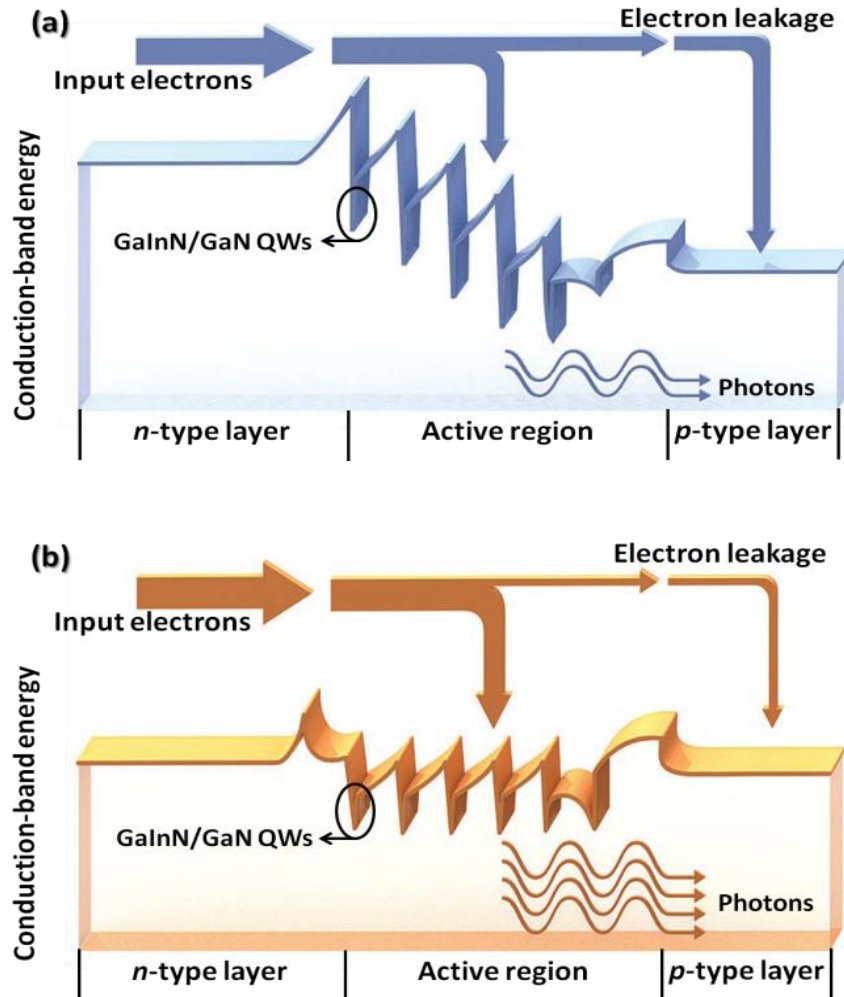


Figure 1.8: Conduction-band energy of (a) a conventional LED structure and (b) a polarization-matched LED structure. (Illustration: Bryan Christie, IEEE spectrum 2009)

Rozhansky et al. proposed that the drop of external quantum efficiency at high current density typically observed for AlInGaN LEDs is caused by reduction of injection efficiency due to electron leakage at high pumping [26]. Also, it has been reported that the polarization in the active region and electron-blocking layer (EBL) results in electron spill-over and corresponding efficiency droop [27, 28]. Thus, the polarization-matched MQWs and EBL, using AlInGaN quaternary alloys, have been suggested as a method to

reduce electron leakage from the active region. The different conduction-band energies for the conventional LED structure and the polarization-matched LED structure are compared in Figure 1.8(a) and (b), respectively. In the polarization-matched LEDs, the photons generated by the radiative recombination can be enhanced due to the lack of spatial separation of electron and hole wave functions in the MQWs. In addition, more carriers injected into the active region are able to be captured uniformly across the MQWs active region, resulting in reduction of carrier spill-over.

Achieving uniform carrier distribution in multiple quantum-wells (MQWs) active region has recently been proposed as a way to mitigate the efficiency droop [29, 30], since the distribution and the number of holes in each QW modify electronic band structure under carrier injection and Auger recombination rate [29, 31]. In order to accomplish uniform hole distribution, efficient hole injection followed by effective hole transport in the MQWs is considered to be of critical importance. Limited hole transport across the MQWs and non-uniform hole distribution in the active region result not only from the relatively large effective mass of holes but also from the specific characteristics of the QWs, QW barriers (QWBs), and electron-blocking layers (EBLs) [29-35].

Except the possible origins of efficiency droop explained above, hot carrier effect by high plasma carrier temperature [36], exciton dissociation [37], and parasitic tunnelling of carriers [38] have been proposed, but these explanations are not widely acknowledged.

Even though several possible mechanisms have been suggested, the origin of the efficiency droop is still not clearly understood. However, most of the discussions on the efficiency droop in III-nitride LEDs point out the importance of the carrier injection into

the active region, the distribution of carriers across the active region, and densities of carriers in the QWs. For example, the effect of the EBL and leakage current is related to the carrier injection, Auger recombination becomes dominant at high carrier density in the QWs, and carrier delocalization from the localized states is related to the carrier density in the QWs. Therefore, achieving high carrier injection followed by uniform distribution of the carriers may be a key issue to identify and resolve the efficiency droop.

1.4 Growth of InAl(Ga)N quaternary alloy

InAlN ternary alloys have drawn attention for device applications involving III-nitride (III-N)-based materials due to their large refractive index contrast and wide bandgap energy with respect to GaN; as well as the possibility to grow epitaxial layers that are lattice-matched and strain-/polarization-engineered on binary GaN and AlN, and on ternary AlGaN and InGaN layers [39-41]. These advantages enable the InAlN alloys to be used in various epitaxial structures for photonic devices, such as GaN/InAlN superlattices for near-infrared intersubband transitions [42], high-reflectivity short-wavelength distributed Bragg reflectors in vertical-cavity surface-emitting lasers [43], cladding and waveguide layer structures in edge-emitting lasers [44,45], and electron-blocking layers in visible light-emitting diodes [46-48]. For electronic device applications, an $\text{In}_{0.18}\text{Al}_{0.82}\text{N}/\text{GaN}$ heterostructure, exhibiting a high sheet carrier density in the channel region of two-dimensional electron gas, makes the structure suitable for high-electron mobility transistors [49]. Also, polarization-engineered $\text{In}_x\text{Al}_{1-x}\text{N}$ layers have been used as a Schottky barrier to demonstrate enhancement-mode (normally-off) heterostructure field-effect transistors [50].

Many potential advantages of the InAlN alloys and their heterostructures for such applications justify further improvement in material quality and controllability in their epitaxial growth processes to overcome current technical challenges in the InAlN materials. The InAlN materials may experience phase separation, compositional variations, deviations from Vegard's law in lattice constants, and anomalous ion channeling [51-55]. Furthermore, huge differences in optimized growth conditions for InN and AlN layers pose additional technical challenges to achieve high-quality and accurately-controlled InAlN epitaxial layers using metalorganic chemical vapor deposition (MOCVD) and molecular beam epitaxy (MBE) [56-59]. AlN layers are typically grown at higher growth temperature and lower growth pressure with low V/III ratios to reduce parasitic reactions in the gas phase and to enhance the surface migration of the Al ad-atom species [60,61], which are completely opposite from the typical growth conditions for InN layers. Thus, meticulous optimization of the growth conditions for InAlN materials is required to grow high-quality epitaxial layers with accurate process control of growth parameters and conditions. However, while growth and characterization of $\text{In}_x\text{Al}_{1-x}\text{N}$ thin-film with various growth parameters have been studied to achieve high-quality epitaxial materials [56-59], the fundamental understanding on the $\text{In}_x\text{Al}_{1-x}\text{N}$ materials and epitaxial growth processes is still lacking. In the majority of previous studies, the focus has been on the growth and characterizations of epitaxial $\text{In}_x\text{Al}_{1-x}\text{N}$ layers, with the assumption that these materials are ternary InAlN, which did not seem to be unreasonable, since only indium (In), aluminum (Al), and nitrogen (N) precursors were introduced for the growth of the layer. Recently, possible unintentional incorporation of Ga (auto-doping or auto-incorporation, depending on the amount of

gallium (Ga) present in InAlN layers) has been reported during the epitaxial growth of the InAlN layers by both MOCVD and MBE [62, 63]. However, the origins of Ga incorporation in InAlN layers, resulting in InAl(Ga)N quaternary layers, and the auto-incorporation mechanism have not been clearly identified. This uncertainty could make the characterization of materials and devices containing InAl(Ga)N layers prone to erroneous analysis and conclusion by ignoring possible uncontrolled Ga content in the layer. Therefore, the fundamental understanding of materials and epitaxial growth process of InAlN and InAlGaN needs to be addressed and studied.

1.5 Improvement of Light-extraction Efficiency by Surface Texturing

III-nitride (III-N)-based light-emitting diodes (LEDs) are extensively used for various display and signal applications such as traffic lights, indoor and outdoor decoration, automobile lighting, liquid-crystal display back-lighting, and many others. Recently, the movements for replacing general lighting sources such as incandescence and fluorescent lamps are actively progressed with the significant improvements in quantum efficiency, optical output power, and color rendering of III-N-based white LEDs [64]. For the improvement of external quantum efficiency, light-extraction efficiency (LEE) of the LEDs has to be further improved along with the enhancement of internal quantum efficiency [65, 66]. The large difference in the refractive indices of semiconductor ($n_{\text{GaN}}=2.5$ at $\lambda\sim 430$ nm) and air ($n=1$) results in low critical angle for light extraction from the surface [65-68]. Most photons generated in the multiple-quantum well (MQW) active region are reabsorbed into the semiconductor materials by total internal reflection [69, 70].

In an effort to enhance the LEE of the GaN-based LEDs, several methods have been proposed and demonstrated including surface roughening [65, 67, 71], laser lift-off process [72], texturing indium tin oxide (ITO) transparent contact [73], growth on patterned sapphire substrates [74], and photonic crystals [75]. While these approaches were reported that they successfully improved the LEE, the surface roughening surpasses other methods in terms of process simplicity, low cost, large area production, and excellent controllability [76]. In general, the texturing of the GaN surface is typically achieved by plasma dry etching or KOH-based wet-chemical etching. However, the surface texturing created by the dry etching techniques is accompanied with radiation damages on the *p*-type surface by plasma ions, resulting in significant degradation of electrical properties of the diodes with non-Ohmic behavior of *p*-type electrode [77]. In the case of the wet-chemical etching, it is very difficult to form periodically arranged or designed surface features due to crystal-plane-dependent etching rates [78]. Furthermore, both etching methods require complex fabrication steps, such as additional photolithography process in the dry etching and deposition and removal of a protection layer in the wet-chemical etching, increasing manufacturing cost and decreasing production yield [69].

To achieve simple yet effective and controlled surface patterning, the laser interference patterning has been developed in the past to fabricate surface microstructures with simple and fast process [79-81]. Interferencing two or more high-power pulsed laser beams allows direct creation of surface features with well-defined periodic array of patterns not only to polymers but also to other surfaces. While the conventional plasma dry etching and laser interference lithography method require additional photolithography

steps, the laser interference ablation patterning technique needs only a simple preparation step, permitting rapid fabrication of the surface patterns with high design flexibility. In addition, relatively large areas can be directly patterned in a short time by manipulating the configuration of the laser beam optics.

1.6 Scope of this Dissertation

Group III-nitride compound semiconductors have drawn enormous attention as one of the most important semiconductors due to their advantages of direct- and wide-bandgap nature, superior thermal and chemical stability, and the intrinsic high carrier mobility, high breakdown field, and capability of forming heterostructures. Among many potential devices based on the Group III-nitride semiconductors, this work will describe the GaN-based visible light-emitting diodes (LEDs) demonstrating the engineering of carrier dynamics with respect to efficiency droop and the enhancement of light extraction efficiency by direct laser ablation. In addition, the growth of InAl(Ga)N epitaxial layer using MOCVD is discussed. In Chapter 1, a brief introduction to the properties of III-nitride semiconductors and the epitaxial layer growth process are presented together with the current development status and technical challenge of the LEDs. In Chapter 2, the characterization methods of epitaxial layers and devices, which were applied in this study, will be presented. Chapter 3 investigates the carrier transport and corresponding distribution in the visible LED structures by modifying the *p*-type layers that do not belong to the MQW active region. A multiple-wavelength-emitting MQW active region design is adopted to effectively trace the transport of carriers. In Chapter 4, the possible origins and a mechanism of the unintentional gallium (Ga) incorporation in the

InAl(Ga)N epitaxial layers have been systematically investigated. Chapter 5 is devoted to the improvement of light-extraction efficiency of visible LEDs having 2-dimensional array of surface pattern fabricated by three-beam interference laser ablation without damages in the surface layer and MQW active region. Finally, a summary of the studies performed in this dissertation is provided in Chapter 6.

CHAPTER 2

MATERIAL AND DEVICE CHARACTERIZATION

2.1 Introduction

In the research on the group III-nitride semiconductor materials, various kinds of analysis and characterization techniques are indispensable for the growth of high quality epitaxial layers and improving performance of devices. This chapter describes the various characterization techniques to monitor the growth process and analyze various properties of the semiconductor materials and devices.

2.2 *In-situ* Temperature and Reflectance Measurement

The surface temperature of a wafer is one of the most important parameters critically affecting the growth of a semiconductor epitaxial layer using MOCVD. The surface temperature of a wafer influences various aspects of the epitaxial layer growth, including growth rate, mole fraction of alloys, crystalline quality of a grown layer, and the surface morphology. Therefore, careful monitoring and precise control of the surface temperature of a wafer is absolutely indispensable for the epitaxial layer growth.

A thermocouple, located underneath the wafer susceptor/carrier, is typically used to determine the growth temperature. However, since the thermocouple in the growth chamber of MOCVD faces backside of the wafer susceptor/carrier, the actual surface temperature cannot be accurately measured. In addition, limited thermal contact between the wafer susceptor/carrier and the wafer, gas flow on the wafer surface, and rotation of the wafer with certain frequency can be other reasons for the deviation of the measured

growth temperature from the actual surface temperature of the growing layer. Contrastively, optical pyrometer measurement is able to measure the surface temperature of a wafer because the pyrometer is located directly on the wafer surface. The pyrometer evaluates the temperature based on the principle that all objects emit electromagnetic radiation with respect to their temperature above absolute zero. The electromagnetic radiation intensity, emitted by a black body in thermal equilibrium at a certain wavelength and temperature, is represented by Planck's law, as shown in equation (2.1):

$$dP_s = \frac{2}{h^4 c^3} \frac{(\hbar\omega)^5}{e^{\frac{\hbar\omega}{k_b T} - 1}} d\lambda, \quad (2.1)$$

where P_s is the spectral radiation intensity, h is the Planck constant, c is speed of light, ω is frequency, K_b is Boltzmann constant, and T is absolute temperature. The relation between the thermal radiation of a black body and the temperature along with the photon energy is described in Figure 2.1. The thermal radiation is mainly observed in the region with the photon energy less than 1.3 eV (< 950 nm). The emitted radiation power, obtained from the area below the curve, increases with the temperature, and the maximum intensity shifts toward higher photon energy with increasing the temperature.

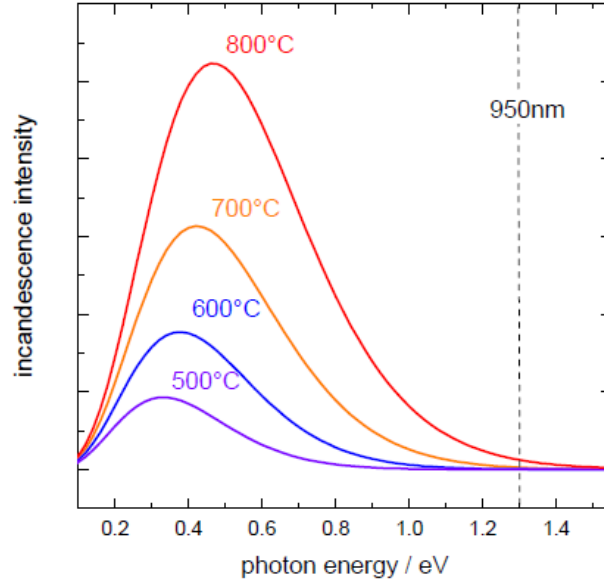


Figure 2.1: Thermal radiation of a black body according to Planck's law [82].

Since the estimation of the surface temperature of the substrate using Planck's law is based on the assumption that the black body shows ideal behaviour concerning the absorption and emission of a radiation, the estimated temperature can lead to large deviation from the actual surface temperature. The optical property and the surface roughness of the real materials result in the modified emissivity. Thus, the emissivity of the real material according to the wavelength and the temperature needs to be corrected to determine the actual surface temperature. The difference of thermal radiation between real body and black body is given by the emissivity, as shown in equation (2.2):

$$\varepsilon(\lambda, T) = \frac{P}{P_s}, \quad (2.2)$$

where $\varepsilon(\lambda, T)$ is the emissivity of a real body, P is thermal radiation of a real body, and P_s is thermal radiation of a black body. The Planck's law corrected by the emissivity is shown as follows:

$$dP = \varepsilon \times dP_s = \varepsilon \frac{2}{h^4 c^3} \frac{(\hbar\omega)^5}{e^{\frac{\hbar\omega}{k_b T} - 1}} d\lambda, \quad (2.3)$$

The emissivity of the growing material should be determined exactly to accurately measure the surface temperature. However, the emissivity often changes during MOCVD growth processes due to the shift of the electronic energy bandgap according to temperature and alloy composition transition. In addition, the multiple reflections of the thermal radiation at the surface and interfaces between different layers lead to constructive or destructive interference, resulting in an intensity modulation depending on the layer thickness. The modulated thermal radiation intensity during epitaxial layer growth is shown in Figure 2.2. While the fluctuation is used for estimating the growth rate in the reflectance measurement, it gives a false signal or a non-existing change in temperature.

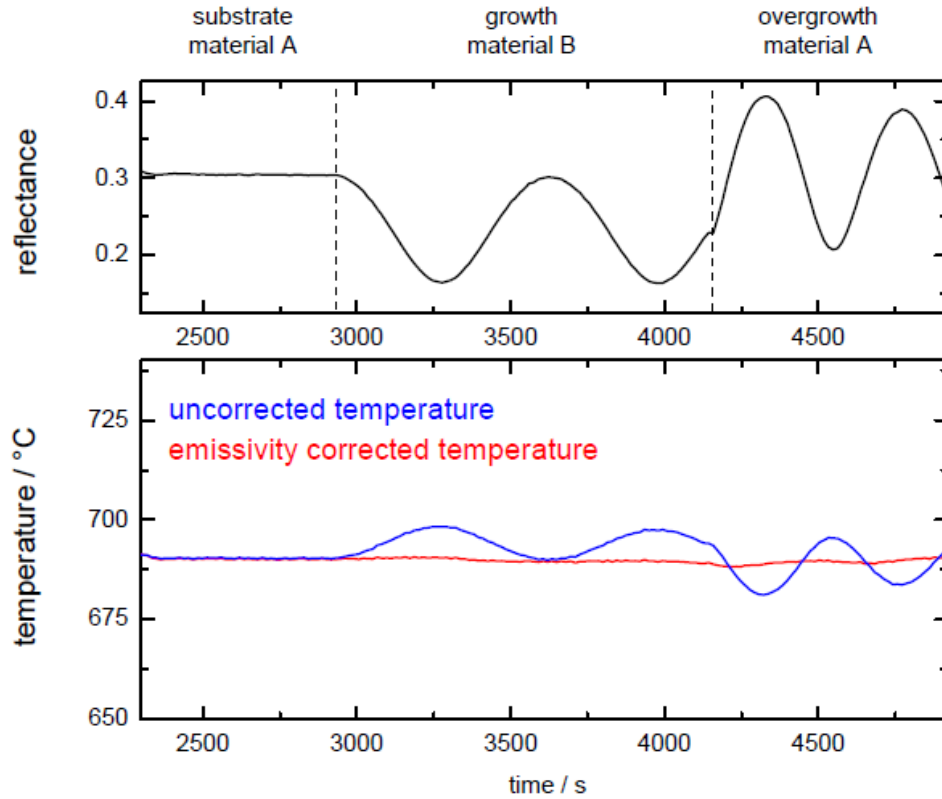


Figure 2.2: True temperature measurement during the growth of the heteroepitaxial layer [82].

To determine the actual emissivity of the wafer, the reflectance measurement of the wafer by using the same wavelength that is used for detecting thermal radiation intensity is required simultaneously with the temperature measurement. During the reflectance measurement, the wafer is illuminated with a light source and a detector measures the intensity of the reflected beam. Since the sum of absorption coefficient α , reflectance coefficient R , and transmission coefficient equals unity according to the conservation of energy, the absorption of the opaque material where no transmission takes place can be achieved by following equation (2.4):

$$\alpha = 1 - R, \quad (2.4)$$

In addition, the absorption equals the emissivity of the material according to Kirchhoff's Law, as described in the following equation (2.5):

$$\alpha(\lambda, T) = \varepsilon(\lambda, T). \quad (2.5)$$

As shown in Figure 2.2 as a red line, the true temperature can be estimated by the corrected emissivity directly derived from the reflectance measurement. However, this emissivity correction can only be applied to the wafer with opaque and smooth surface. In cases of using transparent substrates such as SiC and sapphire, the pyrometer measures the underlying wafer susceptor/carrier and estimates the temperature with certain deviation (ΔT). To compensate this deviation, the absolute temperature of the wafer susceptor/carrier is firstly determined by melting point measurement or pyrometry at two different wavelengths. Next, the temperature of the wafer is determined from its optical properties. The difference of temperature, ΔT , can be obtained from the two temperature measurements, which can be used for compensating the temperature measured by pyrometer during epitaxial layer growth.

The optical reflectance measurement during epitaxial layer growth enables to monitor the properties of the growing layers such as growth rate, epitaxial layer thickness, surface roughness, and composition of ternary material. Thus, the measurement of optical reflectance is essential for the calibration and controlling the growth process in the MOCVD and MBE system.

The light source with a certain wavelength is illuminated on to the growing layer. A detector that is typically a photodiode or a CCD array measures the reflected beam intensity. When the growing layer is transparent at the wavelength of the incoming light, the incident beam is partially reflected at the growing surface, and the remaining part of the beam penetrates the layer and is reflected at the interface between the growing layer and substrate. Since these reflected beams has different phase, the interference takes place between reflected beams takes, and the superposition of all reflected beams generates the overall intensity. The interference between the reflected beams from different interface leads to an oscillation of intensity signal, known as Fabry-Perot oscillations. The reflection of the incident beam at the surface of transparent layer and the substrate is schematically illustrated in Figure 2.3.

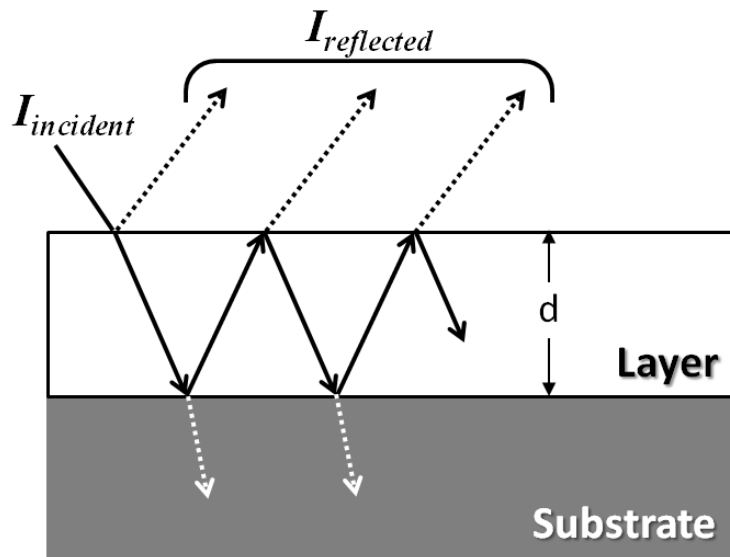


Figure 2.3: Reflections of the incident beam at the surface of transparent layer and the substrate.

The phase difference of the incident beam is depending on the thickness of the growing epitaxial layer, optical properties of the material, and the wavelength of the incident beam. The path difference between beams should satisfy the following equations:

$$2nd = m\lambda, \quad (2.6)$$

and

$$2nd = \left(m + \frac{1}{2}\right)\lambda, \quad (2.7)$$

where n is the refractive index of the layer, m is an even number, d is the thickness of the layer, λ is the wavelength of the incident light. Thus, the layer thickness can be calculated from the intensity oscillations of the reflected light and refractive index of the layer. Moreover, since the layer thickness increases with the growth time, the growth rate can be calculated by following equation (2.8):

$$R_g = \frac{d}{t} = \frac{m\lambda}{2nt}, \quad (2.8)$$

where R_g is the growth rate, d is the thickness of the layer, t is the growth time of the layer. The short period of the intensity oscillation indicates the high growth rate, while the low growth rate leads to long intensity oscillation period. The evaluation of the complete profile of the reflectance behaviour during epitaxial layer growth leads to more accurate information including layer composition and the surface roughness as well.

2.3 Atomic Force Microscopy

Atomic force microscope (AFM) is one of scanned-proximity probe microscopes, measuring local surface property on an object with a metal or semiconductor tip. It was developed to investigate the electrically non-conductive materials and can be applied to observe the solid surfaces and to provide the surface roughness and topographical information. The schematic illustration of the operation of the AFM is schematically illustrated in Figure 2.4.

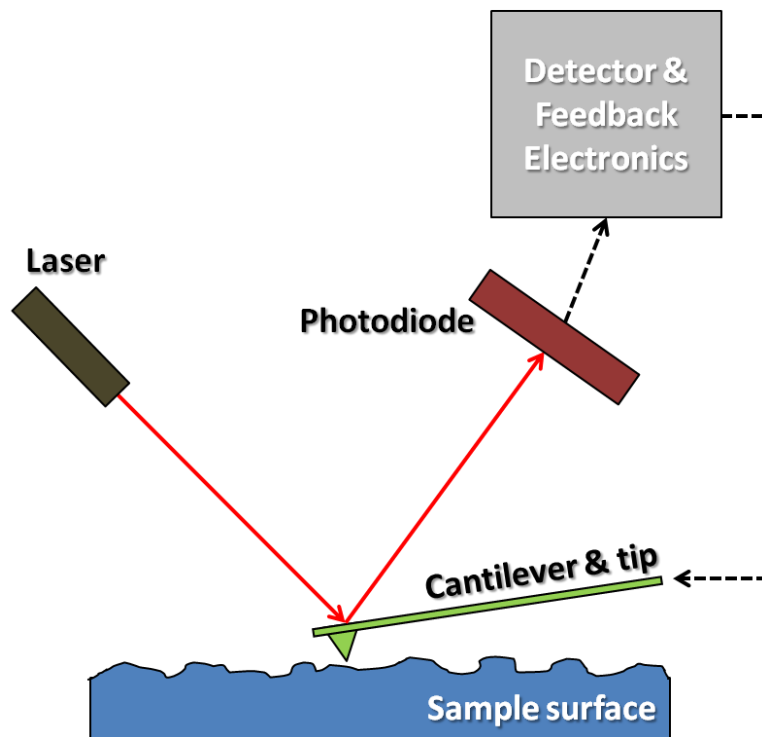


Figure 2.4: Schematic illustration of the operation of an AFM system.

The probe tip travels on the sample surface to achieve the surface morphology and topographical information. The attractive and repulsive forces arising between the sharp tip and the atoms on the surface bend the flexible cantilever according to the surface morphology. The cantilever deflects up and down according to the surface morphology, and the amount of bending of the cantilever is measured optically by the reflection of the laser beam reflected at the backside of the cantilever. The position sensitive photodiode, measuring deflection of cantilever, converts the laser spot into the corresponding electronic current signal and the computer generates an artificial image of the measured surface morphology.

There are three distinct working modes for the AFM measurement. In the contact mode, the tip and the surface of the sample are in physical contact and the surface scan is performed while the deflection of cantilever is kept constant. Since the tip is simply dragged on the surface, the frictional and adhesive forces occurred during the contact mode operation can result in damages on the measured sample and the tip. In the non-contact mode, however, the tip does not touch the surface of the sample and the tip floats several hundreds of angstroms above the sample surface, while the cantilever is oscillated at a frequency slightly above its resonance frequency and the amplitude of the oscillation is kept constant. The interaction between the tip and the sample surface generates the frequency shift of the oscillation, and the feedback loop system maintains constant oscillation amplitude or frequency by adjusting the average distance between the tip and sample surface to draw an image of the sample surface. In the non-contact mode, a contaminant layer can interfere with oscillation of the cantilever, hampering the surface measurement and generally providing low resolution. The tapping mode is somewhere

between the contact and non-contact mode. The cantilever oscillates with the resonance frequency and the tip lightly taps on the surface during scanning. The tapping mode takes advantages of the two different modes mentioned above, so that it provides higher resolution with minimum damage of the sample surface and the tip. This is because the tip intermittently contacts the surface and oscillates with sufficient amplitude, resulting in elimination of frictional forces and prevention of the tip from being trapped by adhesive forces on the surface of the sample. The AFM system used in this study is Veeco Dimension 3100, operating in the tapping mode with NSC Series 16 probes.

2.4 Scanning Electron Microscopy

Scanning electron microscopy (SEM) is used for observation of sample surfaces, providing a largely magnified image by using electrons instead of light to form an image. A beam of electrons produced by an electron gun located at the top of the microscope is focused into a fine spot on the sample surface and scanned across the surface of the sample in a rectangular raster pattern. Once the electron beam hits the surface of the sample, electrons and X-rays created by interactions between the electron beam and the sample are ejected from the surface of the sample. Detectors collect these X-rays, backscattered electrons, and secondary electrons and convert them into a various signal. The secondary electron signal is the most frequently used signal. The output signals from the detector are amplified and then transferred to the screen. The electron optical system and the chamber must be kept at a high vacuum to prevent the electron beam from random discharge resulting in instable electron beam, enabling the electron beam to travel in straight lines to the surface of the sample without interruption by the presence of other

gas molecules. The SEM images used in this study are taken from Hitachi S-4700 FE-SEM that is a cold field emission high resolution SEM, permitting ultra high resolution imaging of thin films and semiconductor materials.

2.5 Secondary Ion Mass Spectrometry

Secondary ion mass spectrometry (SIMS) is a widely used technique for analysis of dopants and impurities with very low concentrations in solid materials and the measurement of the atomic concentration in semiconductors and thin films. SIMS measurement is based on the observation of charged particles that are emitted from a sample surface by the bombardment of a primary ion beam. The ejected secondary ions of interest are transferred and isolated by extraction lens and mass analyser. The ion detection system records the magnitude of the secondary ion signal. The schematic illustration of SIMS measurement is shown in Figure 2.5.

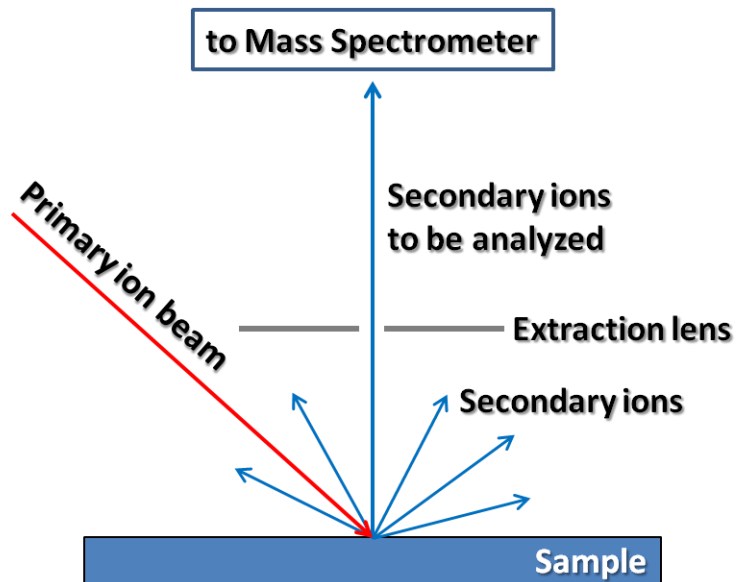


Figure 2.5: Schematic illustration of SIMS measurement.

As a primary ion beam source, usually O_2^+ , O^- , Cs^+ , Ar^+ , Ga^+ or neutrals were used to supply the bombarding species. While the static SIMS mode is suitable for sub-monolayer elemental analysis using a primary ion beam having low energy, the dynamic SIMS mode can be used for achieving compositional information as a function of depth. Since the dynamic SIMS technique uses the primary ion beam exceeds the static limit, producing a high yield of secondary ions, it is useful for determining dopant and impurity depth profiles over a depth ranging from a few angstroms to tens of microns.

2.6 Rutherford Backscattering Spectrometry

Rutherford backscattering spectrometry (RBS) is widely used for the near surface layer analysis of solids. Ion beam having energy in the MeV-range (typically 0.5~4 MeV) bombards the sample, and the energy of the backscattered projectiles is recorded with an energy sensitive detector. The quantitative analysis of the mole fraction of a material and the depth profiling of individual elements are available without reference samples. Moreover, in contrast to the SIMS measurement, RBS is non-destructive method. The analyzed depth of the depth profiling is approximately 2 μm for the incident He-ions and 20 μm for the incident protons with a good depth resolution and a good sensitivity for heavy elements. However, RBS has low sensitivity for light elements, so that the combination of other measurement techniques such as nuclear reaction analysis (NRA) or elastic recoil detection analysis (ERDA) is required to measure the composition of light elements of a material. The RBS spectrum shown in this study was acquired with the collimated He^{++} ion beam energy of 2.0 MeV and beam current of 3 nA, and the XRUMP software was used to determine the alloy composition from the peak positions and signal

intensities. The error range of RBS analysis including XRUMP is estimated to be less than 2-4 % in composition of each group III element.

2.7 Photoluminescence

Photoluminescence (PL) is the optical emission of light from a material and is obtained by photon excitation. Since the measured sample is excited optically, the PL measurement is contactless and non-destructive method to obtain information on the optical quality of a material and thus, it is a widely used technique in the analysis of the optoelectronic device structures composed of semiconductor materials. The electron-hole pairs are generated in the material by irradiating a laser beam having energy greater than the electronic energy bandgap of the material on the sample under equilibrium state, which is followed by the spontaneous emission of photons through the radiative recombination of the electron-hole pairs. The number and the wavelength of emitted photons resulted from the radiative recombination are collected by detectors and analyzed in a spectral distribution of the PL intensity, providing information on electronic energy bandgap of the semiconductor material using following equation (2.9):

$$E_g = h\nu = \frac{hc}{\lambda}, \quad (2.9)$$

where E_g is the electronic energy bandgap of the semiconductor material, h is Planck constant, c is the speed of light, and λ is the wavelength of the emitted photons. In addition to the determination of electronic energy bandgap of a semiconductor material, the quantity of PL is directly related to the relative amount of radiative and non-radiative

recombination rates. Because the non-radiative recombination rates are closely associated with the defects such as impurities and dislocations, the PL measurement can qualitatively evaluate the material quality. The PL measurement system used in this study is Accent RPM2000 equipped with a 266 nm Q-switched Nd:YAG laser as an excitation source. The laser powers attenuated up to $7.5\times$ by the attenuators can be controlled from 0.4 mW to 3.1 mW. This PL system can cover a wide spectral detection range, defined by the choice of gratings, excitation lasers, detectors and order of sorting filters.

2.8 Electroluminescence

Electroluminescence (EL) is the photon emission resulted from the radiative recombination of excess carriers, which are electrons and holes, injected into the material. EL measurement is a widely used technique to characterize the optical properties of an optical device structure. In contrast with PL measurement, which uses photon excitation to generate electron-hole pairs, EL measurement employs the injection of electrons and holes through electric current. Thus, the measured sample needs to form a complete device structure having electrical contact layers for the injection of the excess carriers. In LEDs, the radiative recombination of the injected excess carriers occurs in the active region, and the emitted photons at the electronic energy bandgap of the active region are detected and analyzed in the same manner as PL measurement. However, EL measurement can yield the emission characteristics and the emission intensity of an actual device in operation as well as the emission spectra. Moreover, current-voltage plot can be simultaneously measured, which gives information on the electrical performance of the device. The EL measurement system used in this study is composed of a Keithley

Model 2400 Series Source Meter as a current source, Ocean Optics HR2000-CG-UV-NIR spectrometer equipped with a composite-grating and a 2048-pixel CCD Linear Image Sensor, and LabVIEW[®] software for a control of the system.

2.9 Transmission Line Measurement

The transmission-line measurement (TLM) has been used for contact analysis including the contact resistance between metal and semiconductor and sheet resistance of the semiconductor layer. The TLM measurement can provide both contact resistance and sheet resistance simultaneously with a simple process and a good accuracy. The TLM method involves making a mesa etching around TLM patterns to restrict the current flow only between metal contact pads along the one direction. After making mesa definition on the semiconductor, the metal contact pads separated by various distances are deposited on the top of the mesa area. The typical linear TLM pattern separated by the different spacing between metal contact pads is schematically illustrated in Figure 2.6.

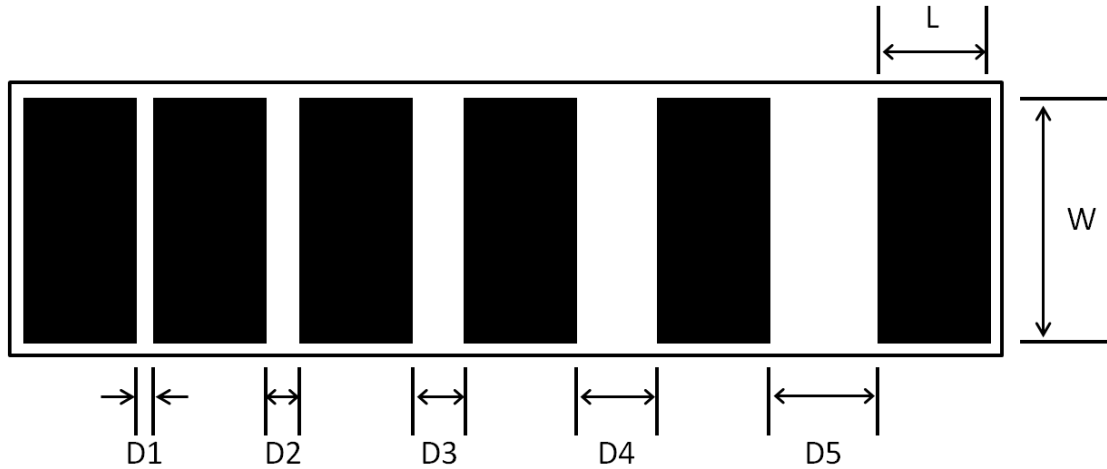


Figure 2.6: A typical linear TLM pattern showing the semiconductor mesa with metal contact pads separated by different distances.

The parameters shown in Figure 2.6 are used for measurements and calculations of resistance: D is the spacing between metal contact pads (μm), L is the length of a rectangular metal contact pad (μm), and W is the width of a rectangular metal contact pad (μm). The values for the contact resistance R_C and the sheet resistance R_S can be obtained from the extrapolation of resistances as a function of the metal contact pads spacing, as shown in Figure 2.7.

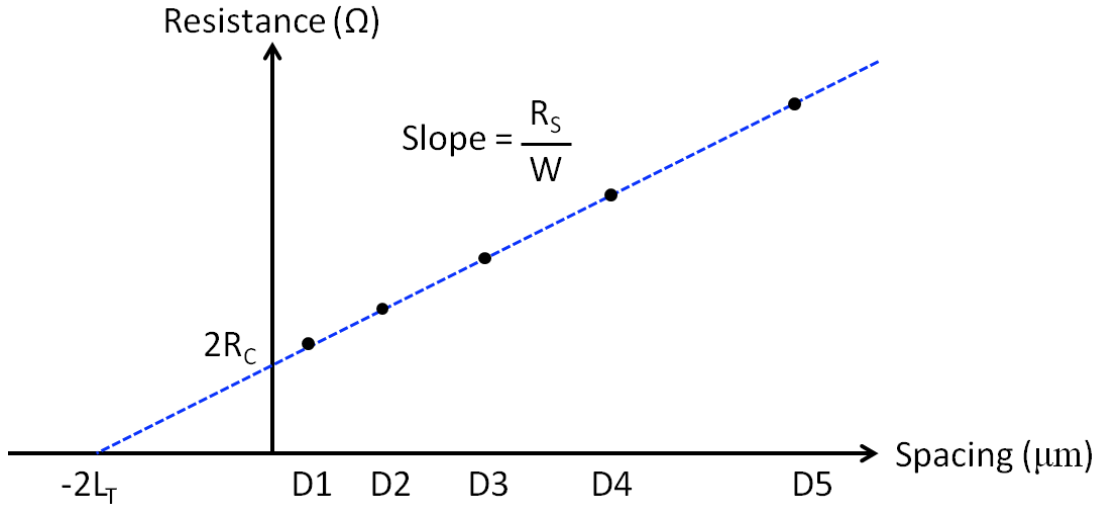


Figure 2.7: Plot of the measured resistance as a function of the distance between the metal contact pads.

The sheet resistance of the semiconductor layer can be calculated from the slope of the linear plot, as shown in following relation:

$$R_s = Slope \cdot W, \quad (2.10)$$

The y-intercept and the x-intercept of the linear plot described in Figure 2.7 indicate twice the contact resistance, $2R_C$, and twice the transfer length, $2L_T$, respectively. The transfer length is defined as the distance from the edge of the metal pad to the point that the contact voltage is $1/e$ of its maximum value. With these parameters, the specific contact resistance ρ_c that is an important parameter to describe the quality of the Ohmic contact can be calculated from the following equations:

$$R_C = \frac{R_S \cdot L_T}{W}, \quad (2.11)$$

$$\rho_C = L_T \cdot W \cdot R_C = R_S \cdot L_T^2 \quad (2.12)$$

2.10 X-ray Diffraction

The X-ray diffraction (XRD) is a powerful measurement tool used to characterize the structural property of crystalline materials. Due to the convenient and non-destructive characterization, the XRD measurement is widely used to determine the epitaxial layer properties such as crystalline quality, alloy composition, uniformity, thickness, and built-in strain and relaxation. In the XRD technique, an incident X-ray beam collides with a specimen, and the X-rays reflected at the crystal interface of the specimen as well as the surface are measured with the angular information. The diffraction of reflected X-rays occurs with respect to the different crystallographic planes in a crystal, which can be described by Bragg's Law shown in following equation (2.13):

$$n\lambda = 2d_{hkl} \sin \theta_B, \quad (2.13)$$

where n is an integer representing diffraction order, λ is the incident X-ray wavelength, d_{hkl} is the spacing between crystallographic planes, and θ_B is the Bragg angle. Since the incident X-ray wavelength λ is fixed, the inter-planar spacing d_{hkl} can be obtained by measuring the Bragg angle θ_B that is an angle between incident and diffracted X-ray to

the crystallographic planes. The lattice spacing of the plane having Miller indices of (h k l) for a cubic lattice is given by following equation (2.14):

$$\frac{1}{d_{hkl}^2} = \frac{h^2 + k^2 + l^2}{a^2} . \quad (2.14)$$

For a hexagonal lattice, the lattice spacing is expressed as equation (2.15):

$$\frac{1}{d_{hkl}^2} = \frac{4}{3} \left(\frac{h^2 + hk + k^2}{a^2} \right) + \frac{l^2}{c^2} , \quad (2.15)$$

where d_{hkl} is the spacing between crystallographic planes, a and c are lattice constants of the plane, and h, k, and l are the Miller indices of the plane of interest. These equations provide correlations between specific crystallographic planes and Bragg angles for the X-ray wavelength.

All XRD data presented in this dissertation are obtained by using Philips X'Pert[®] MRD (Material Research Diffractometer) high-resolution (0.0001°) X-ray diffractometer. The schematic diagram of a typical configuration of a HR-XRD system is shown in Figure 2.8.

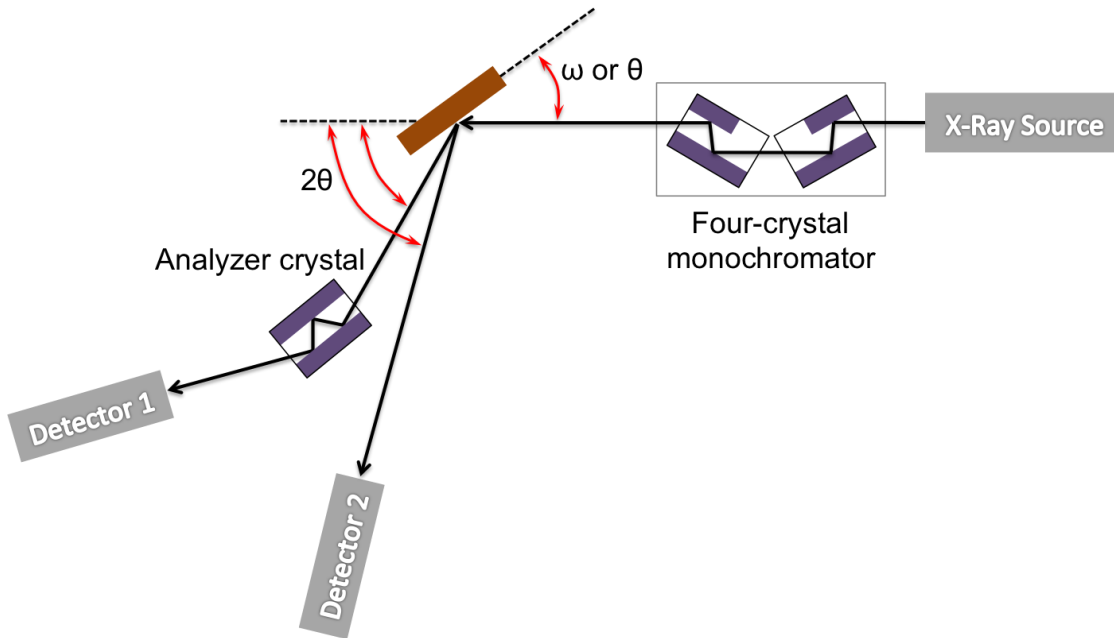


Figure 2.8: Schematic diagram of a typical configuration of a HR-XRD system.

The characteristic Cu $K_{\alpha 1}$ and $K_{\alpha 2}$ radiations having $\lambda=1.5405$ and $\lambda=1.5443$ Å, respectively, are used as the X-ray source. The X-ray is collimated and monochromated by a four-crystal Ge (2 2 0) Bartels monochromator, which enables high angular resolution. The monochromated X-ray beam is incident into the specimen and diffracted from a particular set of planes of the specimen. The diffracted beam is collected by either one of the detectors. In the X'Pert MRD system, the detector 2 is used for the X-ray rocking curve and the detector 1 is utilized for the reciprocal space mapping (RSM).

The rocking curve, which is also known as ω -scan, is one of most commonly employed XRD scan. In this scan mode, the detector is kept at a fixed angle with respect to the primary beam (2θ) while the sample is rotated or rocked relative to the ω axis, perpendicular to the surface of the sample as schematically in Figure 2.8. The symmetric rocking curves are useful not only for obtaining the c lattice constant of relatively lattice-

matched materials but also for determining relative crystalline quality between samples by comparing the full width half maximum (FWHM) or linewidth of the broadened peak. Moreover, asymmetric rocking curves on the planes such as (1 0 2) or (1 0 5) can provide more information because the FWHM of these peaks is sensitive to threading dislocations. However, the angular probing range of the rocking curve is limited to the angle of approximately 1° due to the fact that the detector is not moved along with the sample. Thus, in case of the III-nitride-based epitaxial layers grown on foreign substrate with large lattice mismatch, the information on the lattice mismatch between epitaxial layers and the substrate cannot be obtained in the same rocking curve because the Bragg angles for the epitaxial layers are much smaller than that of the substrate.

The ω - 2θ scan is the alternative technique for the characterization of the highly mismatched epitaxial layers. The detector moves at twice the angular rotation rate as the sample so that the measured diffraction angle remains to be always 2θ with respect to the incident beam angle. Therefore, the diffraction peaks become narrower, minimizing the overlap of the diffraction spectra between layers, enabling the accurate analysis of the each epitaxial layer.

The two-dimensional scan on the reciprocal space, known as reciprocal space mapping (RSM), can provide more detailed information on the degree of strain and relaxation status between layers, the distortion of lattice-constants, and the composition of the layer as well as crystalline quality. The RSM is obtained through the repeating ω - 2θ scans at different ω value along the reciprocal lattice points, providing the information on the strain condition in the epitaxial layers and the composition of the layer independently. More detailed information on RSM can be found elsewhere [83].

CHAPTER 3

IMPROVEMENT OF HOLE TRANSPORT AND DISTRIBUTION IN THE VISIBLE LIGHT-EMITTING DIODES

3.1 Introduction

The peak luminous efficiencies of LED-based lamps far exceed those of incandescent and fluorescent lamps at relatively low currents. However, the efficiency of LED lamps at high currents diminishes with increasing drive currents. This efficiency droop poses a major technical challenge for LED lamps used in high power lighting. Uniform carrier distribution into multiple-quantum-well (MQW) active region has recently been proposed as a way to mitigate the efficiency droop [33, 34]. To accomplish the uniform distribution of carriers, effective hole transport across the MQW active region is considered to be a key factor. The limited hole transport into the active region and the non-uniform hole distribution among the MQWs result not only from the relatively large effective hole mass but also from the specific characteristics of the QWs, quantum barriers (QBs), and electron blocking layers (EBLs), such as potential barrier height, thickness, and doping of those layers [29-35]. The engineering of MQW design for the improvement (mitigation) of efficiency droop is, however, in many cases, not easy to be implemented by observed phenomena that the mitigated efficiency droop is often achieved at the expense of internal quantum efficiency (IQE) of the LEDs. In the present study, the engineering of carrier dynamics by modifying the layers that do not belong to the active region is focused on. The effect on the hole transport in the active region and resulting hole distribution among the MQWs by controlling the indium (In) mole fraction

in p -type $\text{In}_x\text{Ga}_{1-x}\text{N}:\text{Mg}$ layers of the LED structures will be reported. p -InGaN layers replacing p -GaN have been demonstrated to result in reduced thermal damage to “true” green MQW active region [84], enhanced electrical and optical properties of green LEDs [85], and mitigation of the quantum-confined Stark effect [86]. In addition to those beneficial effects by p -type $\text{In}_x\text{Ga}_{1-x}\text{N}:\text{Mg}$, enhanced hole transport in the MQW active region is demonstrated in this work. A dual-wavelength (DW)- and a triple-wavelength (TW)-emitting MQW design containing different-color InGaN QWs was employed to effectively trace the emitted photons from the active region. In the multiple-wavelength emitting MQWs structure, each QW emits its own characteristic wavelength that can be used to experimentally evaluate the transport and distribution of holes in the active region.

3.2 Growth and Fabrication of the LED Structures

Epitaxial growth was carried out by metalorganic chemical vapour deposition in a Thomas-Swan (now Aixtron) reactor system equipped with a close-coupled showerhead chamber. LED epitaxial layer structures on sapphire substrates consist of an n -type Si-doped GaN (n -GaN:Si) layer, a DW- or TW-InGaN/GaN QW/QW barrier (QWB) active region, and p - $\text{In}_x\text{Ga}_{1-x}\text{N}:\text{Mg}$ layers. The schematic illustration of epitaxial layer structure of the LEDs having DW- and TW-MQW active region designs is shown in Figure 3.1.

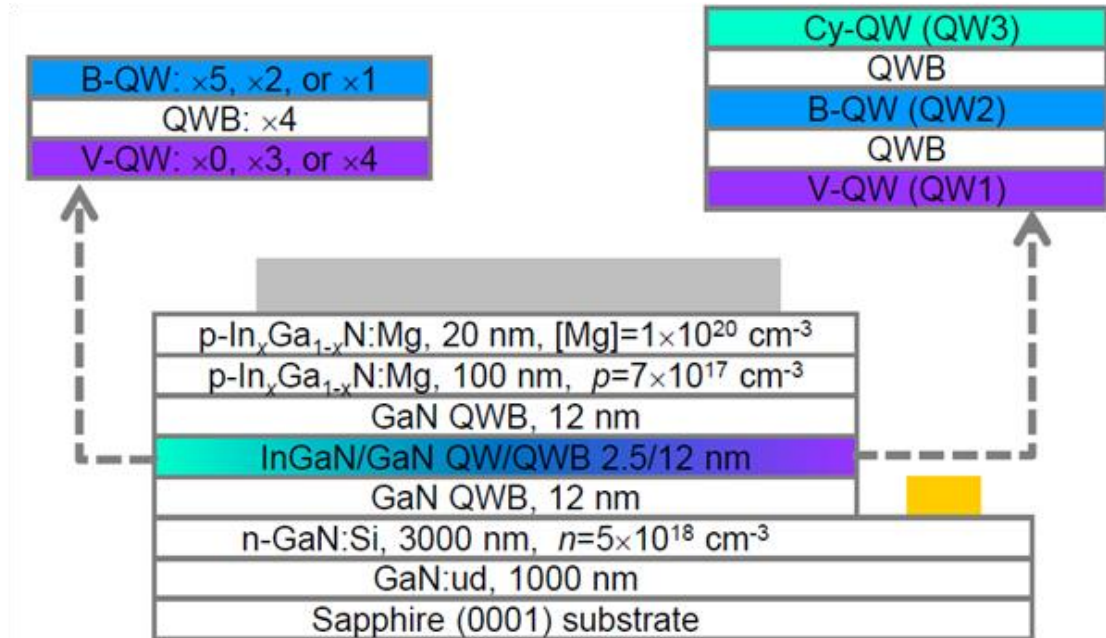


Figure 3.1: Schematic illustration of epitaxial layers of double-wavelength (DW) and triple-wavelength (TW) light-emitting diodes (LEDs) with different indium (In) mole fractions ($x_{In} = 0, 1.5, 2.5,$ and 3.5 %) in p -type layers.

The In mole fraction, x_{In} of the p - $In_xGa_{1-x}N:Mg$ layers was selected in the range of 0 ~ 3.5 %. To obtain corresponding In mole fraction in the p - $In_xGa_{1-x}N:Mg$ layers, the growth temperature was varied during the epitaxial layer growth. An unintentionally-doped GaN (GaN:ud) layer was grown between the last QW and the p -type layer, as a QWB. The doping of the p - $In_xGa_{1-x}N:Mg$ layers was carefully controlled to be same at $p \sim 7 \times 10^{17} \text{ cm}^{-3}$, not necessarily the highest doping level for each p - $In_xGa_{1-x}N:Mg$ layer, to eliminate an unintended effect of p -type doping concentration on the injection and transport of the holes. Also, QWs were located in such a way that the QW having the widest bandgap was close to the n -layer and the QW having the narrowest bandgap close to the p -layer, and the photon recycling effect is believed to be negligible. Since this

study focuses on the effect of different p -type layers on the hole injection and transport across the MQWs, an EBL was intentionally excluded in the LED structures to eliminate the complicated effects on peak efficiency and efficiency droop caused by potential barriers and spontaneous and piezoelectric charges near p -InGaN/EBL and EBL/GaN:ud interfaces.

To investigate the crystalline quality of multiple-wavelength-emitting MQW active region, high-resolution transmission electron microscopy (HR-TEM) was employed. A bright-field, cross-section HR-TEM image of a triple-wavelength (TW) emitting MQW active region structure on [11-20] zone axis is shown in Figure 3.2.

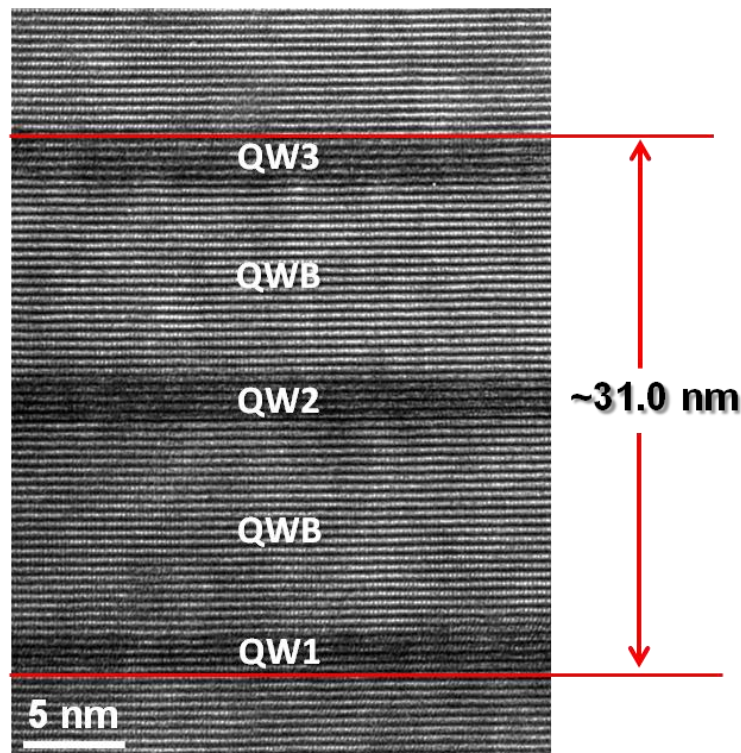


Figure 3.2: The bright-field, cross-section HR-TEM image of the triple-wavelength (TW) emitting MQW active region in a TW-LED structure on [11-20] zone axis.

The HR-TEM image shows the uniform thickness with abrupt interfaces of the MQW active region composed of 3 pairs of QW/QWB (three QWs and two QWBs). The total thickness of the MQW active region is estimated as 36 nm, which is well agrees with the designed thickness of QW (2.5 nm) and QWB (12 nm).

The epitaxial structures of multiple-wavelength emitting LEDs were fabricated into wafer-level LED devices using a standard device fabrication process. Surface cleaning, photolithography (PR), and dry etching using inductively-coupled plasma reactive ion etching (ICP-RIE) processes were implemented to achieve the mesa definition having a mesa size of $350 \times 350 \mu\text{m}^2$. A Ti/Al/Ti/Au *n*-Ohmic and a reflective $\text{Ni}_x\text{O}_{1-x}/\text{Ag}$ *p*-Ohmic contact metals were deposited by an electron-beam evaporation followed by a thermal annealing. An optical microscope image of a fabricated wafer-level LED chip is shown in Figure 3.3.

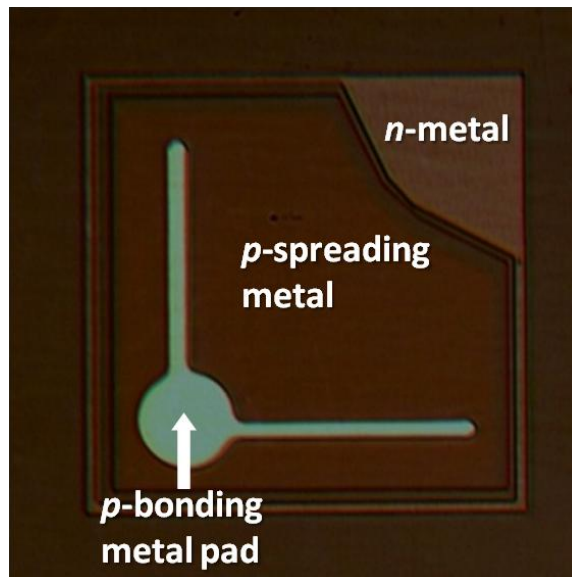
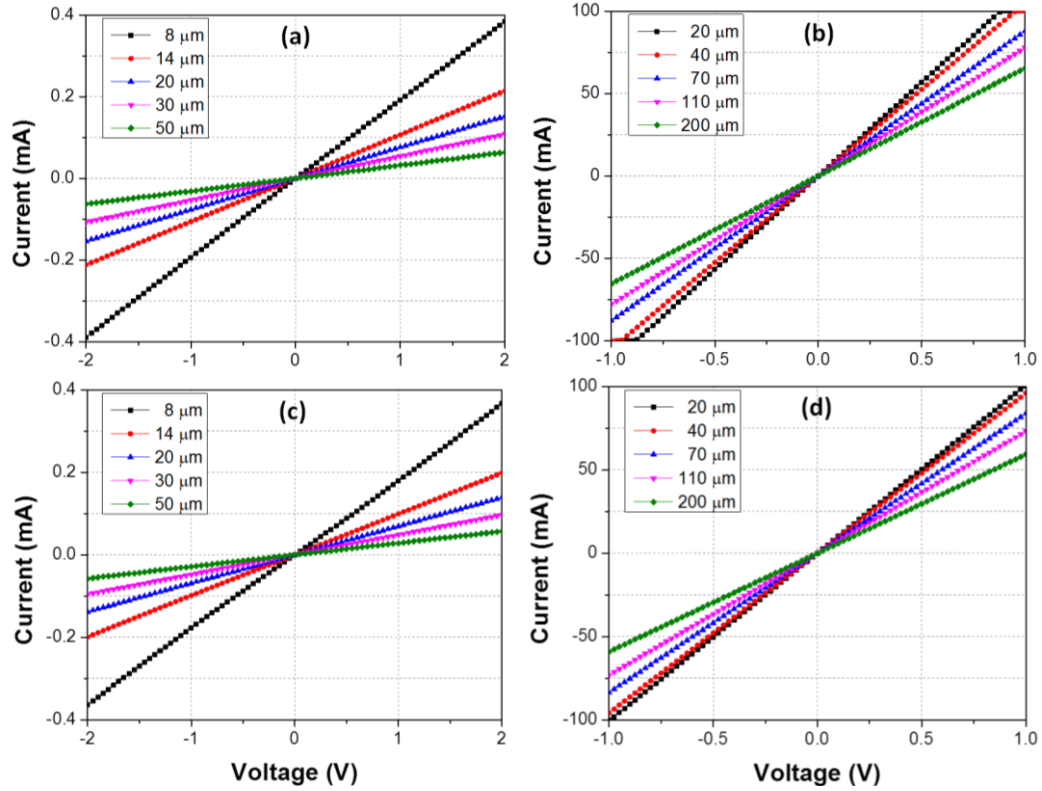


Figure 3.3: An optical microscope image of a wafer-level LED chip with the device size of $350 \times 350 \mu\text{m}^2$.



(a) p -TLM results of LED with p -GaN,
(c) p -TLM results of LED with p -InGaN,

(b) n -TLM results of LED with p -GaN,
(d) n -TLM results of LED with p -InGaN

Figure 3.4: TLM I - V comparisons for p -layers and n -layers of LEDs with different p -type layers.

To investigate the uniformity of electrical properties of the p -type and n -type layers employed in the DW- and TW-LED structures, the transmission line measurements (TLM) were implemented for the LEDs with p -GaN and p -In_{0.035}Ga_{0.965}N layers. The mesa etching around TLM patterns was performed to restrict the current flow only between contact pads along the one direction. The width and length of a contact pad are 200 μm 50 μm , respectively, and the gaps between the metal contact pads are 8/14/20/30/50 μm for p -type layers and 20/40/70/110/200 μm for n -type layers. The current-voltage (I - V) measurement results of the TLM patterns are shown in Figure

3.4(a), (b), (c), and (d). In the TLM results of both p - and n -type layers, the measured I - V curves show a good linearity without a noticeable Schottky contact behaviour, demonstrating that the contacts between the metal pads and the semiconductor layer have good Ohmic characteristics. The specific contact resistances (R_c) and the sheet resistances (R_{sh}) of the p - and n -type layers were obtained from the linear fitting of the total resistances of each gap, calculated from the measured I - V curves. The slopes and y -intercepts of the linear fitting of the total resistances refer to the R_{sh} and the R_c , respectively. The values of the R_{sh} and the R_c of the p - and n -type layers are listed in Table 3.1. For the comparison between p -GaN layer and p -In_{0.035}Ga_{0.965}N layer, no significant differences in the values of the R_{sh} and R_c are observed, indicating that the LEDs having different p -type layers have similar electrical properties in the p -type layers. In addition, the values of the R_{sh} and R_c of the n -type layers used in the LEDs with different p -type layers are uniform without significant differences, which also indicates the similar electrical properties of n -type layers.

Table 3.1: The sheet resistance and specific contact resistance of the p -type and n -type layers in the LEDs with p -GaN and p -In_{0.035}Ga_{0.965}N layers

Layer	LED with p -GaN layer			LED with p -In _{0.035} Ga _{0.965} N layer		
	R_{sh} (Ω)	R_c (Ω -cm ²)	R^2	R_{sh} (Ω)	R_c (Ω -cm ²)	R^2
p -layer	123.1 K	1.99×10^{-4}	0.998	138.9 K	1.98×10^{-4}	0.999
n -layer	7.66	8.55×10^{-4}	0.973	7.95	1.04×10^{-3}	0.996

3.3 Characterization of the Dual-wavelength LEDs

The dual-wavelength (DW)-LEDs with different *p*-type layers of *p*-GaN and *p*-In_{0.035}Ga_{0.965}N layers are characterized. The MQW active region of the DW-LEDs is composed of various combinations in 5-QWs of $\lambda \sim 420$ nm (violet, V) and $\lambda \sim 480$ nm (blue, B), which are *n*/BBBBB/*p*, *n*/VVVBB/*p*, and *n*/VVVVB/*p*. The thicknesses of the QW and QWB in an In_{*x*}Ga_{1-*x*}N/GaN MQW active region were designed to be 2.5 nm and 12 nm, respectively. During the growth of MQW active region, two different growth temperatures of 740 and 770 °C were used for the B- and V-QWs, respectively, so that the In_{*x*}Ga_{1-*x*}N QWs have different In mole fraction according to the growth temperature, allowing the emission of photons at the proposed bandgap energy.

Regarding quality difference between the MQW active regions of the LEDs with different hole injection layers of *p*-GaN and *p*-In_{0.035}Ga_{0.965}N layer, photoluminescence (PL) measurement was performed for each set of DW-LEDs. In a set of DW-LEDs, the design of the epitaxial layer structure in the MQW active region is the same, that is, an *n*/BBBBB/*p* or an *n*/VVVVB/*p*. The comparison of PL spectra on each set of DW-LEDs with different *p*-type layers is shown in Figure 3.5(a) and (b).

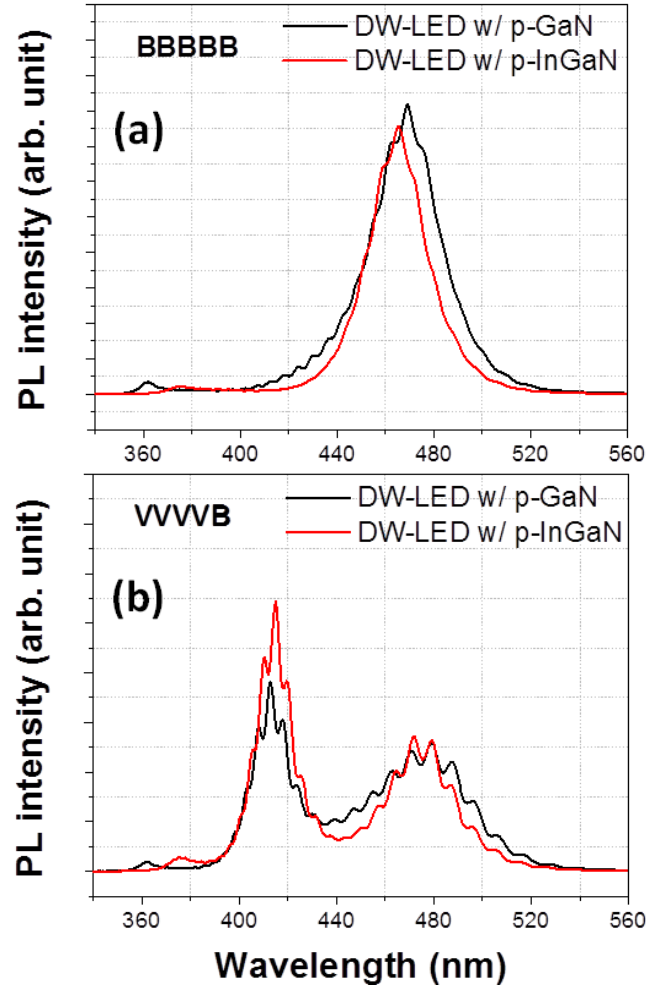


Figure 3.5: The comparison of photoluminescence (PL) spectra on each set of DW-LEDs having different MQW active region structures of (a) n /BBBBB/ p and (b) n /VVVVB/ p with p -GaN and p -In_{0.035}Ga_{0.965}N layers.

No meaningful differences of the PL intensity and the wavelength were observed in each set of DW-LEDs with p -GaN and p -In_{0.035}Ga_{0.965}N layers, as shown in Figure 3.5 (a) and (b). These similar PL spectra support that the quality of MQW active regions between the DW-LEDs with different p -type layers is comparable and the difference in electroluminescence (EL) spectra is likely related to dynamics of carriers that are injected bipolarly.

The electro-optical characteristics of the DW-LEDs with different p -type layers were measured by EL from the wafer-level bottom-emitting LEDs (without packaging). The changes in the ratio of integrated EL intensity of V-QWs to total intensity at a current of $I=80$ mA is shown in the Figure 3.6. In the plots, the total intensity is defined by the sum of the integrated EL intensities of V- and B-QWs. Thus, the ratio of the integrated EL intensity of V-QWs can be described by following equation (3.1):

$$V (\%) = \frac{\text{Emission intensity of V-QWs (V)}}{\text{Total emission intensity (V + B)}} \times 100 \quad (3.1)$$

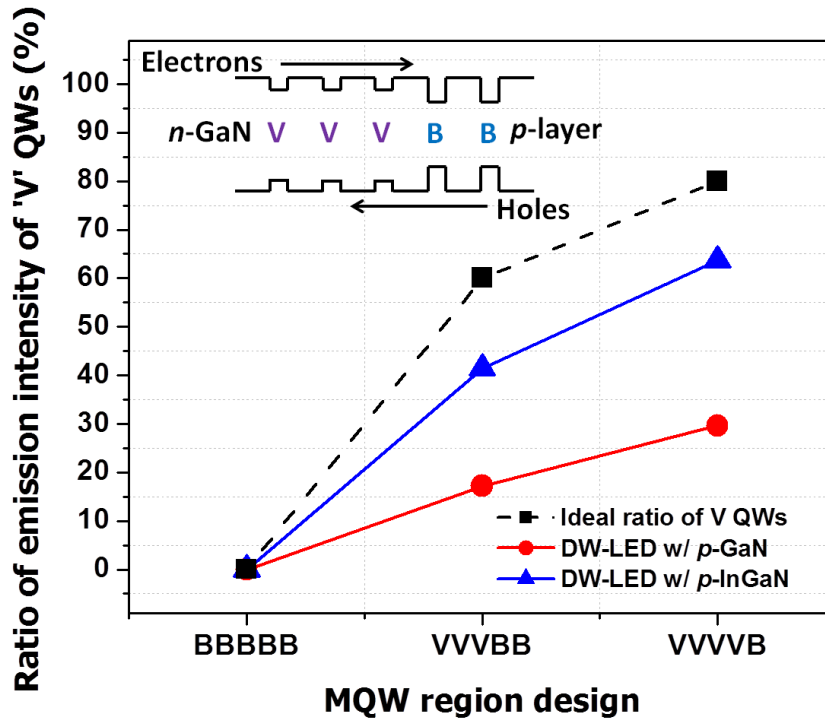
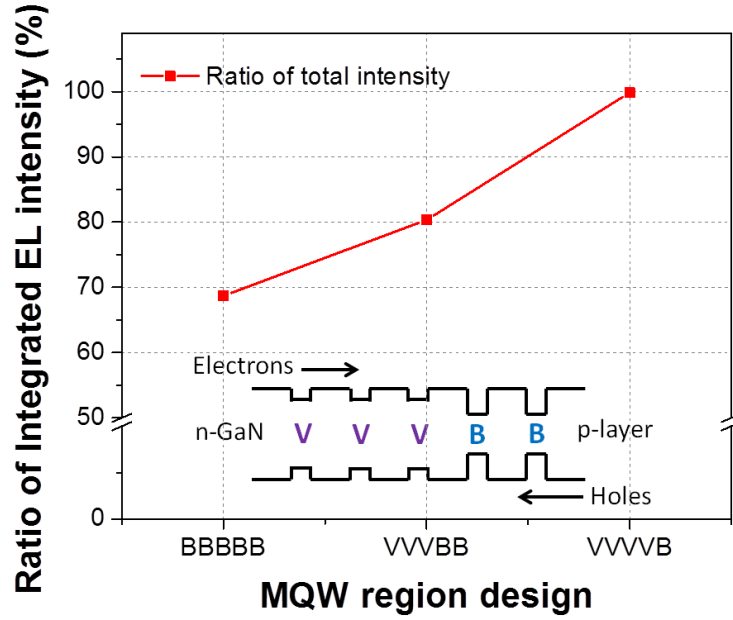


Figure 3.6: Ratio of integrated electroluminescence (EL) intensity of V-QWs to total integrated EL intensity at $I=80$ mA, depending on combinations of V-QWs and B-QWs in LEDs with p -GaN and p -In_{0.035}Ga_{0.965}N layers.

As the number of V-QWs increases, emission from the V-QWs increases at different rates between the LEDs with p -GaN and p -In_{0.035}Ga_{0.965}N layers. While both LEDs have less values of V (%) than the ideal values of LEDs that are assumed to have the same light output from each QW (shown in dotted line in Figure 3.6), the ratios are higher for the LEDs with p -In_{0.035}Ga_{0.965}N layer than those with p -GaN layer. Especially for VVVVB MQWs that have 80 % of V-QWs in active QW volume, the ratio is only 30 % for the DW-LEDs with p -GaN layer, while it is ~64 % for the LEDs with p -In_{0.035}Ga_{0.965}N layer. This indicates that more V-QWs actively contribute to the radiative recombination for the same MQW active region design, when the p -In_{0.035}Ga_{0.965}N is used as an hole injection layer. Considering that electrons are distributed among MQWs uniformly while the population of holes among the MQW active region can be non-uniform [31], the different behaviour in luminescence from V-QWs is possibly attributed to enhanced hole transport across the MQW active region by using p -In_{0.035}Ga_{0.965}N layer.

To further study the behaviour of the hole injection and transport in the MQW active region according to the p -type layers, the ratio of total integrated EL intensities of DW-LEDs with p -In_{0.035}Ga_{0.965}N layers to those of DW-LEDs with p -GaN layers in each set of MQW active region design at an injection current of $I=80$ mA are compared in Figure 3.7



$$\text{Ratio of EL intensity (\%)} = \frac{\text{DW-LED w/ p-InGaN}}{\text{DW-LED w/ p-GaN}} \times 100$$

Figure 3.7: The ratio of total integrated EL intensities of DW-LEDs with $p\text{-In}_{0.035}\text{Ga}_{0.965}\text{N}$ layers to those with $p\text{-GaN}$ layers according to MQW active region design, at $I=80$ mA.

The comparison of the total integrated EL intensities shown in Figure 3.7 shows notable trend that can be explained by hole injection efficiency and hole transport across the MQW active region. For the LEDs containing BBBB MQW active region, total integrated EL intensity of the DW-LED with $p\text{-GaN}$ layer is around 31 % higher than that of the DW-LED with $p\text{-In}_{0.035}\text{Ga}_{0.965}\text{N}$ layer. This is attributed to higher hole injection efficiency of the DW-LEDs with $p\text{-GaN}$ layer than that with $p\text{-In}_{0.035}\text{Ga}_{0.965}\text{N}$ layer. Since the all QWs have the same colour, the hole injection efficiency (total number of holes injected into the MQW active region) dominates the effect on total integrated EL intensity. However, as the number of V-QW increases in the MQW active region, the

difference decreases and finally becomes negligible for the DW-LEDs having VVVVB MQW active region. The difference of total integrated EL intensity of the DW-LEDs with p -GaN and p -In_{0.035}Ga_{0.965}N layer is only 1% in the VVVVB MQWs design. This is explained by combined effect of hole injection efficiency and hole transport. For the DW-LEDs with p -In_{0.035}Ga_{0.965}N layer, total number of holes may be slightly lower but more holes will be populated in V-QWs than the DW-LEDs with p -GaN due to improved hole transport. Since V-QW should have higher internal quantum efficiency than B-QWs, higher radiative recombination rate from V-QW in the DW-LED with p -In_{0.035}Ga_{0.965}N layer should be able to overcome the effect of slightly lower injection efficiency, resulting in almost similar total integrated EL intensities between LEDs with p -GaN and p -In_{0.035}Ga_{0.965}N layers. The hole injection efficiency and effective hole transport according to different p -type layers are further discussed in Chapter 3.6.

3.4 Characterization of the Triple-wavelength LEDs

To further investigate the effect of p -In _{x} Ga_{1- x} N layer, the triple-wavelength (TW)-LEDs having 3-QWs are characterized. The MQW active region of the TW-LEDs has characteristic colors of violet (V, λ ~420 nm), blue (B, λ ~460 nm), and cyan (Cy, λ ~500 nm), designated as QW1, QW2, and QW3 in a sequence of $n/V(QW1)B(QW2)Cy(QW3)/p$ with p -In _{x} Ga_{1- x} N layers. In addition, the x_{In} of the p -In _{x} Ga_{1- x} N layer was controlled to 1.5, 2.5, and 3.5 %, labeled as LEDs A, B, and C, respectively. HR-XRD ω - 2θ scans results with (002) diffraction and PL spectra of the TW-LEDs with p -In _{x} Ga_{1- x} N layers having different x_{In} are shown in Figure 3.8(a) and (b), respectively, to verify the structural and optical properties of the MQW active region.

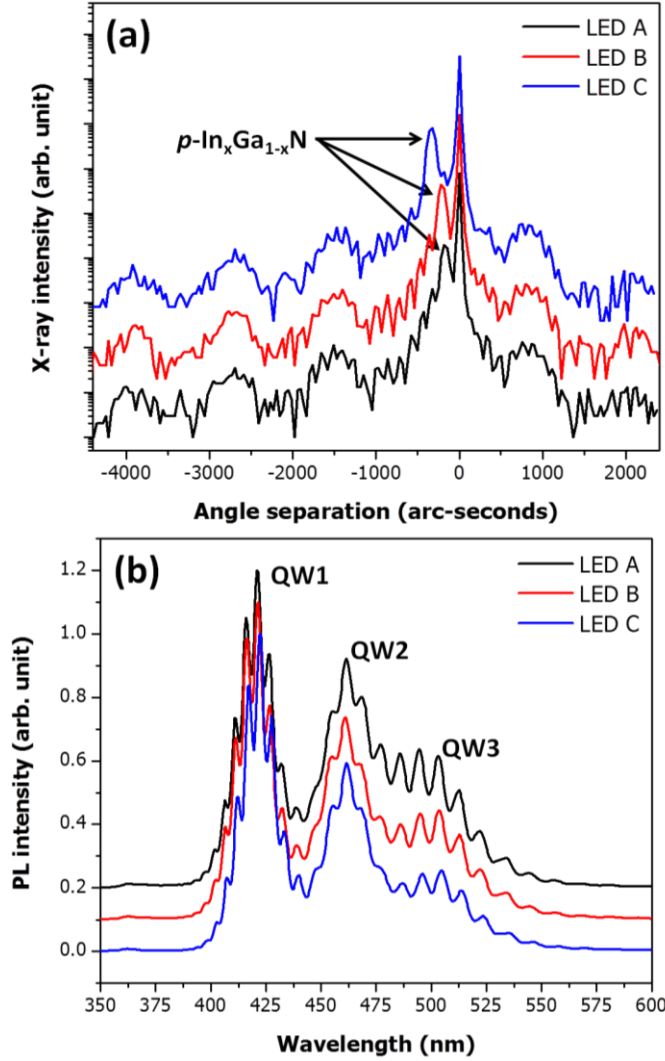


Figure 3.8: (a) HR-XRD ω - 2θ scan results with (002) diffraction and (b) photoluminescence results for TW-LEDs with $p\text{-In}_{0.015}\text{Ga}_{0.985}\text{N}$, $p\text{-In}_{0.025}\text{Ga}_{0.975}\text{N}$, and $p\text{-In}_{0.035}\text{Ga}_{0.965}\text{N}$ layers for LED A, LED B, and LED C, respectively.

X-ray diffraction ω - 2θ scans, shown in Figure 3.7(a), are identical in MQW-related fringe peaks, indicating that the structure of MQW active region including the composition and the thickness of QWs and QWBs are essentially the same for the LEDs A, B, and C. Also, the x_{In} of the $p\text{-In}_x\text{Ga}_{1-x}\text{N}$ layers, confirmed by the XRD dynamical simulation, are 1.5, 2.5, and 3.5 % for LEDs A, B, and C, respectively, and the

differences of x_{In} are responsible for the shift of the $p\text{-In}_x\text{Ga}_{1-x}\text{N}$ layer peak position as indicated by arrows in Figure 3.8(a). In addition to the XRD scan results, the PL spectra, shown in the Figure 3.8(b), have the same shape and intensity for each QW. This also indicates the identical MQW active region structures and optical quality of the LEDs A, B, and C, when the carriers are excited and injected unipolarly by PL, which is different from the case of the EL. The identical MQW active region allows elimination of the possibility of the composition and thickness effects of the MQW active region on the hole transport behaviour.

Electro-optical characteristics of the wafer-level (without packaging) TW-LEDs were measured from the substrate side to minimize absorption by narrower QW. The photon recycling effect is expected to be negligible. The electroluminescence (EL) spectra for the three TW-LEDs were compared to investigate the hole transport behaviour depending on the injection current ranging from 5 mA to 80 mA, as shown in Figure 3.9 (a), (b), and (c).

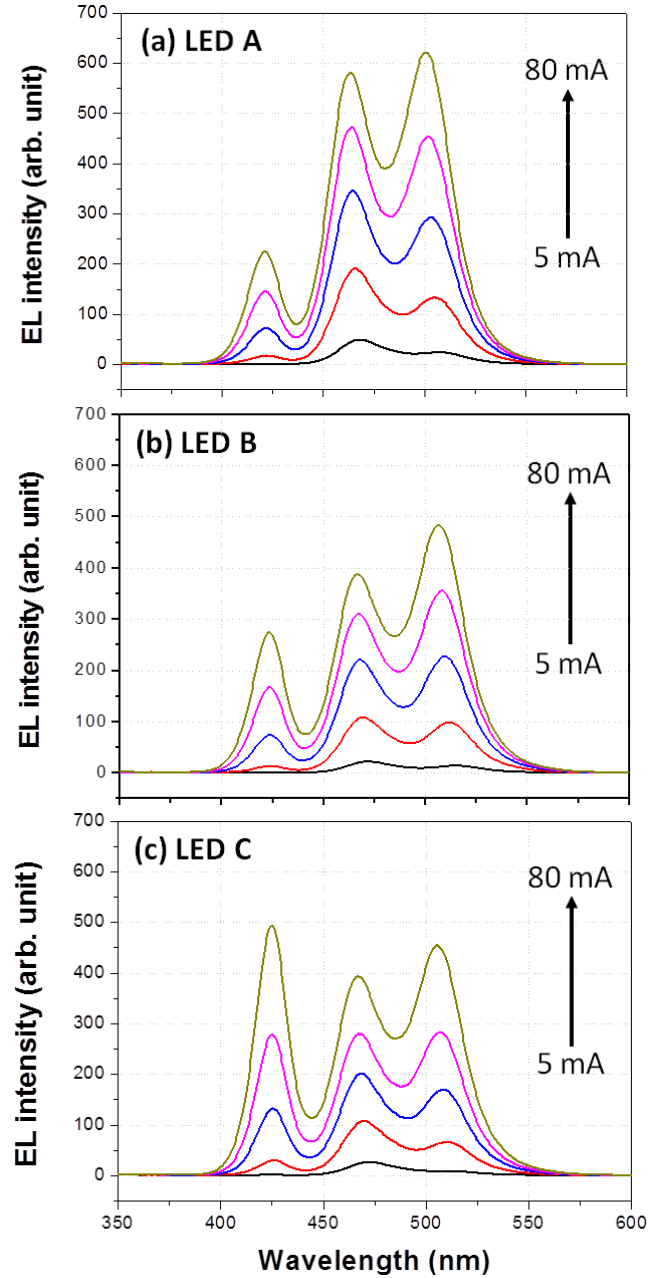


Figure 3.9: Electroluminescence (EL) spectra of (a) LED A, (b) LED B, and (c) LED C with $p\text{-In}_{0.015}\text{Ga}_{0.985}\text{N}$, $p\text{-In}_{0.025}\text{Ga}_{0.975}\text{N}$, and $p\text{-In}_{0.035}\text{Ga}_{0.965}\text{N}$ layers, respectively, at different injection currents.

The EL peak wavelengths for QW1, QW2, and QW3 at $I=20$ mA are $\lambda=423$, 467, and 508 nm for the LED A, $\lambda=424$, 470, and 512 nm for the LED B, and $\lambda=424$, 470, and

509 nm for the LED C, respectively, which suggests the peak emission wavelength was not significantly affected by the difference in $p\text{-In}_x\text{Ga}_{1-x}\text{N:Mg}$ layers.

For the LED A in Figure 3.9(a), QW2 and QW3, having blue and cyan characteristic colors, respectively, show stronger emission than QW1 with violet color. In addition, although the EL peak intensities of all three QWs increase with injection current, the EL peak of QW1 shows lower intensity than those of QW2 and QW3 for the entire injection current range. Assuming the distribution of electrons among TW-QWs is rather uniform, this should be related to the distribution of holes available for radiative recombination, and indicates that the upper QWs adjacent to $p\text{-In}_x\text{Ga}_{1-x}\text{N:Mg}$ layer do emit more photons. Holes have a higher effective mass than electrons (*e.g.*, $1.1 m_0$, compared to $0.2 m_0$ for electrons in GaN-based materials) and corresponding low mobility, so that it is difficult for hole transport into the lower QWs far away from $p\text{-In}_x\text{Ga}_{1-x}\text{N:Mg}$ layer.

However, Figure 3.9(b) shows that for the LED B the emission from QW1 becomes stronger at the expense of that from QW2 and QW3. The peak intensity of QW1 becomes comparable to that of QW3 around $I \sim 80$ mA. This result suggests that in the case of the LED B more holes injected into the active region were transported to QW1 from QW2 and QW3 compared to the LED A. The enhanced hole transport is more clearly shown in the LED C having the highest In mole fraction in the $p\text{-In}_x\text{Ga}_{1-x}\text{N:Mg}$ layer. As shown in Figure 3.9(c), the EL intensity of QW1 is higher than those of QW2 and QW3 even at relatively low injection currents as well as at high driving currents up to $I \sim 80$ mA. Moreover, the QW1 in LED C shows the highest EL intensity among the three TW-LEDs over the entire injection current range. This gradual increase in EL intensity of

QW1 from LED A to LED C and stronger emission of QW1 compared to QW2 and QW3 in LED C indicate that more holes can be transported to the lower QW as drive current increases. Since the MQW epitaxial layer design and growth conditions for the LEDs A, B, and C are designed to be same and the PL spectra shown in Figure 3.8(b) were identical for those TW-LEDs, it is reasonable to infer that the changes of emission spectra from the LED A to the LED C originate from dynamics of carriers that are injected bipolarly, more specifically, from the improved hole transport by varying the In mole fraction of $p\text{-In}_x\text{Ga}_{1-x}\text{N:Mg}$ layer. To further analyze the distribution of holes in the MQW active region according to the $p\text{-In}_x\text{Ga}_{1-x}\text{N:Mg}$ layers, the ratio of normalized integrated EL emission intensity of each QW in the LED A, B, and C at $I \sim 80$ mA is shown in Figure 3.10.

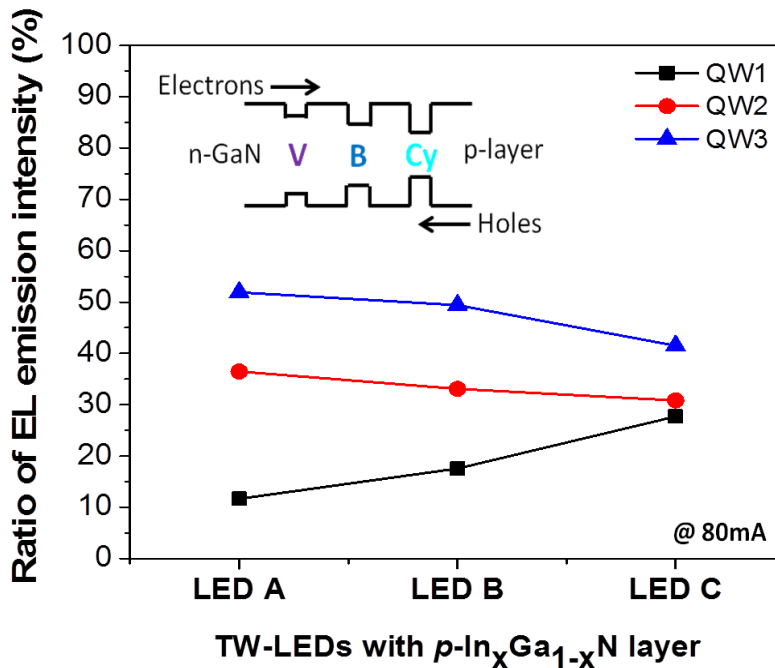


Figure 3.10: Normalized EL emission intensity of each QW in the LED A, B, and C with $p\text{-In}_{0.015}\text{Ga}_{0.985}\text{N}$, $p\text{-In}_{0.025}\text{Ga}_{0.975}\text{N}$, and $p\text{-In}_{0.035}\text{Ga}_{0.965}\text{N}$ layers, respectively, at an injection current of 80 mA.

The ratio of emission intensity of QW1 is enhanced, while those of QW2 and QW3 are decreased as the In content of *p*-type layer is increased from LED A to LED C. In addition, the portion of emission intensity from each QW is more uniformly distributed in the case of LED C. This result indicates that increase in the In content of the *p*-In_xGa_{1-x}N:Mg layer promotes the hole transport across MQWs, so that more holes are able to be arrived to the QW1 far away from *p*-type layer and uniformly distributed throughout the MQW active region.

3.5 Effect of Si Doping in a Selected Quantum-well Barrier

For further confirmation of the hole transport effect on EL spectra of TW-LEDs, silicon (Si) doping in a selected QWB is employed, as schematically shown in the inset of Figure 3.11, since the intentional Si doping in a QWB is an effective way to impede hole transport by increasing a potential barrier for the valance band of an electronic band structure [87, 88]. The EL spectra of TW-LEDs with *p*-In_{0.025}Ga_{0.975}N layers (similar to the LED B used in Chapter 3.4) with various Si doping in a selected QWB at an injection current of *I*=80 mA are shown in the Figure 3.11. The Si doping concentration in a selected QWB was $n \sim 5 \times 10^{18} \text{ cm}^{-3}$.

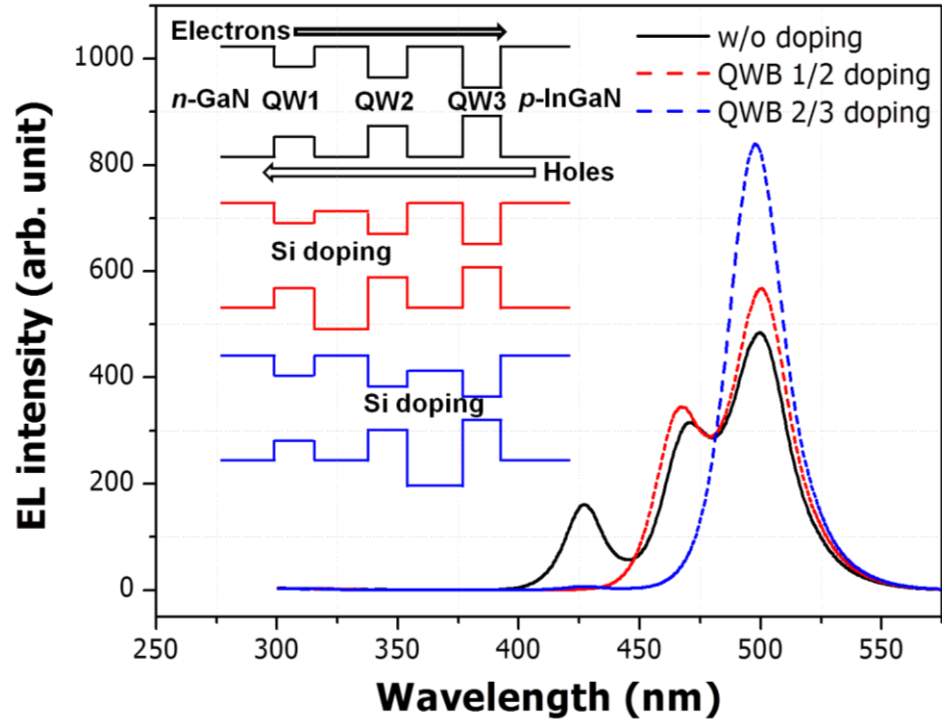


Figure 3.11: EL spectra of LEDs at $I=80$ mA, employing a $p\text{-In}_{0.025}\text{Ga}_{0.975}\text{N}$ layer with Si doping in a selected QW barrier (QWB) of TW-LEDs consisting of $n/V(\text{QW1})\text{B}(\text{QW2})\text{Cy}(\text{QW3})/p$. The location of Si doping in a selected QWB is shown in the inset.

When the QWB between QW1 and QW2 (QWB1/2) is doped with Si, the emission from QW1 (V) disappears and the emission from QW2 (B) and QW3 (Cy) slightly increases due to limited hole transport into QW1. In the case of the TW-LED with Si doping in QWB2/3, only one strong emission from QW3 is observed. This result further confirms that the gradually increased EL intensity of QW1 from LED A to LED C, described by the EL intensity changes shown in Figure 3.9 and 3.10, is caused by improved hole transport in the MQW active region.

3.6 Discussion on the Possible Mechanism of Improved Hole Transport

The improvement in hole transport across the MQW active region may be due to (1) strain effects in the p -type region by $\text{In}_x\text{Ga}_{1-x}\text{N}$, or (2) modified energy for holes to be transported by a potential barrier between the p - $\text{In}_x\text{Ga}_{1-x}\text{N}$ and the GaN of last QWB. For the effects of strain by p - $\text{In}_x\text{Ga}_{1-x}\text{N}$ layer, the strain on top of MQW may (i) change mobility of holes and (ii) modify strain status in the MQW. Modified strain in the active region results in mitigation on quantum-confined Stark effect and hence, enhancement of oscillator strength for radiative recombination [86, 89]. First, the biaxial strain in the c -plane of wurtzite structures does not significantly change mass of heavy holes and the density of states at the valence band maxima [90]. In addition, PL results in this study showed the same peak position and intensities, as described earlier, suggesting that strain effects by different p - $\text{In}_x\text{Ga}_{1-x}\text{N}$ on the MQW should not be significant. Therefore, compressive in-plane strain in p - $\text{In}_x\text{Ga}_{1-x}\text{N}$ with $x_{\text{In}} \leq 3.5\%$ used in this work on the transport of holes in the MQW active region is believed to be negligible.

In this study, the difference between hole injection efficiency and effective hole transport among the QWs needs to be distinguished. Hole injection efficiency is related to total number of holes injected in the MQW active region and hole transport is more related to distribution of holes among the QWs of given total number of holes injected with concentrations set by hole injection efficiency. Enhanced hole transport into farther (away from p -type layers) QWs is believed to be related to potential barriers formed between a p -type layer and MQW active region in electronic band structures. The heterostructure interface at p - $\text{InGaN}/\text{GaN:ud}$ has a potential barrier depending on x_{In} in p - $\text{In}_x\text{Ga}_{1-x}\text{N}$ layer, which may provide a reservoir for holes before being injected into the

active region. LEDs with $p\text{-In}_x\text{Ga}_{1-x}\text{N}$ may have a lower hole injection efficiency due to a potential barrier between $p\text{-InGaN}$ and last GaN:ud QWB. However, once they are injected into the active region overcoming the potential barrier, the transport in the active region among the QWs is more pertinent to a kinetic energy of holes. This higher energy of holes will result in changes in carrier capturing efficiency of each different-wavelength QW. The ratios of EL integrated intensity of each QW and of total intensity in the TW-LEDs with $p\text{-In}_x\text{Ga}_{1-x}\text{N}$ layer with increasing injection current are shown in the Figure 3.12.

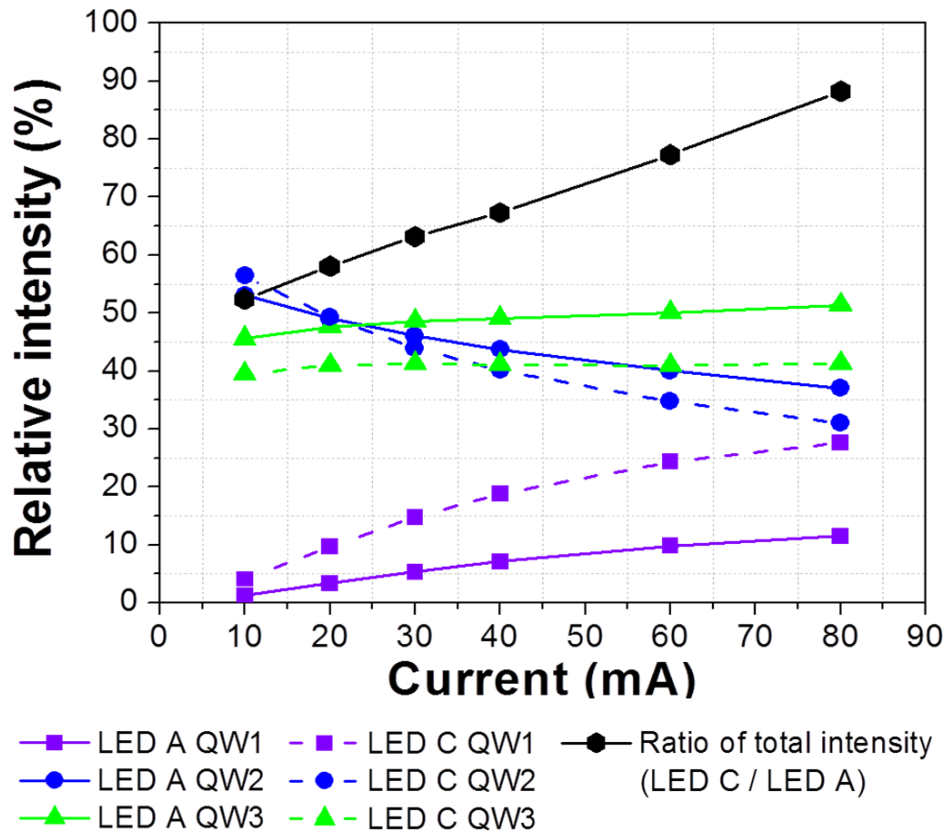


Figure 3.12: Ratios of EL integrated intensity from each QW of TW-LEDs A and C consisting of $n/V(\text{QW1})B(\text{QW2})C_y(\text{QW3})/p$ and ratios of total EL intensity of the LED C to that of the LED A with increasing current.

The hole injection efficiency of LEDs with higher potential barriers for holes (p -InGaN with higher x_{In}) appears to be lower, especially at low currents. For example, the ratio of total EL intensity of the LED C to that of the LED A (LED C/LED A) is about half (~53 %) at $I=10$ mA. At relatively high currents, however, hole injection efficiency of the LED C is suggested to be improved with a value of close to 90 % at $I=80$ mA. At the same time, the uniformity of emission in each QW is also improved for the LED C with higher potential barriers for holes to be injected. The ratio of emission intensity of QW1 (V) is enhanced, while that of QW2 (B) decreases with increasing x_{In} in the p -In $_x$ Ga $_{1-x}$ N layer. As a result, the portion of emission intensity from each QW, dotted line in Figure 3.12, is more uniformly distributed in the case of the LED C. Therefore, the role of potential barrier by p -In $_x$ Ga $_{1-x}$ N limits a hole injection efficiency especially under low injection conditions. The injection efficiency effects, however, are diminished with increasing current and are expected to become negligible under high injection conditions. With similar injection efficiencies of holes, injected holes overcoming higher potential barrier gain energy to be transported farther, resulting in more uniform hole distributions among QWs in order to mitigate the effects of efficiency droop.

3.7 Summary

In this chapter, the hole injection and transport in MQW active regions was experimentally studied by using a multiple-wavelength-emitting active region in the LED structures by changing the p -type hole injection layer from the standard GaN layer to In $_x$ Ga $_{1-x}$ N layers. The special design of dual- and triple-wavelength-emitting MQW active region allows us to trace the hole distribution across the active region. It was found that

the holes are preferentially injected into the QW adjacent to the p -type layer with lower In-mole-fraction p - $\text{In}_x\text{Ga}_{1-x}\text{N:Mg}$ layer. Enhanced hole transport with increasing In mole fraction in the p - $\text{In}_x\text{Ga}_{1-x}\text{N:Mg}$ layer has been shown by analyzing the EL spectra. The improved hole transport and corresponding uniform distribution was achieved possibly by potential barrier near p -type layer and MQW active region. This is because the holes injected into the MQW active region achieve kinetic energy depending on the potential barrier, resulting in a hole transport favorable environment in the MQW active region. At the same time, the limited hole injection due to the potential barrier for hole can be overcome under high injection conditions.

CHAPTER 4

GALLIUM AUTO-INCORPORATION IN AN InAl(Ga)N LAYER

4.1 Introduction

Recently developed InAlN ternary wide-bandgap semiconductor materials open a way to new III-nitride (III-N)-based heterostructures due to their large refractive index contrast and wider bandgap energy with respect to GaN. In addition, the InAlN ternary and InAlGaN quaternary alloys have the possibility to grow epitaxial layers that are lattice-matched and strain-/polarization-engineered on binary GaN and AlN, and on ternary AlGaN and InGaN layers [39, 40], as shown in Figure 4.1.

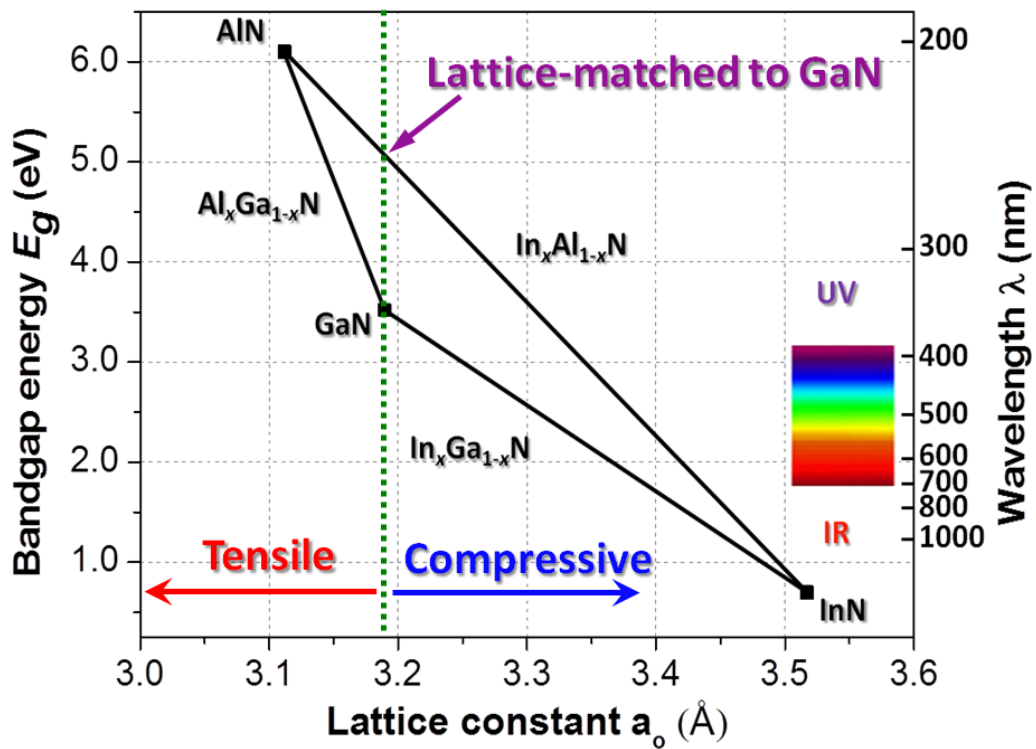


Figure 4.1: Bandgap energy vs. lattice constant and strain status of III-nitride compound semiconductors.

These advantages enable the InAlN alloys to be used in photonic devices, such as GaN/InAlN superlattices for near-infrared intersubband transitions [42], high-reflectivity short-wavelength distributed Bragg reflectors in vertical-cavity surface-emitting lasers [43], cladding and waveguide layer structures in edge-emitting lasers [45], and electron-blocking layers in visible light-emitting diodes [46]. For electronic device applications, an $\text{In}_{0.18}\text{Al}_{0.82}\text{N}/\text{GaN}$ heterostructure, exhibiting a high sheet carrier density in the channel region of two-dimensional electron gas, makes the structure suitable for high-electron mobility transistors [49]. Also, polarization-engineered $\text{In}_x\text{Al}_{1-x}\text{N}$ layers have been used as a Schottky barrier to demonstrate enhancement-mode (normally-off) heterostructure field-effect transistors [50].

While growth and characterization of $\text{In}_x\text{Al}_{1-x}\text{N}$ materials with various growth parameters have been studied for such applications [56,57,59], since high-quality and accurately-controlled InAlN epitaxial material growth has been challenging, fundamental understanding on the InAlN materials and epitaxial growth processes is still lacking. In addition, majority of previous studies focused on the growth, characterizations, and device applications of epitaxial InAlN layers assumed that these materials are *ternary* InAlN. Since only In, aluminum (Al), and nitrogen (N) precursors were introduced for the growth of the layer, the assumption did not seem to be unreasonable; however, the assumption could make the characterization of materials and devices containing InAl(Ga)N layers prone to erroneous analysis and conclusion by ignoring possible uncontrolled Ga content in the layer. The possible unintentional incorporation of gallium (Ga) has been recently reported during the epitaxial growth of the InAlN layers by both metalorganic chemical vapor deposition (MOCVD) and molecular beam epitaxy (MBE)

[62,63]. However, the origins of Ga incorporation in InAlN layers, resulting in InAl(Ga)N quaternary layers, and its auto-incorporation mechanism have not been identified. In the present study, it is compared that the InAl(Ga)N epitaxial layers that were *intended* to be InAlN layers grown on different underlayers (GaN and AlN), regrown layers that are same as templates (GaN, AlN, and no regrowth), and coating/deposition status on a wafer susceptor/carrier (GaN, AlN, and no deposition) and on other surrounding surfaces in a growth chamber, to systematically study on all the possible origins of Ga auto-incorporation during the epitaxial growth of ternary InAlN and quaternary InAlGaN. Also, the effect of Mg or Mg precursor on Ga auto-incorporation is studied as a part of growth chamber condition modification. The possible origins and a mechanism are discussed based on experimental results and a proposed model for Ga auto-incorporation.

4.2 Growth of the InAl(Ga)N Layer by MOCVD

$\text{In}_x\text{Al}_{1-x}\text{N}$ layers were grown by MOCVD in a reactor system equipped with a close-coupled showerhead (CCS) chamber. Trimethylaluminum (TMAI, $\text{Al}(\text{CH}_3)_3$), trimethylindium (TMIn, $\text{In}(\text{CH}_3)_3$), and ammonia (NH_3) were used as precursors with a nitrogen (N_2) carrier gas for the growth of the InAlN layers. Trimethylgallium (TMGa, $\text{Ga}(\text{CH}_3)_3$) was used only for the growth of a GaN regrown layer on a GaN template. Bis-cyclopentadienyl magnesium (Cp_2Mg , $\text{Mg}(\text{C}_5\text{H}_5)_2$) was also used to further study the effect of chamber conditions. Slower growth rate (low molar flow rates of Group III precursors with TMAI = 5.834 $\mu\text{mol}/\text{min}$. and TMIn = 11.691 $\mu\text{mol}/\text{min}$. and Group V precursor with NH_3 = 0.134 mol/min.) and higher pressure (~300 Torr) and temperature

(~890 °C) than those of typical $\text{In}_{0.18}\text{Al}_{0.82}\text{N}$ layers were intentionally selected to distinguish the effects from various origins. Thus, higher Ga mole fractions are expected in this study than those in typical $\text{In}_{0.18}\text{Al}_{0.82}\text{N}$ layers due to higher desorption rate of In on a growing surface and higher homogeneous gas-phase reaction rate between TMAI and NH_3 .

For the investigation on the effect of underlayers, an AlN and a GaN template, which consists of an AlN layer and a GaN layer grown on a (0001) *c*-plane sapphire substrate, respectively, was employed for the growth of InAl(Ga)N epitaxial layers. The InAl(Ga)N layers on GaN templates were grown with and without a GaN regrown layer between the InAlN and the template for the purpose of studying the variations of “pre-deposition” conditions on a substrate, a wafer susceptor/carrier, and surrounding surfaces in the growth chamber. The regrown GaN layers were either unintentionally doped (GaN:ud) or Mg-doped (GaN:Mg) for further study on the effect of Mg or Mg precursor on the Ga auto-incorporation. A detailed description for the layer structures and selected growth parameters of the samples is summarized in Table 4.1.

Table 4.1: Layer structures and growth parameters of the samples grown in this study.

Sample	In _x Al _{1-x} N layer		Underlayers	
	Layer:doping	D/III ^{a)}	Regrowth layer	Template
A	In _x Al _{1-x} N:ud		None	AlN/sapphire
B	In _x Al _{1-x} N:ud		None	GaN/sapphire
C	In _x Al _{1-x} N:ud		GaN:ud	GaN/sapphire
D	In _x Al _{1-x} N:Mg	2.21 %	GaN:ud	GaN/sapphire
E	In _x Al _{1-x} N:Mg	4.42 %	GaN:ud	GaN/sapphire
F	In _x Al _{1-x} N:Mg	8.84 %	GaN:ud	GaN/sapphire
E' ^{b)}	In _x Al _{1-x} N:Mg	4.42 %	GaN:ud	GaN/sapphire
G ^{b)}	In _x Al _{1-x} N:ud		GaN:Mg	GaN/sapphire

^{a)} D/III is a ratio of the molar flow rate of dopant precursor (Cp₂Mg) to the sum of molar flow rates of Group III precursors (TMIn+TMAI): $D/III = Cp_2Mg/(TMIn+TMAI)$.

^{b)} Samples E' and G have a GaN cap layer on InAl(Ga)N for secondary-ion mass spectrometry measurement.

For these runs, GaN coating and baking prior to the growth run was performed. However, the effect from prior GaN coating may be overshadowed by the effect from the GaN regrowth in the same run. When it comes to the cleaning, two techniques for the cleaning of wafer susceptor/carrier were employed. In the case of GaN deposited wafer susceptor/carrier, the cleaning was performed by baking of the wafer susceptor/carrier in the growth chamber with H₂ ambient at around 1100 °C. However, in the case of Al-containing-material-deposited wafer susceptor/carrier, aforementioned technique does not

result in complete cleaning. Instead, the chemical etching during the baking in the mixture of HCl and H₂ gases at around 850 °C in a separate cleaning chamber which is designed as a separate susceptor etching system especially for Al-containing-material-deposited wafer susceptor/carriers. The cleaning of wafer susceptor/carrier and baking of the growth chamber were performed for every run unless there is any intentional purpose.

The epitaxial layers were characterized by high-resolution X-ray diffraction (HR-XRD) ω - 2θ scan and reciprocal space mapping (RSM), Rutherford backscattering spectrometry (RBS) (with the collimated He⁺⁺ ion beam energy of 2.0 MeV), in conjunction with XRUMP simulation, and secondary-ion mass spectrometry (SIMS). In case of the HR-XRD measurement, asymmetric RSM (105) was also performed to make the symmetric ω - 2θ scan valid for the composition estimation.

4.3 Effects of the Underlying and Regrown Layers

The HR-XRD ω - 2θ scans near the (00•2) diffraction condition of InAl(Ga)N layers grown on different underlayers for samples A, B, and C and the schematic illustration of epitaxial layer structures of the measured samples are shown in Figure 4.2(a) and (b).

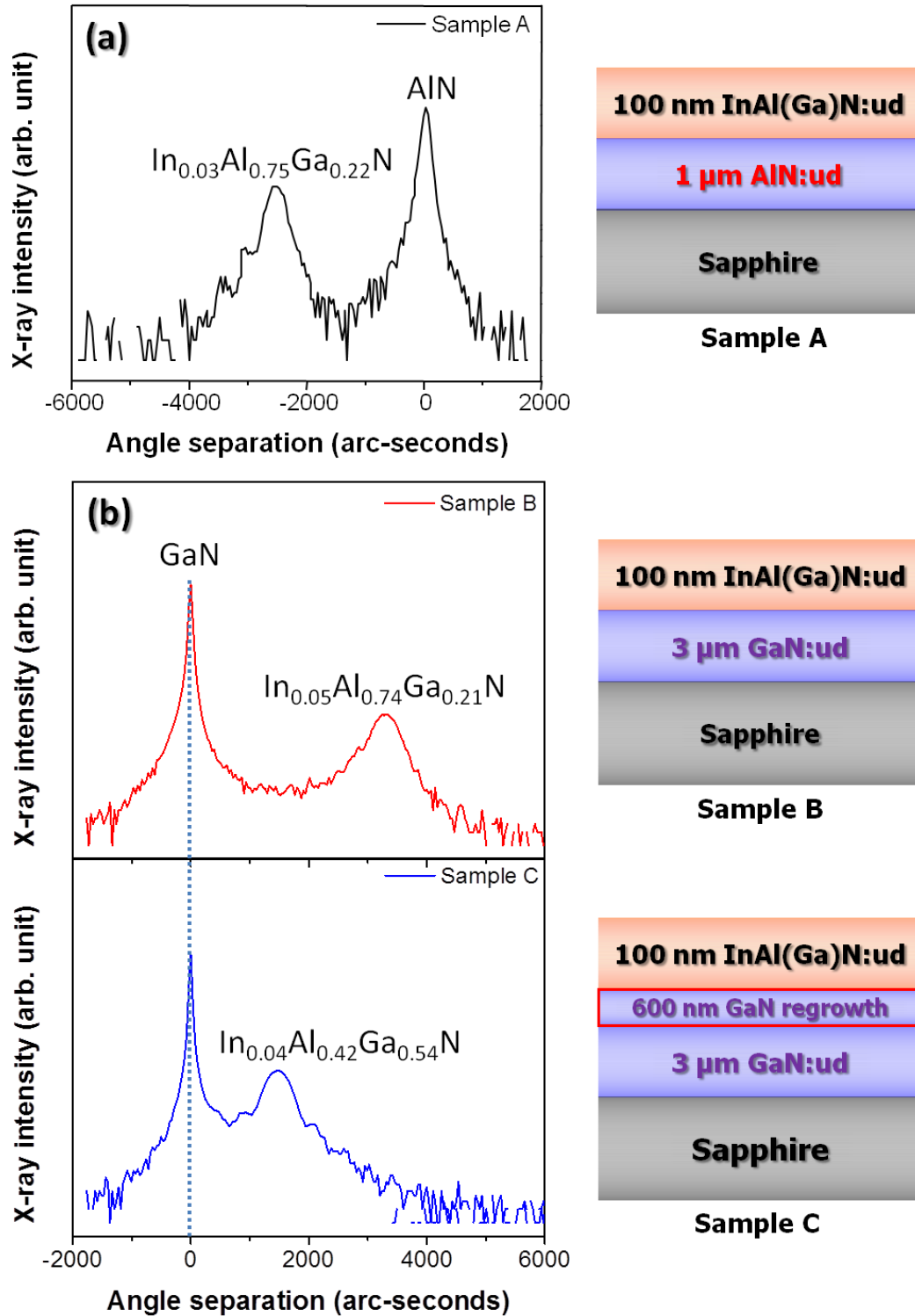


Figure 4.2: High-resolution X-ray diffraction (HR-XRD) ω - 2θ scans near the (00•2) diffraction condition of templates for (a) an InAl(Ga)N layer grown on an AlN template (sample A) and (b) InAl(Ga)N layers grown on GaN templates without and with a GaN regrown layer (sample B and C, respectively).

The InAl(Ga)N layers of samples A and B were grown on AlN and GaN templates without a regrown layer, while a GaN:ud regrown layer was used on a GaN template before the growth of InAl(Ga)N for sample C. This GaN:ud regrowth process on a GaN template also resulted in Ga-containing deposition on an initially uncoated wafer susceptor/carrier. Even with the same growth parameters for InAlN layers of samples A, B, and C, the peaks of InAl(Ga)N layers are located at different positions, which may suggest differences in alloy compositions and/or strain status. The alloy composition of quaternary alloy III-V semiconductors cannot be uniquely determined by XRD. RBS measurements were performed to determine mole fractions of In, Al, and Ga in Group-III elements. The quaternary layers of samples A and B have compositions of $\text{In}_{0.03}\text{Al}_{0.75}\text{Ga}_{0.22}\text{N}$ and $\text{In}_{0.05}\text{Al}_{0.74}\text{Ga}_{0.21}\text{N}$, respectively. These compositions match reasonably well for the locations of XRD peaks based on XRD dynamical simulations of quaternary alloys on different templates, suggesting that difference in InAl(Ga)N peak positions between sample A and B is mainly due to different strain status. Slight differences in mole fractions, especially for In, could be related to difference in strain for InAl(Ga)N layers grown on AlN and GaN templates [91], experimental/fitting errors in RBS measurement and XRUMP simulation [92], and different actual temperatures of growing surfaces by different thermal conductivities between GaN and AlN [93] or by different curvatures of GaN and AlN templates [94]. Two major features have to be pointed out for the effects of underlying and regrown layers. First, the mole fraction of Ga is substantial for all the samples A, B, and C. Such substantial amount of Ga in InAl(Ga)N by auto-incorporation could originate from (1) Ga contamination from the GaN underlayer by interdiffusion, (2) Ga-containing deposition on a wafer

susceptor/carrier, and/or (3) Ga-containing deposition on other surrounding surfaces in the growth chamber, such as the surfaces of liner, the showerhead/precursor-injector-plenum, and the walls which are made of (3.1) quartz liner or (3.2) stainless steel, as schematically shown in Figure 4.3. In the case of the origin #3, quartz liner and stainless steel parts are the same surrounding surfaces in the growth chamber but those have different temperatures. Based on our proposed model, temperature of the surrounding surfaces will be critical in terms of equilibrium vapor pressure of liquid metallic Ga, so that the origin #3 is divided into #3.1 and #3.2.

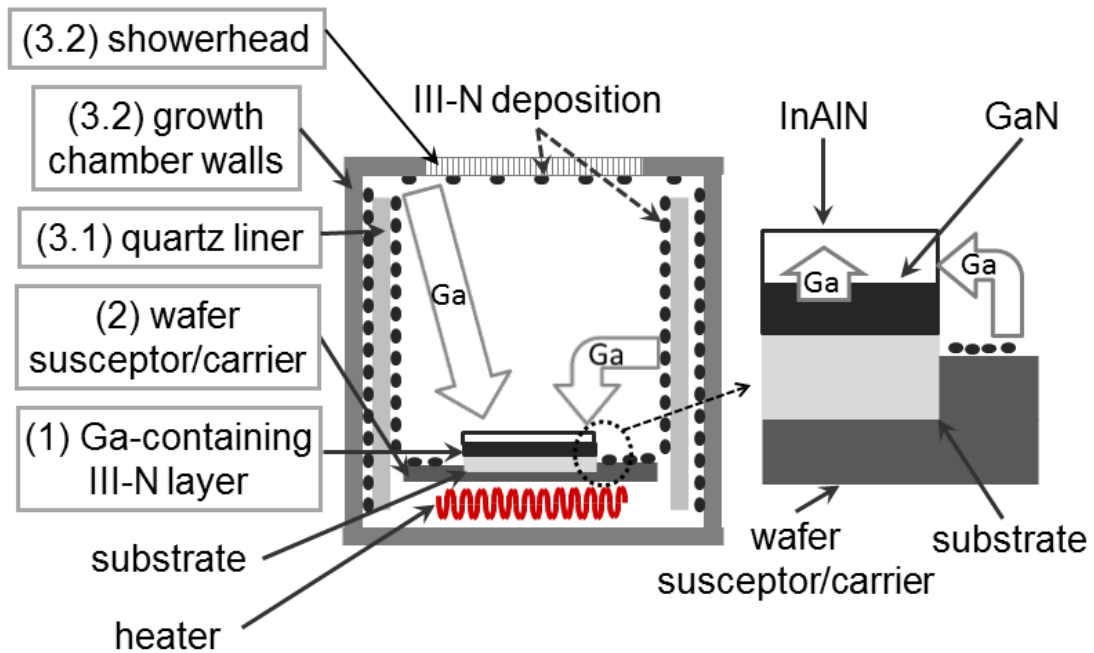


Figure 4.3: Schematic view showing possible sites leading to Ga auto-incorporation in a growth chamber with close-coupled showerhead. The possible sites consist of (1) a Ga-containing III-N epitaxial underlayer, (2) a wafer susceptor/carrier, (3.1) quartz liner, and (3.2) stainless-steel showerhead and chamber walls.

For the comparison between samples A and B, since the wafer susceptor/carrier was initially uncoated, the effect from GaN deposition on the wafer susceptor/carrier (origin #2) can be excluded. In addition, the mole fraction of Ga in sample B is comparable to that in sample A so that the interdiffusion (origin #1) of Ga from the underlying GaN layer [95] is not believed to be a dominant mechanism of the Ga auto-incorporation. Therefore, substantial amount of Ga (21~22 % in Group III) in InAl(Ga)N layer may come from Ga-containing deposition on the surrounding surfaces (origin #3). When this is the case, Ga incorporation in InAlN materials is inevitable, as virtually all the III-N MOCVD growth chambers contain a certain amount of deposition containing Ga except for the run #1 of new growth chamber. Secondly, a regrown GaN layer alters the mole fraction of Ga significantly. Different XRD peak positions for the InAl(Ga)N layers of samples B and C suggest a significant difference in alloy composition, since their epitaxial structures and strain status are essentially similar except for the GaN regrown layer (~800 nm) of samples C, which changes the coating status on a wafer susceptor/carrier from “uncoated” to “GaN-coated” during the regrowth. The compositions of the quaternary layers of samples B and C are estimated to be $\text{In}_{0.05}\text{Al}_{0.74}\text{Ga}_{0.21}\text{N}$ and $\text{In}_{0.04}\text{Al}_{0.54}\text{Ga}_{0.42}\text{N}$, respectively. During the GaN regrowth, GaN coating on the wafer susceptor/carrier (origin #2) and additional coating of Ga-containing deposition on the surrounding surfaces in the growth chamber (origin #3) may further contribute to the Ga auto-incorporation in the InAl(Ga)N layers, as sample C is compared to samples A and B.

4.4 Effects of the Growth Chamber Coating Conditions

To further understand the Ga auto-incorporation process, Mg doping was employed in the InAl(Ga)N epitaxial layer. It should be noted that the introduction of Cp_2Mg was intended for the modification of chamber conditions. The XRD measurement results of the symmetric (002) ω -2 θ scan for InAl(Ga)N:Mg layers with increasing Cp_2Mg molar flow rates grown on a GaN:ud regrowth layer and template for samples C, D, E, and F are shown in Figure 4.4. An XRD peak of a InAl(Ga)N:Mg layer shifts toward a GaN peak as the Cp_2Mg molar flow rate increases, indicating that the compositional changes in the InAl(Ga)N:Mg layers when the InAl(Ga)N:Mg layers of all the samples are fully strained.

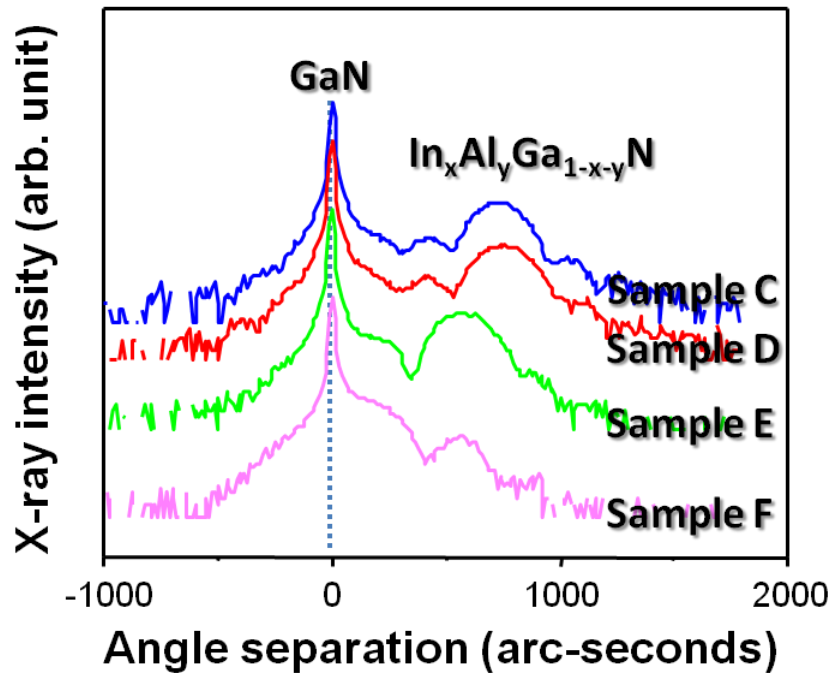


Figure 4.4: HR-XRD ω -2 θ scans near the (00•2) diffraction condition of wurtzite GaN of InAl(Ga)N layers grown under various Cp_2Mg molar flow rates; corresponding to sample C, D, E, and F.

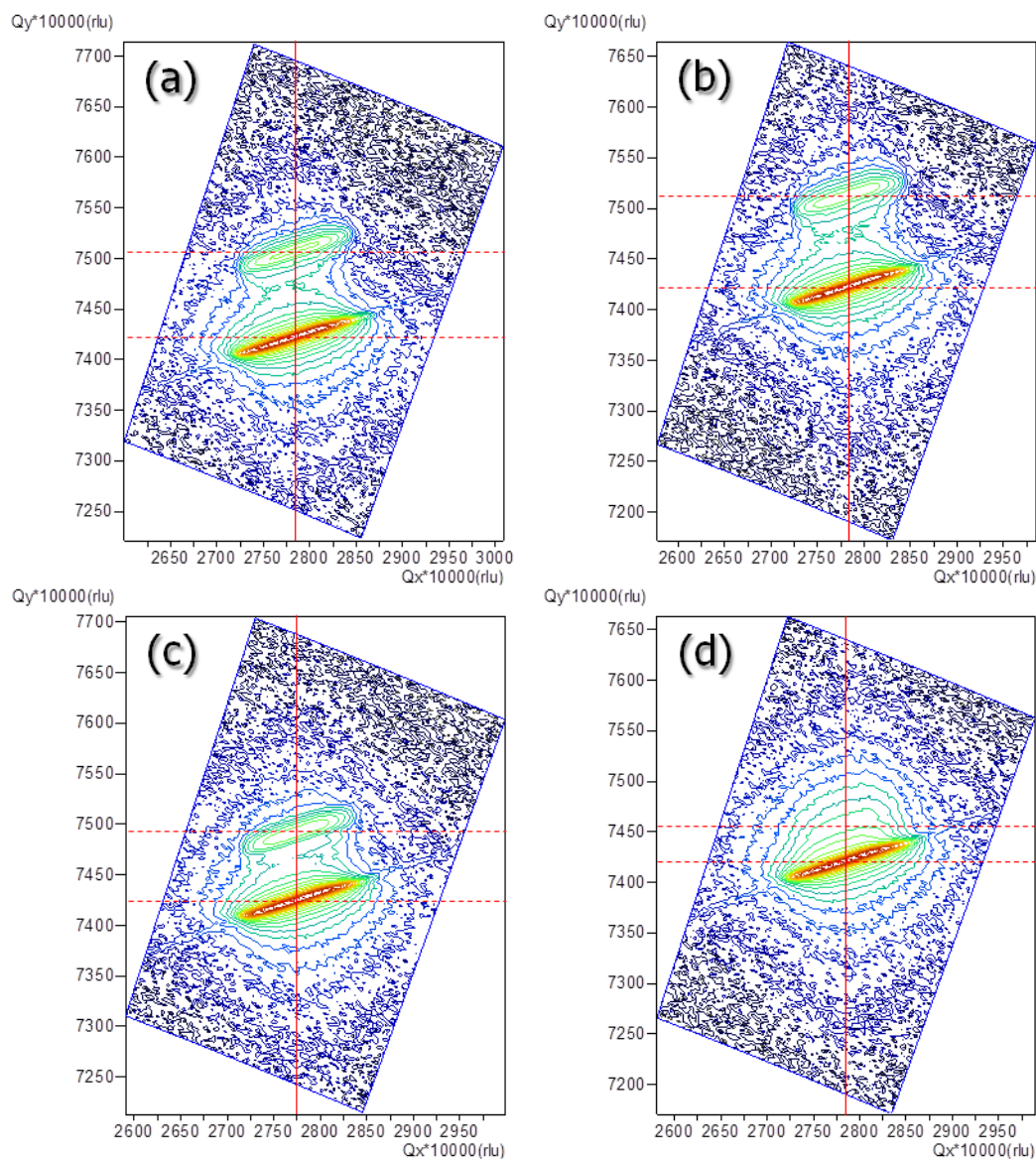


Figure 4.5: Asymmetric RSM using (10•5) diffraction condition of wurtzite GaN for the InAl(Ga)N layers of (a) sample C, (b) sample D, (c) sample E, and (d) sample F grown under various Cp_2Mg molar flow rates.

To investigate the strain status in the InAl(Ga)N layers of sample C-F, the asymmetric RSM map around the GaN (10•5) reciprocal lattice point was performed, as shown in Figure 4.5. The diffractions from the InAl(Ga)N layer and GaN layer have the same Q_x in the reciprocal space for all sample C-F, indicating that the InAl(Ga)N layers

are fully strained. Thus, the changes of the transverse position of the InAl(Ga)N layer toward GaN layer from sample C to sample F demonstrate the mole fraction changes in the InAl(Ga)N layer, which was explained by the peak shift in ω - 2θ scan shown in Figure 4.4. The RSM may be critical for the estimation of composition of InAl(Ga)N, especially the epitaxial films are partially relaxed. However, most InAl(Ga)N layers are fully-strained, which makes symmetric (002) ω - 2θ valid for composition estimation, not having to resort to RSM.

The variation in mole fraction of each Group-III element measured by RBS in the InAl(Ga)N:Mg layer with different D/III is shown in Figure 4.6.

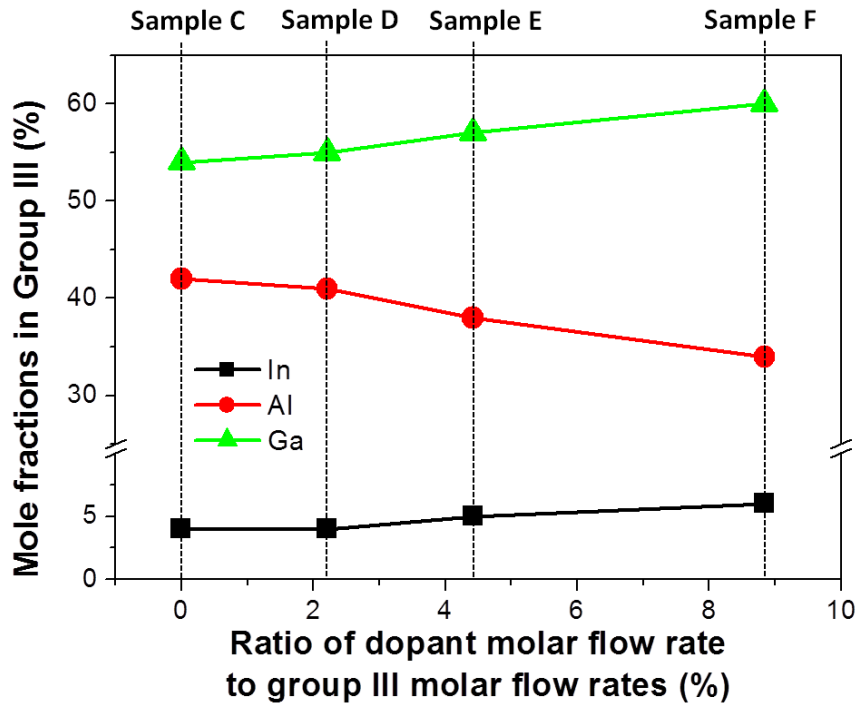


Figure 4.6: The variations in mole fraction of each Group-III element obtained by RBS in the InAl(Ga)N layers with different D/III ratios; corresponding to sample C, D, E, and F.

The D/III is a ratio of molar flow rate of dopant precursor (Cp_2Mg) to those of Group-III precursors ($\text{TMIIn}+\text{TMAI}$); $\text{D/III} = \text{Cp}_2\text{Mg}/(\text{TMIIn}+\text{TMAI})$. As D/III increases, the mole fraction of Ga increases from 54 % to 60 %, while that of Al decreases from 42 % to 34 %. Introduction of Mg precursor appears to promote the auto-incorporation of Ga in $\text{InAl}(\text{Ga})\text{N}$ layers. Decrease in Al is believed to be due to *relative* decrease in mole fraction with respect to Ga, as more Ga is incorporated in the layer. Increase in In may be related to reduced desorption rate of In on the growing surface by higher growth rate of the $\text{InAl}(\text{Ga})\text{N}:\text{Mg}$ layers with increasing incorporation of Ga.

To further investigate the effect of Mg precursor on chamber surface and wafer susceptor/carrier coating, the Mg precursor was introduced before the growth of $\text{InAl}(\text{Ga})\text{N}$ during the regrowth of GaN for “pretreatment” of the Mg precursor, that is, a GaN:Mg regrowth layer was employed instead of GaN:ud regrowth layer, while the InAlN layer remained to be unintentionally doped. The Cp_2Mg tends to be preferably adsorbed on surfaces of surroundings in the growth chamber until a certain saturation point is reached, known as the memory effect [96]. This memory effect results in slow turn-on (ramping-up transient) and delayed turn-off (tailing) in Mg distribution profile in epitaxial structures. If Cp_2Mg or Mg atoms promote the auto-incorporation of Ga, the profile of Ga in the $\text{InAl}(\text{Ga})\text{N}$ layer may be in line with the profile of Mg.

The distribution profiles of Group-III elements and Mg measured by SIMS, as a function of depth from the sample surface, for $\text{InAl}(\text{Ga})\text{N}:\text{Mg}$ on GaN:ud (sample E') and $\text{InAl}(\text{Ga})\text{N}:\text{ud}$ on GaN:Mg (sample G) are shown in Figure 4.7(a) and (b).

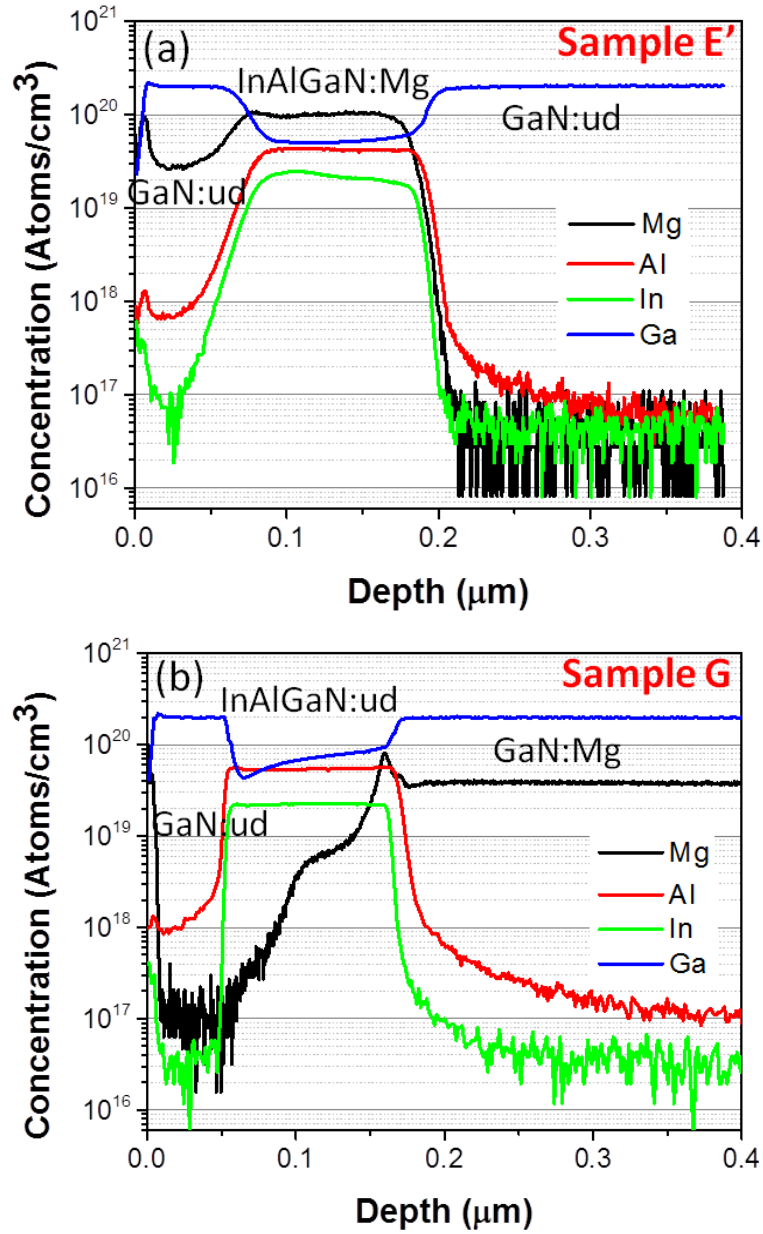


Figure 4.7: SIMS distribution profiles of Group III elements and Mg for (a) an InAl(Ga)N:Mg layer grown on a GaN:ud layer (sample E') and (b) an InAl(Ga)N:ud layer grown on a GaN:Mg layer (sample G).

Both sample E' and G have a GaN:ud cap layer to isolate surface effect from profiles in InAl(Ga)N layers during the SIMS measurement. Even though the concentration of the elements calibrated only for dopant for SIMS measurement,

comparison of relative amount of Group-III elements is still valid. The amount of Ga in the InAl(Ga)N:Mg layer is constant for sample E', as shown in Fig. 4.5(a). However, for sample G, the amount of Ga in an InAl(Ga)N:ud layer (with a GaN:Mg layer underneath) decreases, as the growth of the InAl(Ga)N:ud layer proceeds, while amount of Al and In remains constant. Decreasing transient of Ga in the InAl(Ga)N:ud layer shows the similar behavior to that of Mg tailing after the Mg precursor being turned off. Mg precursor, which was adsorbed onto reactor environment during the GaN:Mg growth, is released into gas phase during the InAl(Ga)N:ud growth and this process is believed to be related to enhanced auto-incorporation of Ga. Such different SIMS profiles between sample E' and G support an experimental evidence that the auto-incorporation of Ga in InAl(Ga)N:Mg layers was affected by Cp₂Mg or Mg during the growth, as shown in Figure 4.7(a) and (b). From these results, it is confirmed that the existence of Mg or Cp₂Mg in the reactor during InAl(Ga)N layer growth promotes the auto-incorporation of Ga. The exact mechanism of this enhanced auto-incorporation requires further studies. Even though exact pathway for the chemical reactions is not known, it may be related to eutectic formation between metallic Ga and intermetallic compound Mg₂Ga₅ having a very low eutectic temperature of ~302 K [97].

4.5 Discussion on the Gallium Auto-incorporation

4.5.1 Comparison of Gallium Mole Fractions in the InAl(Ga)N Layers

The Ga mole fractions in InAl(Ga)N layers grown using the same growth parameters, but varying the underlayers, regrowth layers, and the growth chamber surface conditions are shown in Table 4.2.

Table 4.2: Mole fractions of GaN in InAl(Ga)N layers grown using same growth parameters, but using different chamber conditions, underlayers, and wafer susceptor/carrier conditions.

Case	Previous growth run	Template	Regrowth layer ^{a)}	InAl(Ga)N layer	GaN mole fraction
I	GaN-free	AlN/sapphire	AlN	InAl(Ga)N:ud	~0.18–0.20 ²³
II	GaN-free	AlN sapphire	None	InAl(Ga)N:ud	~0.22
III	GaN coating	AlN/sapphire	AlN	InAl(Ga)N:ud	~0.30 ²³
IV	GaN-free	GaN/sapphire	None	InAl(Ga)N:ud	~0.21
V	GaN-free	GaN/sapphire	GaN:ud	InAl(Ga)N:ud	~0.54
VI	GaN coating	GaN/sapphire	GaN:ud	InAl(Ga)N:Mg	~0.60

^{a)} A regrowth layer was grown between a template and an InAl(Ga)N layer.

To understand the effect of an underlayer without GaN regrowth, we compare Case I, II, and IV. It should be noted that in these cases, no prior GaN coating or growth occurred. The Ga mole fractions for these three cases are quite similar, falling in the range of ~0.20–0.22, regardless of underlayers. Therefore, interdiffusion of Ga from the GaN underlayer (origin #1) does not significantly affect the Ga auto-incorporation. These results also indicate that Ga auto-incorporation is independent on whether the film contains an AlN regrowth layer or not. Comparing Cases III and V, the regrowth process of GaN results in higher Ga mole fraction (~0.54) than the coating of GaN in the previous growth run (~0.30). The regrowth of GaN accompanies coating of Ga-containing deposition both on the surrounding surfaces in a growth chamber (origin #3) and on the

wafer susceptor/carrier (origin #2). The coating of GaN in the previous growth run without regrowth of GaN leaves Ga-containing deposition in a growth chamber, while wafer susceptor/carrier is still GaN-free. Therefore, high Ga mole fraction for the case of V is reasonable. Comparing Cases V and VI, Mg or Cp₂Mg in the reactor during InAl(Ga)N layer growth promotes the auto-incorporation of Ga in addition to the effect from a previous GaN coating run by modifying deposition conditions of GaN on surrounding surfaces and a wafer susceptor/carrier.

Analyzing experimental data of various cases, the origins of Ga for the auto-incorporation in the InAl(Ga)N layers are believed to Ga-containing deposition on a wafer susceptor/carrier (origin #2) and surrounding surfaces in the growth chamber (origin #3). This auto-incorporation in the InAl(Ga)N layers are believed to occur by enhanced desorption of metallic Ga from the deposition, when In is present. The effect of Ga-containing deposition is believed to be related to enhanced desorption of Ga due to high equilibrium vapor pressure of a liquid phase by formation of a eutectic system between In and Ga. Adsorbed metallic In (from pyrolyzed TMI_n) and pre-deposited metallic Ga or Ga from GaN (on the surfaces of a wafer susceptor/carrier and of surrounding surfaces in the growth chamber) form a liquid phase due to a very low eutectic temperature of ~16 °C (~289 K); thus, equilibrium vapor pressure of liquid Ga as a function of temperature will be important in desorption of Ga.

4.5.2 Equilibrium Vapour Pressure of Gallium

The equilibrium vapor pressures of Ga ($p_{eq,Ga}$) are calculated [98], assuming liquid phase of Ga on various surfaces in the chamber at different temperatures. The

Antonie equation, which describes the vapor pressure of a pure element according to the temperature, as shown in the equation (4.1), was employed to calculate the equilibrium vapor pressure of Ga.

$$\log(P / pa) = A + \frac{B}{T} + C \log(T) + \frac{D}{T^3}, \quad (4.1)$$

where P is the vapor pressure of a component, T is the temperature, and the A , B , C , and D are the coefficients for an element. The values of each coefficient for Ga employed in this calculation to obtain the Ga vapor pressure are 11.759, -13984, -0.3413, and 0 for A , B , C , and D , respectively. The Antonie equation constants for other Group-III elements commonly used in the growth of epitaxial layers are shown in Table 4.3.

Table 4.3: The Antonie equation constants for the selected Group-III elements.

Group III element	State	Constant				Temperature range
		A	B	C	D	
Al	Solid	14.464	-17342	-0.7927	0	298 K – M.P.
	Liquid	10.916	-16211	0	0	M.P. – 1800 K
Ga	Solid	11.662	-14208	0	0	298 K – M.P.
	Liquid	11.759	-13984	-0.3413	0	M.P. – 1600 K
In	Solid	10.996	-12548	0	0	298 K – M.P.
	Liquid	10.379	-12276	0	0	M.P. – 1500 K
Mg	Solid	13.494	-7813	-0.8253	0	298 K – M.P.
	Liquid	0	0	0	0	-

* Pressure unit: Pascal (pa).

* T is the temperature in Kevin (K).

* M.P. is a melting point of an element.

The temperatures for the calculation of vapor pressure are to be selected to represent surfaces of stainless-steel parts of the chamber (origin #3.2), which is maintained at 50 °C by active liquid-cooling system, quartz parts of the chamber (origin #3.1), and a wafer susceptor/carrier (origin #2), respectively. For equilibrium vapor pressures, $p_{eq,Ga}$ is estimated to be $\sim 3.05 \times 10^{-35}$ Torr at 50 °C, which is deemed to be negligible even after the formation of a liquid phase. Therefore, Ga-containing deposition on surfaces of stainless-steel parts (origin #3.1) may not be the major origin of Ga auto-incorporation. When the temperature increases, $p_{eq,Ga}$ increases significantly, for example with estimated values of $\sim 3.62 \times 10^{-10}$ Torr and $\sim 4.10 \times 10^{-8}$ Torr at 500 °C and 600 °C, respectively, which might represent the temperatures of the surfaces of quartz parts in the growth chamber. Finally, estimated $p_{eq,Ga}$ reaches at $\sim 3.67 \times 10^{-4}$ Torr at 890 °C. Considering a sticking coefficient of Ga with nearly 1 at a temperature used in this study and very low incorporation efficiencies of Al and In in the epitaxial material, this vapor pressure may not be significantly small as compared to *input* partial pressures of Group-III precursors in the growth chamber using growth parameters in this study.

4.5.3 Partial Pressure and Incorporation Efficiency of Group-III Precursors

The partial pressure of each element in the reaction chamber during the growth of an InAl(Ga)N layer was calculated from molar flow rate of each gas in the growth chamber (TMIn, TMAI, NH₃ and N₂) assuming ideal gas behavior. The ideal gas law shown in equation (4.2) was used for this calculation.

$$P_{MO}V = nRT \quad (4.2)$$

where P_{MO} is the partial pressure of Group-III and Group-V precursors, V is the volume of the MO precursor, n is number of moles. From the numerical calculation, the partial pressures of Group-III precursors injected into the reaction chamber were $p_{TMAI} = 1.96 \times 10^{-3}$ Torr and $p_{TMIn} = 3.93 \times 10^{-3}$ Torr.

Next, the incorporation efficiency (η) under the growth condition used in this study was estimated by comparing the number of Al and In atoms in an epitaxial InAlGaN film (representatively using sample C, $In_{0.04}Al_{0.54}Ga_{0.42}N$) deposited on an 8-inch-diameter susceptor/carrier to the molar flow rates of input TMAI and TMIn precursors, which can be described by following equation (4.3):

$$\eta = \frac{\text{number of Group III atoms in the grown layer}}{\text{number of Group III atoms of MO precursors}}, \quad (4.3)$$

The incorporation efficiencies of Al and In are estimated to be 18.9 % and 0.61 %, respectively. Homogeneous reaction in the gas phase and high desorption rate from the growth surface for Al and In, respectively, are responsible for very low incorporation efficiency. And then, *effective* precursor molar flow rate (for actual epitaxial growth) of each precursor was calculated from nominal input precursor molar flow rate and the estimated incorporation efficiency. Finally, the *effective* partial pressures that actually contribute to the epitaxial growth on substrates and a wafer susceptor/carrier are calculated to be $p_{TMAI} = 3.7 \times 10^{-4}$ Torr, and $p_{TMIn} = 2.4 \times 10^{-5}$ Torr, which is comparable or less than $p_{Ga} = \sim 3.67 \times 10^{-4}$ Torr (the same as equilibrium vapor pressure of liquid metal at 890 °C, assuming segregation coefficient (or incorporation efficiency) of Ga nearly 1). The results of the calculations on the equilibrium vapor pressure of Ga and the partial

pressure of Group-III precursors in the growth chamber under the growth temperature of is summarized in Table 4.4.

Table 4.4: Equilibrium vapor pressure of the Ga and the partial pressure of Group-III precursors in the reaction chamber at the growth temperature (T=890 °C) and the growth pressure (300 Torr) to grow InAl(Ga)N layer.

	TMAI	TMIn	Ga
Equilibrium vapor pressure			$\sim 3.67 \times 10^{-4}$ Torr ^{a)}
Partial pressure	1.96×10^{-3} Torr	3.93×10^{-3} Torr	
Incorporation efficiency	0.189	0.061	~ 1 ^{b)}
Effective partial pressure^{c)}	3.7×10^{-4} Torr	2.4×10^{-5} Torr	$\sim 3.67 \times 10^{-4}$ Torr

^{a)} In the case of liquid-phase Gallium

^{b)} Assuming segregation coefficient (or incorporation efficiency) of Ga is nearly 1.

^{c)} The partial pressure actually contributes to the epitaxial growth on substrate and a wafer susceptor/carrier.

4.5.4 Origins and a Mechanism of Gallium Auto-incorporation

A mechanism of Ga auto-incorporation can be deduced from the experimental results of various cases. The Ga auto-incorporation starts with In-Ga eutectic formation on Ga-containing deposition with abundant In. Next, desorption of Ga (and In) from a liquid phase from surrounding surfaces into gas-phase Ga, followed by adsorption of Ga on a growing InAlN epitaxial layer. Thus, the Ga-containing deposition on a wafer

susceptor/carrier is believed to be one of the most dominant origins of Ga auto-incorporation by its high vapor pressure due to high temperature, once the formation of liquid phase occurs by introduction of In precursor. Ga-containing deposition on quartz parts in a growth chamber is believed to be the other dominant origin of Ga auto-incorporation. For the case of deposition on quartz parts, even though vapor pressure of liquid Ga phase is significantly lower than for the case on a wafer susceptor/carrier, In-Ga eutectic formation on the surface of Ga-containing deposition on the quartz parts might be easier than for the case on a wafer susceptor/carrier due to the Ga-rich (or N-deficient) nature of Ga-containing deposition by the difference in NH₃ cracking efficiency at temperatures of the quartz parts and wafer susceptor/carrier.

4.6 Summary

The possible origins and a mechanism of Ga auto-incorporation of InAl(Ga)N epitaxial layers have been systematically investigated. It was found that the Ga-containing deposition on a wafer susceptor/carrier is the most dominant precursor for Ga auto-incorporation and the deposition on surrounding surfaces of quartz parts in a growth chamber is the other dominant source, while the effect of stainless-steel parts and interdiffusion of Ga atom from GaN underlayer are not critical. In addition, Mg or Cp₂Mg in the growth chamber during InAl(Ga)N layer growth facilitates the auto-incorporation of Ga by modifying deposition conditions of GaN on surrounding surfaces and a wafer susceptor/carrier. Based on experimental data of various cases, a mechanism for Ga auto-incorporation in InAl(Ga)N has been proposed. The mechanism includes (i) In-Ga eutectic formation on Ga-containing deposition with abundant In and (ii)

desorption of Ga (and In) from a liquid phase from surrounding surfaces into gas-phase Ga, followed by (iii) adsorption of Ga on a growing InAlN epitaxial layer with a sticking coefficient of nearly 1. Therefore, Ga-containing deposition on any hot surfaces that is also exposed to In precursor to form a liquid phase is believed to be major origins of Ga auto-incorporation. This mechanism implies the following Ga auto-incorporation behaviors in the epitaxial growth of ternary InAlN and quaternary InAlGaN materials.

- The auto-incorporation process is suspected to occur in most MOCVD and MBE reactors, unless all surfaces exposed to a Ga-containing ambient are effectively cooled below the eutectic temperature of In-Ga.
- While the auto-incorporation may not be completely suppressed in the growth of ternary InAlN layers, the incorporation can be controlled by employing the same growth parameters and chamber conditions for the wafer susceptor/carrier and surrounding surfaces.
- The auto-incorporation is expected to be more severe for growth of InAlN on a GaN layer mainly via Ga-containing deposition on a wafer susceptor/carrier and on surrounding surfaces in the growth chamber during GaN growth in the same run.
- Effects of the auto-incorporation in the growth of quaternary InAlGaN layers can be suppressed by using higher partial pressure of Ga from precursor than equilibrium vapor pressure of Ga from Ga-containing deposition and by employing the same growth chamber conditions.
- The auto-incorporation may also occur in the growth of binary InN.

CHAPTER 5

IMPROVEMENT OF EXTRACTION EFFICIENCY OF THE VISIBLE LIGHT-EMITTING DIODES

5.1 Introduction

Periodic structures of dielectric and metallic materials are a critical element in photonic crystals and other metamaterials [99,100]. Especially, 2-dimensional periodic dielectric structures have been developed for light emitting applications to modify spontaneous recombination and photon confinement or extraction [101,102]. For the proper management of generated photons in the light-emitting diodes (LEDs), confinement of photon in the naturally-formed waveguide structures has to be disturbed. Therefore, the improvement in light-extraction efficiency (LEE), while not compromising internal quantum efficiency, electrical characteristics of the diodes, and controllability and throughput of fabrication process, which are related to optical output power, wall-plug efficiency, and manufacturing cost of the LEDs, respectively, is of critical importance considering given technical and economic challenges that LED-based solid-state lighting is currently facing [64]. In efforts to enhance the LEE in the LEDs, various schemes and techniques have been developed, including patterning of substrates under the epitaxial structures [103], roughening of light-emitting surfaces [104], shaping of LED chips [105], and incorporation of photonic crystals [106]. While these approaches were applied to successfully improve the LEE of III-nitride-based visible and white LEDs, they were also accompanied by drawbacks associated with the process applied. The substrate patterning requires additional lithography and dry-etching process of sapphire

substrates prior to the epitaxial structure formation [107]. The texturing of the GaN surface is typically achieved by plasma-based dry etching or KOH-based wet-chemical etching. However, the surface texturing created by the dry etching techniques leaves radiation damages on the *p*-type surface by plasma, resulting in significant degradation of electrical properties of the diodes with non-Ohmic behavior of *p*-type electrode [77]. In the case of the wet-chemical etching, it is very difficult to form periodically arranged or designed surface features due to crystal-plane-dependent etching rates [78]. Furthermore, both etching methods require additional fabrication steps, such as additional photolithography process in the dry etching and deposition and removal of a protection layer in the wet-chemical etching [69]. The LED shaping for III-N LEDs requires the shaping of hard materials that is transparent to blue spectral range followed by wafer bonding process [108]. The photonic crystal formation has to go through electron-beam lithography followed by well-controlled plasma etching, which is the most complicated process, hence, suspected to have the lowest throughput among all the proposed approaches.

In order to achieve simple yet effective and controlled periodic surface patterning, laser interference is used for direct patterning of a semiconductor surface in this study. The laser interference patterning has been developed in the past to fabricate surface microstructures with simple and fast process [79-81]. Interferencing two or more high-power pulsed laser beams allows direct creation of surface features with well-defined periodic array of patterns not only to polymers but also to other material surfaces. While the conventional plasma dry etching and laser interference lithography method require additional steps using metal, insulator, or photoresist mask [73,75], the laser interference

ablation technique using interference of three laser beams applied in this work to semiconductor processing needs only a simple preparation step, permitting rapid fabrication of the surface patterns with high design flexibility. In addition, relatively large areas can be directly patterned in a short time by manipulating the configuration of the laser beam optics. In the present study, we report on the direct patterning by laser ablation applied in the visible LEDs that can be further applied to the formation of photonic crystals and other metamaterial periodic structures. Demonstrated LED structures with direct periodic surface patterns show negligible degradation of electrical properties of diodes as well as improved LEEs.

5.2 Growth and Fabrication of the Blue LEDs

The GaN-based blue LED structure was epitaxially grown by metalorganic chemical vapor deposition (Thomas-Swan Scientific Equipment, 6×2"). The structure on a *c*-plane (0001) sapphire substrate consists of an unintentionally-doped 1- μm -thick GaN layer (GaN:ud, $\sim 1\mu\text{m}$) an *n*-GaN:Si ($\sim 2\mu\text{m}$, $n\sim 5\times 10^{18}\text{ cm}^{-3}$), a five-period InGaN/GaN (2.5 nm/12 nm) multiple quantum well (MQW) active region, followed by a *p*-GaN:Mg layer ($\sim 200\text{ nm}$, $p\sim 7\times 10^{17}\text{ cm}^{-3}$), and finally, a heavily doped *p*-GaN:Mg⁺⁺ contact layer ($\sim 20\text{ nm}$, [Mg] $\sim 1\times 10^{20}\text{ cm}^{-3}$). A schematic illustration of the epitaxial layer structure of a blue LED is shown in Figure 5.1. The direct laser ablation for patterning was applied on the surface of *p*-type GaN layers. The laser-patterned LED epitaxial layer structure was cleaned in HCl solution for 10 min to remove the residual Ga and Ga-oxide generated during laser interference ablation [109]. A conventional LED having the same epitaxial layers but without surface patterning was also prepared for a comparative study.

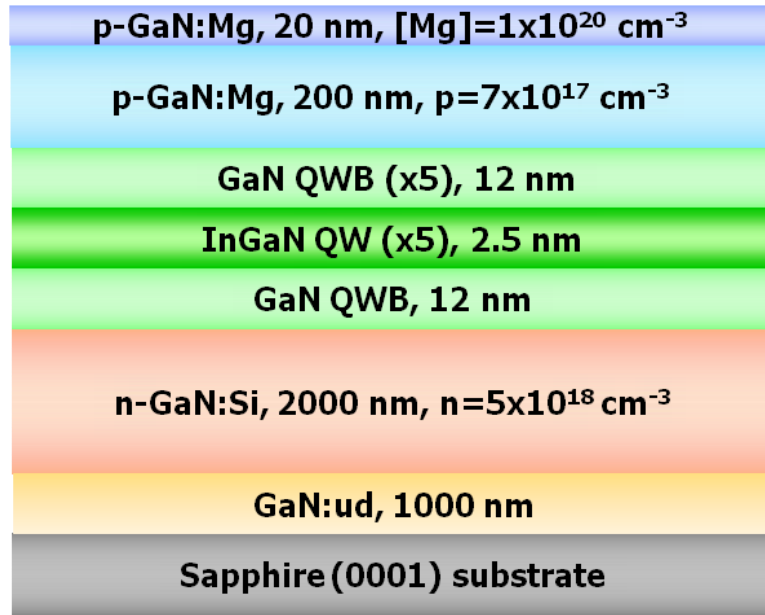


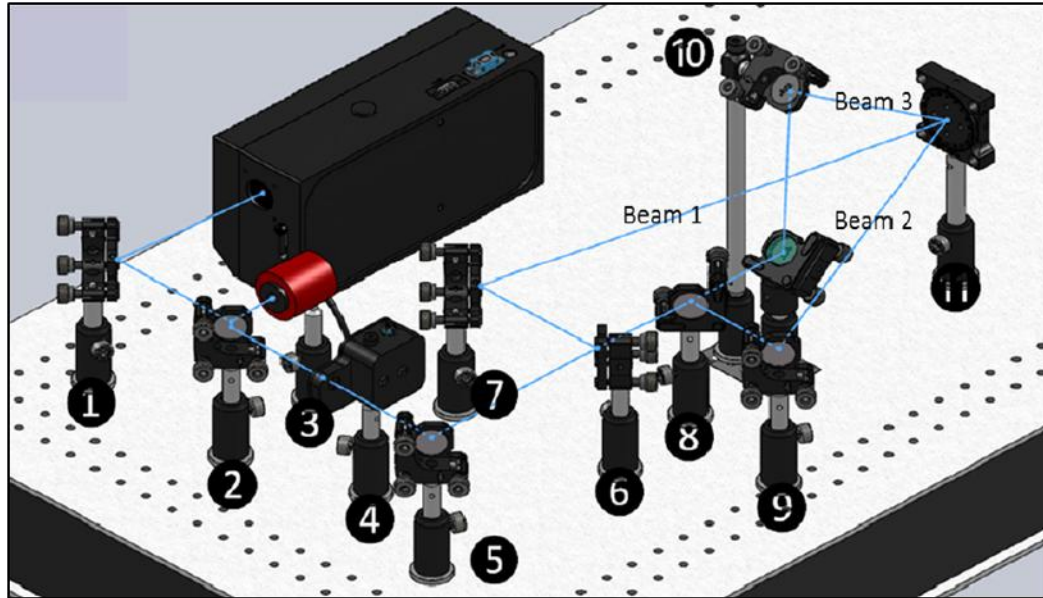
Figure 5.1: Schematic illustration of epitaxial layer structure of a blue LED.

The epitaxial structures of both LEDs with and without surface patterning were fabricated into LED chips having a mesa size of $350 \times 350 \mu\text{m}^2$ by mesa definition using inductively-coupled plasma reactive-ion etching. Ti/Al/Ti/Au and Ni/Au metal films were deposited for *n*-type and transparent *p*-type electrodes by e-beam evaporation, respectively, followed by metallization annealing. A bond pad was deposited on the *p*-type electrode but no additional current spreading layer was applied. Scanning electron microscope (SEM) and atomic force microscopy (AFM) were taken to identify the surface profile of the *p*-GaN of the laser-patterned LEDs. Electrical property of the LEDs depending on the surface patterning was compared by measuring current–voltage (*I*–*V*) characteristics. In addition, transmission line measurement (TLM) was performed for 1 μm -thick *p*-GaN layers separately prepared with and without three-beam interference laser ablation to study the type conversion and degraded contact resistance by the laser

interference ablation process. Electroluminescence (EL) measurement was to compare light-extraction efficiencies between patterned and non-patterned LED structures. Monte-Carlo ray-tracing simulation was conducted for the theoretical confirmation of enhanced light extraction by the surface patterning.

5.3 Direct Surface Patterning by Three-beam Interference Laser Ablation

The schematic configuration of the three-beam interference laser ablation setup is shown in Figure 5.2. For laser interference ablation, a high-power pulsed Nd:YAG laser (Quanta-Ray PRO 290, Spectra Physics) was used. The surface of the LED epitaxial layer structure was irradiated by the laser beam at $\lambda=266$ nm harmonic wavelength with a pulse width of 10 ns and repetition rate of 10 Hz. The primary laser beam was split into three beams by a 67 % and a 50 % reflection beam splitters which are (#6) and (#8), respectively, in the Figure 5.2, to interfere with each other on the surface of the sample (#11). The laser power was systematically adjusted through the laser controller and monitored by a high-damage-threshold power meter (#3). The diameter of the initial laser beam was expanded to 10 mm through beam expansion optics, allowing patterning over areas of approximately 0.78 cm^2 . Exposure time and the number of laser pulses irradiated on the sample were controlled by a mechanical shutter (Uniblitz Electronic VS25S2ZMO) (#4). Further details on the setup of the three-beam interference laser ablation process used in this study and the theoretical background are well discussed in one of previous reports [110].



- ① ⑤ ⑦ ⑨ ⑩ Reflection mirrors
- ② Reflection beam splitter (10 %) for monitoring laser power
- ③ High threshold power meter
- ④ Mechanical shutter
- ⑥ Reflection beam splitter (67 %)
- ⑧ Reflection beam splitter (50 %)
- ⑪ Sample holder

Figure 5.2: Schematic illustration of the configuration for the three-beam interference laser ablation [110].

5.4 Surface Characterization of the Laser-patterned LEDs

The scanning electron microscopy (SEM) image of the *p*-GaN surface of the laser-patterned LED is shown in Figure 5.3.

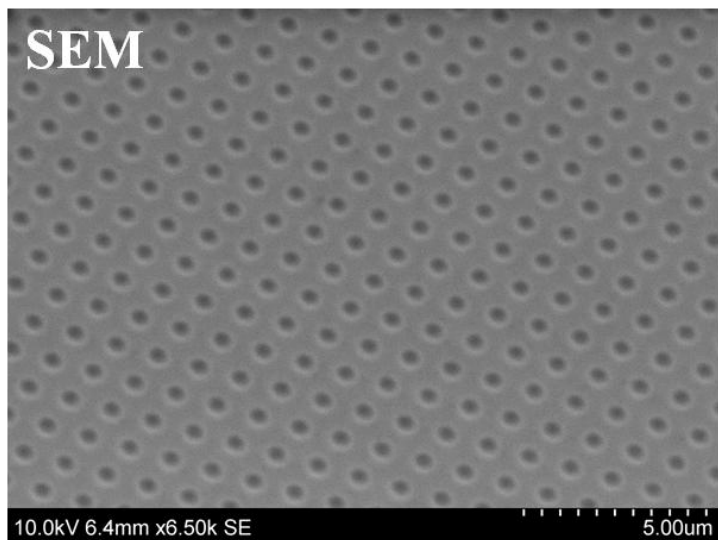


Figure 5.3: Surface image of the laser-patterned LED; showing periodic array of 2-dimensional pattern measured by SEM.

The direct irradiation of the laser leads to thermal decomposition of the LED surface according to the laser fluence into gaseous nitrogen and metallic Ga residue. The interference of three laser beams separated by two plate beam splitters results in a periodic intensity distribution on the irradiated surface, enabling the ablation of selective areas on the LED epitaxial layer structure surface, so that the resulting surface can have periodic array of circular-hole patterns with six-fold rotational symmetry. The patterned *p*-GaN surface of the laser-patterned LED is also characterized by atomic-force microscopy (AFM) as shown in Figure 5.4(a) and (b).

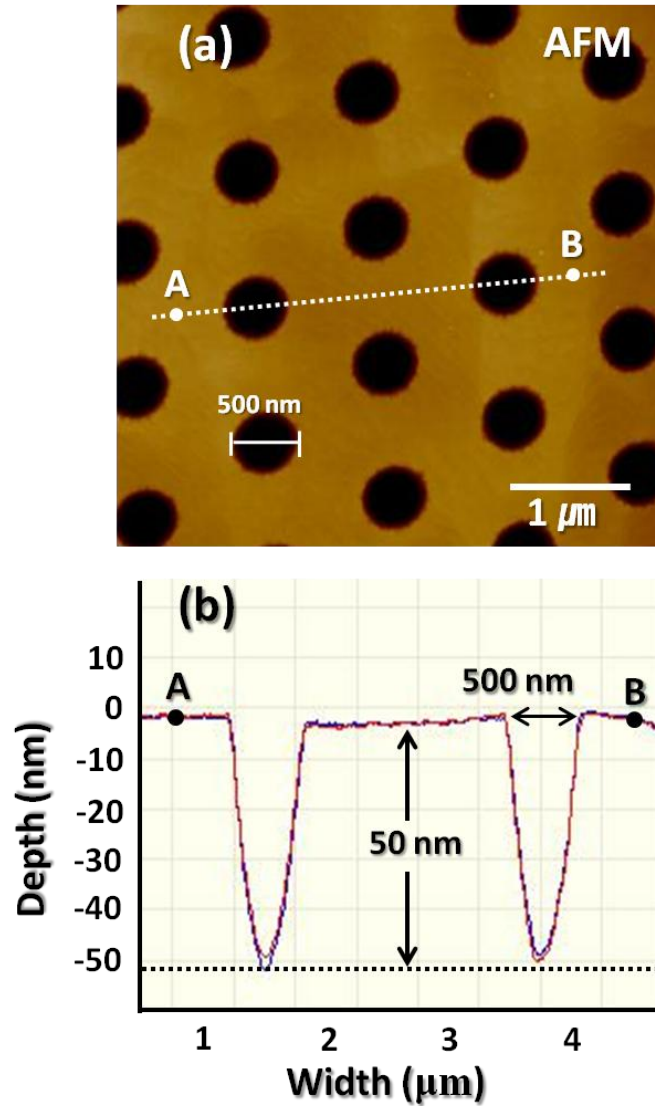


Figure 5.4: (a) Surface image and (b) depth profile of the laser-patterned LED; showing inverted-cone-shaped holes at the top p-GaN layer measured by AFM.

The ablated holes were measured to be the same opening diameter of approximately 500 nm and a periodicity of 1 μm, and no surface defects/features were observed on non-patterned areas, as shown in Figure 5.3 and 5.4(a). In addition, surface scans performed by AFM, as representatively shown in Figure 5.4(b), confirms the profile of patterned holes, which is inverted cone shape having the ablation depth of

approximately 50 nm. The topographical structure of the resulting surface comprising 2-D hexagonal hole array was formed inversely to the corresponding laser intensity distribution. The intensity distribution, $I(x,y)$ of the three-beam interference, and the period (P) of the 2-dimensional (2-D) hexagonal lattice array are described by equation (5.1) and (5.2), respectively [110]:

$$I(x, y) = I_{laser} + \frac{2}{3} I_{laser} \times \left[\begin{aligned} &\cos\left(k \sin \theta \left(-\frac{3}{2}x + \frac{\sqrt{3}}{2}y\right)\right) + \cos\left(k \sin \theta \left(-\sqrt{3}y\right)\right), \\ &+ \cos\left(k \sin \theta \left(\frac{3}{2}x + \frac{\sqrt{3}}{2}y\right)\right) \end{aligned} \right], \quad (5.1)$$

and

$$P = \frac{\lambda}{\sqrt{3} \sin \theta}, \quad (5.2)$$

where I_{laser} is the laser fluence, k is the wave vector, θ is the angle of the beams with respect to the vertical axis, and λ is the wavelength of light. Since the intensity distribution of the three-beam laser interference is sinusoidal profile during exposure, the resulting hole has inverted cone shape, which will improve photon extraction from the p -GaN surface by modifying critical angle as well as enlarging the effective surface area for photons to be escaped. In addition, when $I(x,y) = I_{th}$ and $y=0$, x is the ablation radius due to the central symmetry. Thus, the diameter of the ablated area (D_{hole}) is given by

following equation (5.3):

$$D_{hole} = \frac{4}{3k \sin(\theta)} \arccos\left(\frac{3I_{th}}{4I_{laser}} - \frac{5}{4}\right). \quad (5.3)$$

The periodicity and hole diameter are strong function of angle of the beam from the surface normal when the wavelength of the laser is fixed. In this laser ablation, laser beam angle and intensity were controlled, considering hole depth as well as hole diameter and periodicity. Especially the depth of holes has to be optimized not only to improve the LEE but also not to affect optical quality of visible InGaN/GaN MQW active region [84], which is located about 200 nm away from the surface by thermal and other degradation during the laser ablation. The periodicity and depth, changed by simple manipulation of laser beam in this three-beam interference set up, also suggest that photonic lattice can be implemented relatively easily without extensive effort in fabrication processes. Moreover, the rapid fabrication of the 2-D hole array on relatively large area of *p*-GaN surface was accomplished by the three-beam interference laser ablation without additional photolithography and dry etching processes. Additionally, only single exposure of three-beam interference of high-energy nanosecond laser was required to generate periodic 2-D patterns on the *p*-GaN surface. The extra steps, rotation or movement of wafer stage or laser source along *x-y* plane, are inevitable in the two-beam interference laser ablation or laser beam writing techniques [75,81,111]. The direct three-beam interference laser ablation can avoid the additional manipulation of geographical configurations leading to extra process steps and time; and hence no compromised process yield and throughput.

5.5 Electrical Characterization of Laser-patterned LEDs

Current–voltage (I – V) characteristics of the laser-patterned LEDs and non-patterned (conventional) LEDs were measured, as shown in Figure 5.5. The forward voltages at an injection current of 20 mA were similar at ~ 3.7 V for both laser-patterned and conventional LEDs. While the turn-on voltage and the slope of I – V plot up to 4 V were similar, the laser-patterned LEDs had a slightly higher series resistance ($R_s = dV/dI$) than the conventional LEDs at the voltages exceeding 4 V, showing $R_s \sim 16 \Omega$ and 12Ω for the laser-patterned LEDs and the conventional LEDs, respectively.

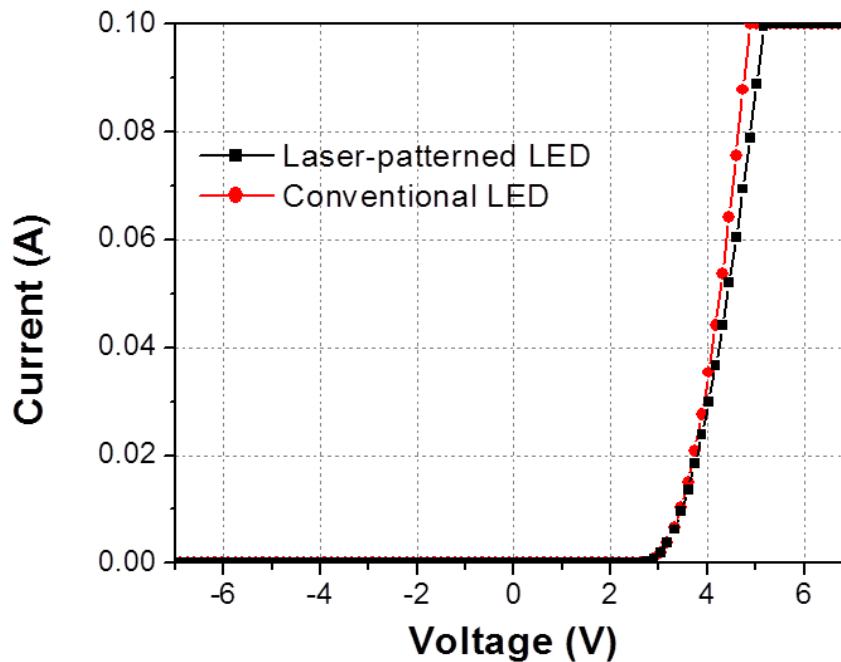


Figure 5.5: The current-voltage (I – V) measurement results of the laser-patterned LED and the conventional (non-patterned) LED.

Even though there is a slight increase in series resistance, this I - V characteristics of periodic patterned LEDs in the current study is significantly better than other periodically patterned LEDs [112,113]. In addition, this increase in series resistance for the laser-patterned LEDs is believed to be a result of compromised current spreading by locally reduced thickness in the p -GaN layer, but not the result of degraded Ohmic contact.

To further study specific contact resistance (r_c) and sheet resistance (R_{sh}) contributed to the I - V characteristics and also to investigate the possible degradation of the materials by the laser interference ablation process and corresponding degradation of electrical property of the p -GaN:Mg layer, the transmission line measurement (TLM) using a linear-pattern geometry was performed. Mesa definition for TLM patterns was defined on 1 μ m-thick p -GaN:Mg layer without p -GaN:Mg⁺⁺ metal contact layer. The elimination of the contact layer was intended to have the metal contact on the same p -type surfaces for both patterned and non-patterned areas. The p -GaN layer was grown with the same growth condition including doping concentration as the p -GaN layer in the LEDs compared in this study. The TLM results of the p -GaN layers with and without surface patterning generated by three-beam interference laser ablation are plotted in Figure 5.6.

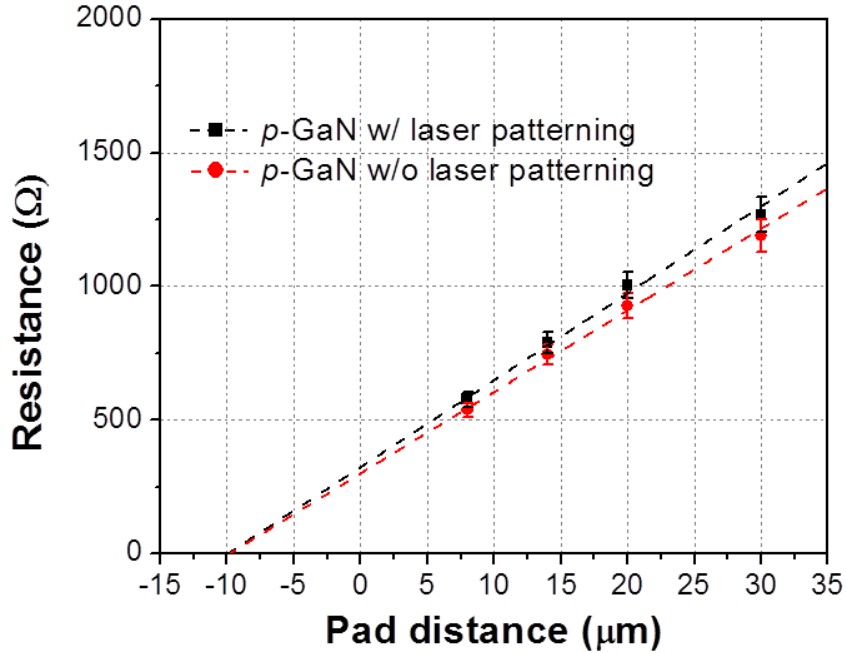


Figure 5.6: The TLM plot for the laser-patterned LED and the conventional (non-patterned) LED.

Both the metal/*p*-GaN layers with and without surface pattern show Ohmic contact behavior (no Schottky barrier) having similar linearity and values. The R_{sh} and the r_c were $7.125 \times 10^3 \Omega/\square$ and $1.183 \times 10^{-3} \Omega\text{-cm}^2$ for the laser-patterned *p*-GaN layer and $6.540 \times 10^3 \Omega/\square$ and $1.177 \times 10^{-3} \Omega\text{-cm}^2$ for the non-patterned *p*-GaN layer, respectively. The increased sheet resistance in the case of laser-patterned *p*-GaN layer is due to locally reduced thickness in the layer by patterning. The contact resistances are, however, nearly identical for both cases and this results strongly suggests that Ohmic contact properties were not affected by direct laser interference ablation. This data provide additional benefit of this direct laser interference ablation method, in addition to simple process for high process yield and throughput, over previously reported patterning techniques, which mostly resulted in type-conversion of *p*-type surface followed by degraded Ohmic contact

properties by plasma damage [77]. In fact, most previous reports on surface patterning by dry-etching, especially for photonic-crystal LEDs, show degradation of electrical properties by Ohmic contact problems [114]. However, the electrical properties of patterned p -GaN layer of laser-patterned LEDs are expected to be uncompromised by three-beam interference laser ablation. Slightly higher series resistance for the LEDs with laser-patterning is believed to be due to increased sheet resistance by locally reduced thickness by patterning in the p -GaN layer, as the depth of the holes is nearly 1/4 of the total p -type layer thickness, which can be mitigated easily by slight device structure modification.

5.6 Device Electroluminescence Measurement Results

For the improvement in light-output characteristics by three-beam interference laser patterning, the electroluminescence (EL) measurement was performed. The EL intensities of wafer-level (without packaging) devices were measured from the top p -GaN surface with and without surface patterning. The light output–current (L – I) characteristics for laser-patterned and conventional LEDs are compared in Figure 5.7.

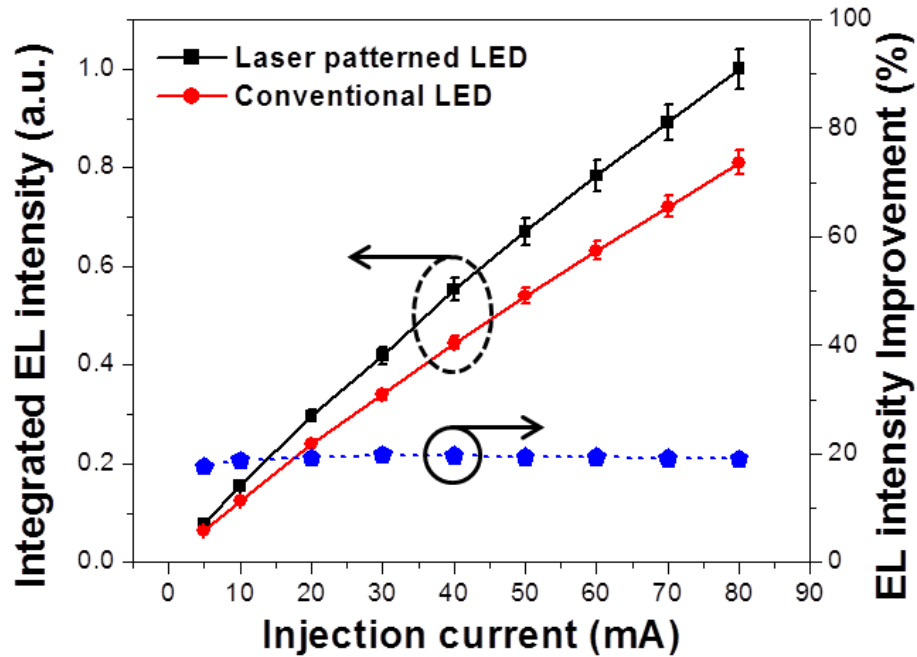


Figure 5.7: Plots of the integrated EL intensity according to injection current for the laser-patterned LED and the conventional LED.

As shown in Figure 5.7, while the EL intensities for both LEDs increase monotonously as the driving current increased from 5 mA to 80 mA, the EL intensity of laser-patterned LEDs exceeds that observed from the conventional LEDs. The patterning on the top *p*-GaN surface resulted in an improvement in light output power by 20 % for all injection current regimes (blue dotted line in Figure 5.7), indicating that the laser-patterned LEDs have higher LEE than the conventional LEDs. The comparison of the EL spectra of the laser-patterned LED and conventional LED at the injection current of 80 mA is also shown in Figure 5.8.

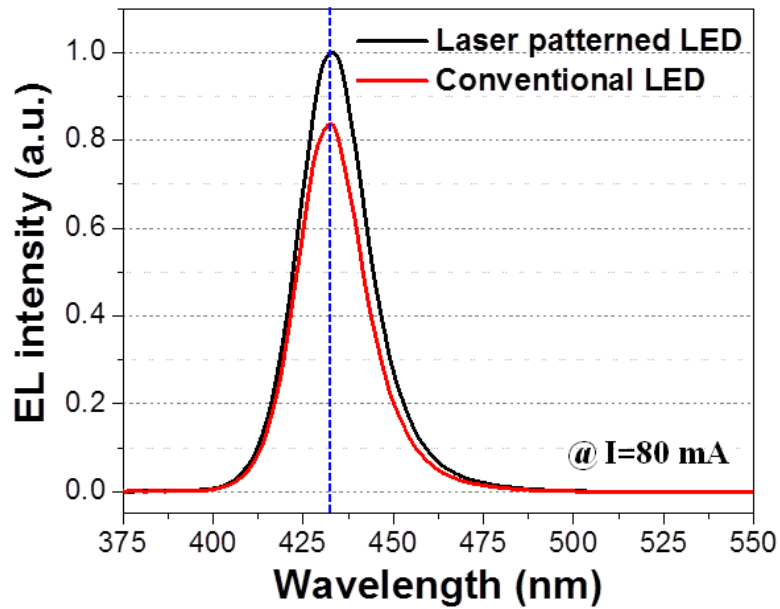


Figure 5.8: Comparison of the EL spectra at an injection current of $I=80$ mA for the laser-patterned LED and the conventional LED.

In the Figure 5.8, both EL spectra have the same peak emission wavelengths of $\lambda \sim 430$ nm as well as showing the EL intensity of laser-patterned LED is approximately 20 % higher than that of conventional LED, confirming no change after surface patterning by three-beam interference laser ablation on the *p*-GaN surface. The improvement of optical property of a blue LED after surface texturing was also confirmed by photoluminescence (PL) measurement as compared in Figure 5.9(a) and (b).

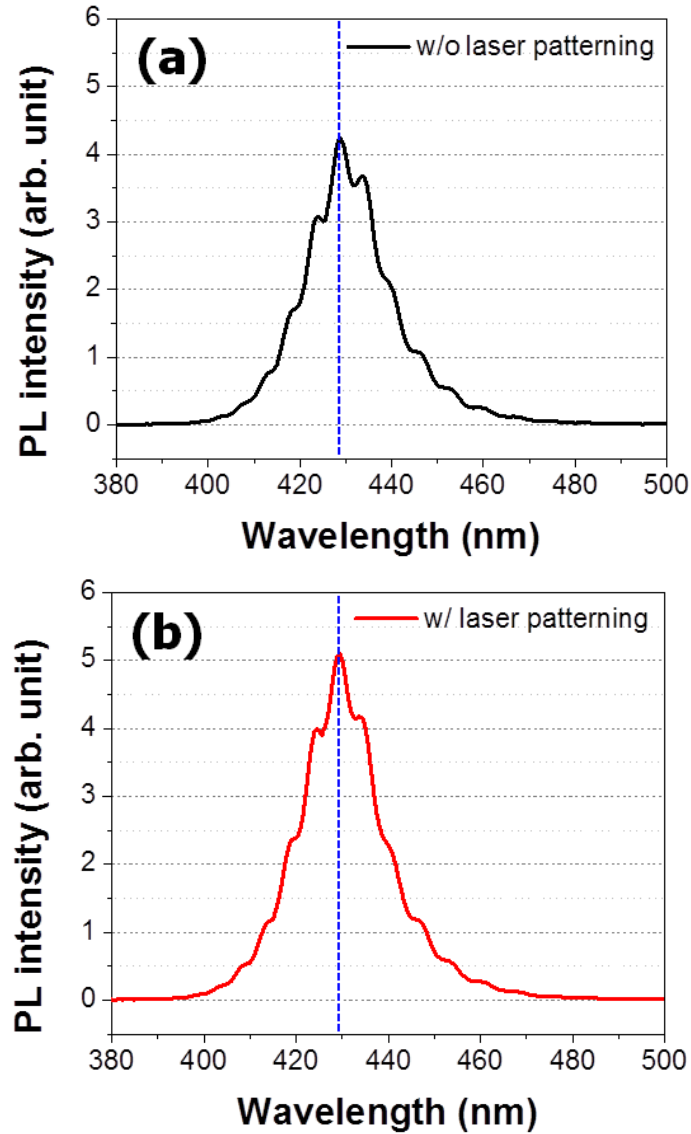


Figure 5.9: Photoluminescence (PL) spectra for (a) the laser-patterned LED and (b) the conventional LED.

The PL intensity of laser-patterned LEDs was 19 % higher than that of conventional LEDs while the peak emission wavelengths of $\lambda \sim 430$ nm for both LEDs were similar. These observations suggest that the three-beam interference laser ablation treatment on the top *p*-GaN surface successfully generated periodic array of surface

microstructures without significant damages to the MQW active region, and the enhancement of LEE was responsible for the surface texturing of the laser-patterned LEDs.

5.7 Theoretical Confirmation of the Enhanced Light-extraction Efficiency

To theoretically confirm the enhanced photon extraction through the *p*-GaN surface of the laser-patterned LED, Monte-Carlo ray-tracing simulations were implemented using the LIGHTTOOLS modeling software. As the periodicity of the pattern in this study is larger than periodicity to have photonic bandgap in visible spectrum [115], ray-tracing simulation will serve the purpose enough. The results of ray-tracing simulations for laser-patterned LED and conventional LED are compared in Figure 5.10(a), (b), and (c).

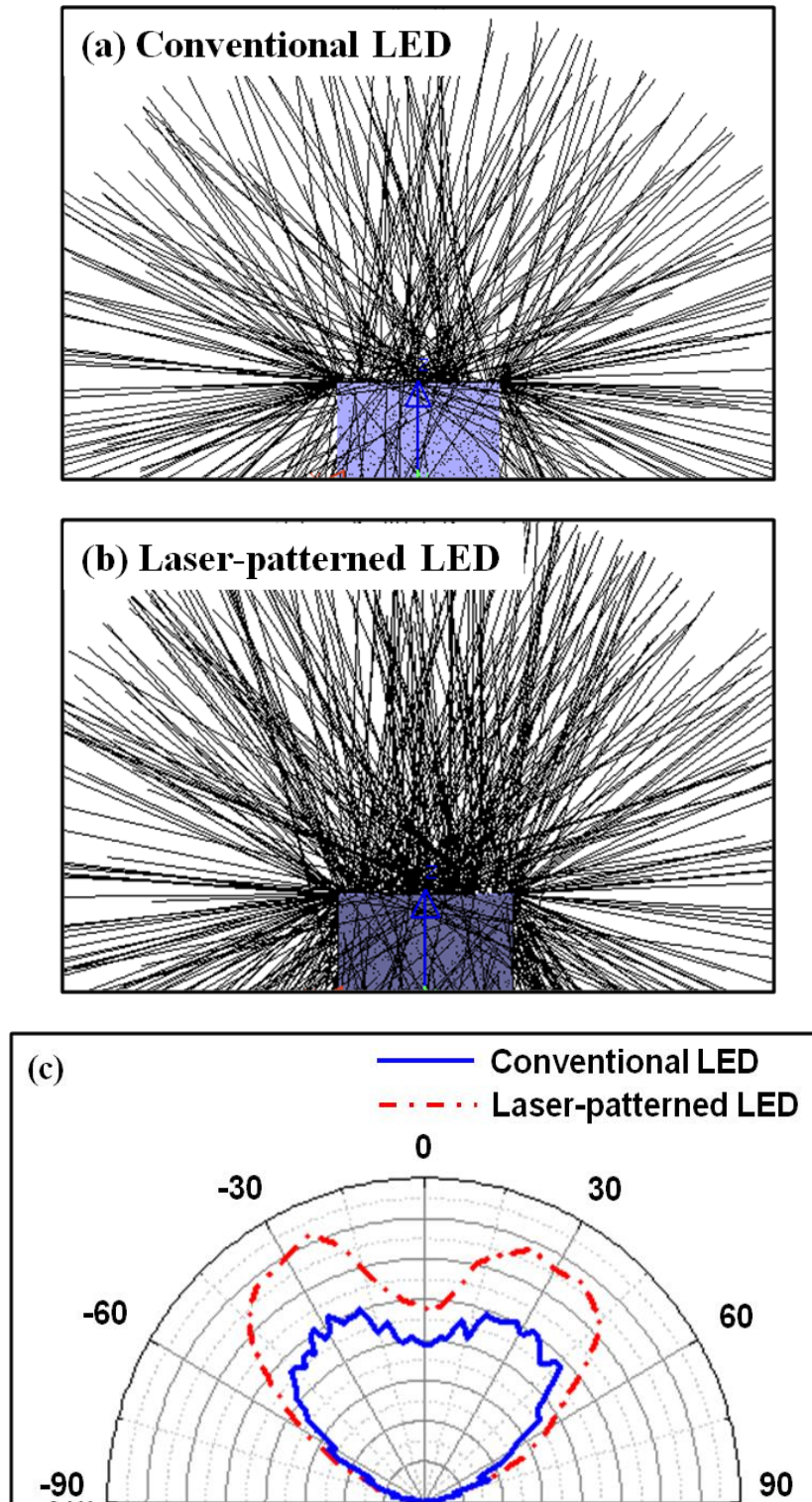


Figure 5.10: Cross-sectional ray-tracing views of (a) conventional LED and (b) laser-patterned LED, and (c) Far-field patterns of LEDs with and without surface texture calculated by Monte-Carlo ray-tracing simulation.

The cross-sectional ray-tracing views of laser-patterned LED and conventional LED, as shown in Figure 5.10(a) and (b), show that the photons, generated from the MQW active region, more effectively escape from the LED with periodic surface patterns in *p*-GaN than from the conventional LED without periodic patterns. In particular, the light is more efficiently extracted from the top side of the LED with periodic surface texture, as shown in Figure 5.10(c). Based on simulation results, the light extraction efficiency of laser-patterned LED was improved by 19.5 %, compared to that of conventional LED. This improvement of light extraction from the laser-patterned LED obtained by theoretical simulation well agreed with experimental result. Therefore, it is convinced that the enhancement of light output power of laser-patterned LED is attributed to the increase in extraction efficiency by surface patterning, while the internal quantum efficiency of both LEDs are same due to no degradation in MQW active region by direct laser interference ablation.

5.8 Summary

The periodic array of surface patterns on the top surface of GaN-based visible LEDs was fabricated by three-beam interference laser ablation method without deterioration of electrical property of *p*-type layer and optical properties of MQW active region. The 2-dimensional hexagonal lattice array of surface patterns were simply generated by direct irradiation of the laser source which is interference of three laser beams on the top *p*-GaN surface. The experimental results showed about 20 % improved LEE of the laser-patterned LED structure. Furthermore, the theoretical calculation using Monte-Carlo ray-tracing simulation confirmed the enhancement of LEE of the laser-

patterned LED structure. The laser interference ablation technique using three or more laser beams can offer the possibility to realize homogenous microstructures having complex patterns on the large surface area. In addition, this method can be expanded for the formation of photonic crystals in visible spectrum and shorter wavelength spectrum without complication of electron-beam lithography.

CHAPTER 6

RESEARCH SUMMARY

For several decades, group-III-nitride semiconductors have drawn enormous attention as practicable materials in a variety of semiconductor optoelectronic devices such as laser diodes (LDs), light-emitting diodes (LEDs), and photodiodes (PDs) due to the advantages of wide and direct energy bandgap, superior thermal and chemical stability even at elevated temperature, and capability of forming heterostructure. The development of the epitaxial layer growth by using metalorganic chemical vapour deposition (MOCVD) technique enables the III-nitride based photonic and electronic devices to have the high-quality epitaxial layer structure with high throughput and flexibility of the epitaxial layer growth. Moreover, various kinds of analysis and characterization techniques have been developed and utilized for the growth of high-quality epitaxial layers. Therefore, the performance of the optoelectronic devices based on the III-nitride semiconductor materials has been dramatically improved, resulting in a great success in commercialization.

One of the most successful achievements in the optoelectronic devices based on III-nitride semiconductor materials is LEDs regarded as the most promising candidate for replacing the conventional light sources in displays and general lighting in the near future. While the peak luminous efficiencies of LED-based lamps far exceed those of incandescent and fluorescent lamps at relatively low currents, the efficiencies of LED lamps at high currents diminish with increasing drive currents. This efficiency droop poses a major technical challenge for LED lamps used in high power lighting. Although

several possible mechanisms have been suggested, the origin of the efficiency droop still remains in dispute. However, most of the discussions on the efficiency droop in III-nitride LEDs point out the importance of the carrier injection into the active region, the distribution of carriers across the active region, and densities of carriers in the QWs. For example, the effect of the EBL and leakage current is related to the carrier injection, Auger recombination becomes dominant at high carrier density in the QWs, and carrier delocalization from the localized states is related to the carrier density in the QWs. Therefore, achieving high carrier injection followed by uniform distribution of the carriers may be a key issue to identify and resolve the efficiency droop.

The hole injection and transport in MQW active regions have been described in this work. The effect on the hole transport in the active region and resulting hole distribution among the MQWs was experimentally studied by controlling the indium (In) mole fraction in *p*-type $\text{In}_x\text{Ga}_{1-x}\text{N}:\text{Mg}$ layers of the LED structures. The employment of the special design of dual- and triple-wavelength-emitting MQW active region allowed tracing the hole distribution across the active region because each QW emits its own characteristic wavelength that can be used to experimentally evaluate the transport and distribution of holes in the active region. It was found that the holes are preferentially injected into the QW adjacent to the *p*-type layer with lower In-mole-fraction *p*- $\text{In}_x\text{Ga}_{1-x}\text{N}:\text{Mg}$ layer. Enhanced hole transport with increasing In mole fraction in the *p*- $\text{In}_x\text{Ga}_{1-x}\text{N}:\text{Mg}$ layer was shown by analyzing the EL spectra. The improved hole transport and corresponding uniform distribution were achieved presumably by potential barrier near *p*-type layer and MQW active region. This is because the holes injected into the MQW active region achieve kinetic energy depending on the potential barrier between the last

GaN QW barrier and the p -type $\text{In}_x\text{Ga}_{1-x}\text{N}:\text{Mg}$ layer, resulting in a hole transport favorable environment in the MQW active region. At the same time, the hindered hole injection due to the potential barrier for hole can be overcome under high injection conditions.

Recently, the InAlN ternary wide-bandgap semiconductor material is widely used in the GaN-based visible LED structures as an alternative high quality electron blocking layer instead of the conventional AlGaIn layer because of the possibility to grow epitaxial layers that are lattice-matched to the GaN layer, resulting in higher electron confinement effect. While growth and characterization of $\text{In}_x\text{Al}_{1-x}\text{N}$ materials with various growth parameters have been studied for various applications, since high-quality and accurately-controlled InAlN epitaxial material growth has been challenging, fundamental understandings on the InAlN materials and epitaxial growth processes are still lacking. In addition, the possible unintentional incorporation of gallium (Ga) has been recently reported during the epitaxial growth of the InAlN layers by both metalorganic chemical vapor deposition (MOCVD) and molecular beam epitaxy (MBE), and the origins and a mechanism of Ga auto-incorporation in the InAl(Ga)N layers have not been identified.

The InAl(Ga)N epitaxial layers that were intended to be InAlN layers have been systematically investigated to identify the possible origins and a mechanism of Ga auto-incorporation of the InAl(Ga)N epitaxial layers in the MOCVD system. It was found that the Ga-containing deposition on a wafer susceptor/carrier is the most dominant precursor for Ga auto-incorporation and the deposition on surrounding surfaces of quartz parts in a growth chamber is the other dominant source, while the effect of stainless-steel parts and interdiffusion of Ga atom from GaN underlayer are not critical. In addition, Mg or

Cp_2Mg in the growth chamber during InAl(Ga)N layer growth facilitates the auto-incorporation of Ga by modifying deposition conditions of GaN on surrounding surfaces and a wafer susceptor/carrier. Based on experimental data of various cases, a mechanism for Ga auto-incorporation in InAl(Ga)N has been proposed. The mechanism includes (i) In-Ga eutectic formation on Ga-containing deposition with abundant In and (ii) desorption of Ga (and In) from a liquid phase from surrounding surfaces into gas-phase Ga, followed by (iii) adsorption of Ga on a growing InAlN epitaxial layer with a sticking coefficient of nearly 1. Therefore, Ga-containing deposition on any hot surfaces that are also exposed to In precursor to form a liquid phase is believed to be major origins of Ga auto-incorporation.

The 2-dimensional periodic dielectric structures have been developed for light emitting applications to modify spontaneous recombination and photon confinement or extraction. For the proper management of generated photons in the LEDs, confinement of photon in the naturally-formed waveguide structures has to be disturbed. Therefore, the improvement in light-extraction efficiency (LEE), while not compromising internal quantum efficiency, electrical characteristics of the diodes, and controllability and throughput of fabrication process, which are related to optical output power, wall-plug efficiency, and manufacturing cost of the LEDs, respectively, is of critical importance considering given technical and economic challenges that LED-based solid-state lighting is currently facing. In an effort to enhance the LEE in the LEDs, direct surface patterning on a LED structure by employing a laser interference ablation technique has been studied in this dissertation. The 2-dimensional hexagonal lattice array of surface patterns on the top surface of GaN-based visible LEDs was simply fabricated by three-beam interference

laser ablation method without deterioration of electrical property of p -type layer and optical properties of MQW active region. The experimental results showed approximately 20 % improved LEE of the laser-patterned LED structure. Furthermore, the theoretical calculation using Monte-Carlo ray-tracing simulation confirmed the enhancement of LEE of the laser-patterned LED structure. The laser interference ablation technique using three or more laser beams can offer the possibility to realize homogenous microstructures having complex patterns on the large surface area.

REFERENCES

- [1] C. Y. Yeh *et al.*, “Zinc-blende-Wurtzite polytypism in semiconductors,” *Phys. Rev. B*, vol.46, pp.10086, (1992).
- [2] A. Belabbes *et al.*, “Electronic properties of polar and nonpolar InN surfaces: A quasiparticle picture,” *Phys. Rev. B*, vol. 85(11), pp. 115121, (2012).
- [3] W. Paszkowicz *et al.*, “Rietveld-refinement study of aluminium and gallium nitrides,” *J. Alloys Compd.*, vol. 382(1-2), pp. 100–106, (2004).
- [4] *Handbook of Nitride Semiconductors and Devices.*, Vol.1; ed. Hadis Morkoc, WILEY-VCH Verlag GmbH & Co, KGaA, Weinheim, ISBN: 978-3-527-40837-5; pp.1–1311, (2008).
- [5] K. M. Yu *et al.*, “On the crystalline structure, stoichiometry and band gap of InN thin films,” *Appl. Phys. Lett.*, vol. 86(7), pp. 071910-1–2, (2005).
- [6] E. Sakalauskas *et al.*, “Dielectric function and bowing parameters of InGaN alloys,” *Phys. Stat. Sol. (b)*, vol. 249(3), pp. 485–488, (2012).
- [7] P. G. Moses *et al.*, “Band bowing and band alignment in InGaN alloys,” *Appl. Phys. Lett.*, vol. 96(2), pp. 021908-1–3, (2010).
- [8] W. G. Breiland *et al.*, “Organometallic vapor phase epitaxy (OMVPE),” *Mat. Sci. Eng. R*, vol. 24(6), pp. 241–274, (1999).
- [9] H. M. Manasevit, “Single-Crystal Gallium Arsenide on Insulating Substrates,” *Appl. Phys. Lett.* vol. 12, pp. 156–159, (1968).
- [10] R. D. Dupuis *et al.*, “High-efficiency GaAlAs/GaAs heterostructure solar cells grown by metalorganic chemical vapor deposition,” *Appl. Phys. Lett.*, vol. 31, pp. 201, (1977).
- [11] R. D. Dupuis *et al.*, “Room-temperature laser operation of quantum-well Ga_{1-x}Al_xAs-GaAs laser diodes grown by metalorganic chemical vapor deposition,” *Appl. Phys. Lett.*, vol. 32, pp. 295, (1978).
- [12] H. Amano *et al.*, “Metalorganic vapor phase epitaxial growth of a high quality GaN film using an AlN buffer layer,” *Appl. Phys. Lett.*, vol. 48, pp. 353, (1986).
- [13] H. Amano *et al.*, “p-type conduction in Mg-doped GaN treated with low-energy electron beam irradiation (LEEBI),” *Jpn. J. Appl. Phys.*, vol. 28, pp. L2112, (1989).

- [14] S. Nakamura and T. Mukai, "High-Quality InGaN Films Grown on GaN Films," *Jpn. J. Appl. Phys.*, vol. 31, pp. L1457, (1992).
- [15] R. F. Davis *et al.*, "Epitaxial growth of gallium nitride," *Aip. Conf. Proc.*, vol. 916, pp. 520–540, (2007).
- [16] A. A. Efremov *et al.*, "Effect of the Joule Heating on the Quantum Efficiency and Choice of Thermal Conditions for High-Power Blue InGaN/GaN LEDs," *Semiconductor*, vol. 40, no. 5, pp. 605–610, (2006).
- [17] T. Mukai *et al.*, "Characteristics of InGaN-based UV/Blue/Green/Amber/Red Light-Emitting Diodes," *Jpn. J. Appl. Phys.*, vol. 38, no. 7A, pp. 3976–3981, (1999).
- [18] A. Y. Kim *et al.*, "Performance of High-Power AlInGaN Light Emitting Diodes," *phys. stat. sol. (a)*, vol. 188, no. 1, pp. 15–21, (2001).
- [19] M. F. Schubert *et al.*, "Effect of dislocation density on efficiency droop in GaInN/GaN light-emitting diodes," *Appl. Phys. Lett.*, vol. 91(23), pp. 231114-1–3, (2007).
- [20] Y. C. Shen *et al.*, "Auger recombination in InGaN measurement by photoluminescence," *Appl. Phys. Lett.*, vol. 91(14), pp. 141101-1–3, (2007).
- [21] N. F. Gardner *et al.*, "Blue-emitting InGaN-GaN double-heterostructure light-emitting diodes reaching maximum quantum efficiency above 200 A/cm²," *Appl. Phys. Lett.*, vol. 91(24) pp. 243506-1–3, (2007).
- [22] K. T. Delaney *et al.*, "Auger recombination rates in nitrides from first principles," *Appl. Phys. Lett.*, vol. 94(19), pp. 191109-1–3, (2009).
- [23] J. Hader *et al.*, "On the importance of radiative and Auger losses in GaN-based quantum wells," *Appl. Phys. Lett.*, vol. 92(26), pp. 261103-1–3, (2008).
- [24] A. Laubsch *et al.*, "On the origin of IQE-‘droop’ in InGaN LEDs," *phys. Stat. sol. (c)*, vol. 6, no. S2, pp. S913–S916, (2009).
- [25] E. Kioupakis *et al.*, "Indirect Auger recombination as a cause of efficiency droop in nitride light-emitting diodes," *Appl. Phys. Lett.*, vol. 98(16), pp. 161107-1–3, (2011).
- [26] I. V. Rozhansky *et al.*, "Analysis of processes limiting quantum efficiency of AlGaInN LEDs at high pumping," *phys. Stat. sol. (a)*, vol. 204, no. 1, pp. 227–230, (2007).
- [27] M. H. Kim *et al.*, "Origin of efficiency droop in GaN-based light-emitting diodes," *Appl. Phys. Lett.*, vol. 91(18), pp. 183507-1–3, (2007).

- [28] M. F. Schubert *et al.*, “Polarization-matched GaInN/AlGaInN multi-quantum-well light-emitting diodes with reduced efficiency droop,” *Appl. Phys. Lett.*, vol. 93(4), pp. 041102-1–3, (2008).
- [29] J. P. Liu, *et al.*, “Barrier effect on hole transport and carrier distribution in InGaN/GaN multiple quantum well visible light-emitting diodes,” *Appl. Phys. Lett.*, vol. 93, pp. 021102-1–3, (2008).
- [30] X. Ni *et al.*, “Reduction of efficiency droop in InGaN light emitting diodes by coupled quantum wells,” *Appl. Phys. Lett.*, vol. 93, pp. 171113-1–3, (2008).
- [31] J.-H. Ryou, *et al.*, “Control of quantum-confined Stark effect in InGaN-based quantum wells,” *IEEE J. Select. Topic. Quantum Electron.*, vol. 15, pp. 1080–1091, (2009).
- [32] D. Zhu, *et al.*, “Enhanced electron capture and symmetrized carrier distribution in GaInN light-emitting diodes having tailored barrier doping,” *Appl. Phys. Lett.*, vol. 96, pp. 121110-1–3, (2010).
- [33] C. H. Wang, *et al.*, “Efficiency droop alleviation in InGaN/GaN light-emitting diodes by graded-thickness multiple quantum wells,” *Appl. Phys. Lett.*, vol. 97, pp. 181101-1–3, (2010).
- [34] S. H. Han, *et al.*, “Improvement of efficiency droop in InGaN/GaN multiple quantum well light-emitting diodes with trapezoidal wells,” *J. Phys. D: Appl. Phys.*, vol. 43, pp. 354004-1–5, (2010).
- [35] Y. K. Kuo *et al.*, “Advantages of InGaN light-emitting diodes with GaN-InGaN-GaN barriers,” *Appl. Phys. Lett.*, vol. 99, pp. 091107-1–3, (2011).
- [36] A. R. Vasconcellos *et al.*, “Hot-phonon bottleneck in the photoinjected plasma in GaN,” *Appl. Phys. Lett.*, vol. 82(15), no. 15, pp. 2455–2457, (2003).
- [37] S. Chichibu *et al.*, “Exciton localization in InGaN quantum well devices,” *J. Vac. Sci. Technol. B*, vol. 16, pp. 2204–2214, (1998).
- [38] B. Monemar *et al.*, “Defect related issues in the “current roll-off” in InGaN based light emitting diodes,” *Appl. Phys. Lett.*, vol. 91(18), pp. 181103-1–3, (2007).
- [39] T. Peng *et al.*, “Band gap bowing and refractive index spectra of polycrystalline $\text{Al}_x\text{In}_{1-x}\text{N}$ films deposited by sputtering,” *Appl. Phys. Lett.*, vol. 71(17), pp. 2439–2441, (1997).
- [40] M. Ferhat *et al.*, “First-principles calculations of gap bowing in $\text{In}_x\text{Ga}_{1-x}\text{N}$ and $\text{In}_x\text{Al}_{1-x}\text{N}$ alloy: Relation to structural and thermodynamic properties,” *Phys. Rev. B*, vol. 65, pp. 075213, (2002).

- [41] S.Yu. Karpov *et al.*, “Statistical model of ternary group-III nitrides,” *Phys. Rev. B*, vol. 70, pp. 235203-1–10, (2004).
- [42] K. Driscoll *et al.*, “Optically pumped intersubband emission of short-wave infrared radiation with GaN/AlN quantum wells,” *Appl. Phys. Lett.*, vol. 94(8), pp. 081120-1–3, (2009).
- [43] J.-F. Carlin *et al.*, “Crack-free fully epitaxial nitride microcavity using highly reflective AlInN/GaN Bragg mirrors,” *Appl. Phys. Lett.*, vol. 86(3), pp. 031107-1–3, (2005).
- [44] E. Feltn *et al.*, “Crack-free highly reflective AlInN/AlGaIn Bragg mirrors for UV applications,” *Appl. Phys. Lett.*, vol. 88, pp. 051108-1–3, (2006).
- [45] Md.M. Satter *et al.*, “Design and Analysis of 250-nm AlInN Laser Diodes on AlN Substrates Using Tapered Electron Blocking Layers,” *IEEE J Quantum Electron.*, vol. 48, pp. 703, (2012).
- [46] S. Choi *et al.*, “Improvement of peak quantum efficiency and efficiency droop in III-nitride visible light-emitting diodes with an InAlN electron-blocking layer,” *Appl. Phys. Lett.*, vol. 96, pp. 221105-1–3, (2010).
- [47] H.J. Kim *et al.*, “Improvement of quantum efficiency by employing active-layer-friendly lattice-matched InAlN electron blocking layer in green light-emitting diodes,” *Appl. Phys. Lett.*, vol. 96, pp. 101102-1–3, (2010).
- [48] S. Choi *et al.*, “Efficiency droop due to electron spill-over and limited hole injection in III-nitride visible light-emitting diodes employing lattice-matched InAlN electron blocking layers,” *Appl. Phys. Lett.*, vol. 101, pp. 161110-1–5, (2012).
- [49] J. Kuzmik *et al.*, “InAlN/(In)GaIn high electron mobility transistors: some aspects of the quantum well heterostructure proposal,” *Semicon. Sci. Technol.*, vol. 17, pp. 540–544, (2002).
- [50] S. Choi *et al.*, “Threshold voltage control of InAlN/GaN heterostructure field-effect transistors for depletion- and enhancement-mode operation,” *Appl. Phys. Lett.*, vol. 96, pp. 243506-1–3, (2010).
- [51] T. Matsuoka *et al.*, “Calculation of unstable mixing region in wurtzite $\text{In}_{1-x-y}\text{Ga}_x\text{Al}_y\text{N}$,” *Appl. Phys. Lett.*, vol. 71, pp. 105, (1971).
- [52] J.M. Manuel *et al.*, “Structural and compositional homogeneity of InAlN epitaxial layers nearly lattice-matched to GaN,” *Acta Mater.*, vol. 58, pp. 4120–4125, (2010).

- [53] Q.Y. Wei *et al.*, “Compositional instability in InAlN/GaN lattice-matched epitaxy,” *Appl. Phys. Lett.*, vol. 100, pp. 092101-1–3, (2012).
- [54] B.-T. Liou *et al.*, “Vegard’s law deviation in band gap and bowing parameter of $\text{Al}_x\text{In}_{1-x}\text{N}$,” *Appl. Phys. A*, vol. 81, pp. 651, (2005).
- [55] K. Lorenz *et al.*, “Anomalous Ion Channeling in AlInN-GaN Bilayers: Determination of the Strain State,” *Phys. Rev. Lett.*, vol. 97, pp. 085501, (2006).
- [56] T. Fujimori *et al.*, “Growth and characterization of AlInN on AlN template,” *J. Crystal Growth*, vol. 272, pp. 381–385, (2004).
- [57] C. Hums *et al.*, “Metal-organic vapor phase epitaxy and properties of AlInN in the whole compositional range,” *Appl. Phys. Lett.*, vol. 90, pp. 022105-1–3, (2007).
- [58] T.S. Oh *et al.*, “Growth and properties of Al-rich $\text{In}_x\text{Al}_{1-x}\text{N}$ ternary alloy grown on GaN template by metalorganic chemical vapour deposition,” *J. Phys. D: Appl. Phys.*, vol. 41, pp. 095402, (2008).
- [59] G. Liu *et al.*, “Metalorganic vapor phase epitaxy and characterizations of nearly-lattice-matched AlInN alloys on GaN/sapphire templates and free-standing GaN substrates,” *J. Crystal Growth*, vol. 340, pp. 66–75, (2012).
- [60] D.G. Zhao *et al.*, “Parasitic reaction and its effect on the growth rate of AlN by metalorganic chemical vapor deposition,” *J. Crystal Growth*, vol. 289, pp. 72–75, (2006).
- [61] H.J. Kim *et al.*, “Modulated precursor flow epitaxial growth of AlN layers on native AlN substrates by metal-organic chemical vapor deposition,” *Appl. Phys. Lett.*, vol. 93, pp. 022103-1–3, (2008).
- [62] J. Gillespie *et al.*, “Ultra Thin Barrier Layers for mmW Frequencies in III-N HEMT Technologies,” *Compound Semiconductor Manufacturing Technology (CS-MANTECH) Conference*, pp. 181–183, (2010).
- [63] S. Guo *et al.*, “AlInN HEMT grown on SiC by metalorganic vapor phase epitaxy for millimeter-wave applications,” *Phys. Stat. Sol. (a)*, vol. 207, pp. 1348, (2010).
- [64] J.-H. Ryou and R. D. Dupuis, “Focus Issue Introduction: Optics in LEDs for lighting,” *Opt. Express*, vol. 19(S4), pp. A897–A899, (2011).
- [65] C. Huh *et al.*, “Improved light-output and electrical performance of InGaN-based light-emitting diode by microroughening of the p-GaN surface,” *J. Appl. Phys.*, vol. 93(11), pp. 9383–9385, (2003).

- [66] S. F. Yu *et al.*, “Characteristics of InGaN-based Light-Emitting Diodes on Patterned Sapphire Substrates with Various Pattern Heights,” *J. Nano.* vol. 2012, pp. 1–6, (2012).
- [67] T. Fujii *et al.*, “Increase in the extraction efficiency of GaN-based Light-emitting diodes via surface roughening,” *Appl. Phys. Lett.*, vol. 84(6), pp. 855–857, (2004).
- [68] S. Chhajed *et al.*, “Strong light extraction enhancement in GaInN light-emitting diodes by using self-organized nanoscale patterning of p-type GaN,” *Appl. Phys. Lett.*, vol. 98(7), pp. 071102, (2011).
- [69] J. K. Kim *et al.*, “Elimination of total internal reflection in GaInN light-emitting diodes by graded-refractive-index micropillars,” *Appl. Phys. Lett.*, vol. 93(22), pp. 22111, (2008).
- [70] W. C. Peng and Y. S. Wu, “Enhanced performance of an InGaN-GaN light-emitting diode by roughening the undoped-GaN surface and applying a mirror coating to the sapphire substrate,” *Appl. Phys. Lett.*, vol. 88(18), pp. 181117, (2006).
- [71] H. W. Huang *et al.*, “Enhanced light output of an InGaN/GaN light emitting diode with a nano-roughened p-GaN surface,” *Nanotechnology*, vol. 16, pp. 1844–1848, (2005).
- [72] K. T. Lee *et al.*, “Improvement on optical properties of GaN light-emitting diode with mesh-textured sapphire back delineated by laser scribe,” *IEEE Photon. Technol. Lett.*, vol. 21(7), pp. 477–479, (2009).
- [73] S. M. Pan *et al.*, “Improvement of InGaN-GaN light-emitting diodes with surface-textured indium-tin-oxide transparent ohmic contacts,” *IEEE Photon. Technol. Lett.*, vol. 15(5), pp. 649–651, (2003).
- [74] X. H. Huang *et al.*, “High-efficiency InGaN-based LEDs grown on patterned sapphire substrates,” *Opt. Express*, vol. 19(14), pp. 949–955, (2011).
- [75] D. H. Kim *et al.*, “Enhanced light extraction from GaN-based light-emitting diodes with holographically generated two-dimensional photonic crystal patterns,” *Appl. Phys. Lett.*, vol. 87(20), pp. 203508, (2005).
- [76] Z. Zuo *et al.*, “Increasing the extraction efficiency of blue light emitting diodes via laser patterned Ga-polar p-GaN surface,” *Phys. Stat. Sol. (a)*, vol. 208(9), pp. 2226–2230, (2011).

- [77] X. A. Cao *et al.*, “Electrical effects of plasma damage in p-GaN,” *Appl. Phys. Lett.*, vol. 75(17), pp. 2569–2571, (1999).
- [78] Y. Gao *et al.*, “Roughening hexagonal surface morphology on laser lift-off (LLO) N-face GaN with simple photo-enhanced chemical wet etching,” *Jpn. J. Appl. Phys.* vol. 43, pp. L637–L639, (2004).
- [79] A. Lasagni *et al.*, “Advanced design of periodical architectures in bulk metals by means of Laser Interference Metallurgy,” *Applied Surface Science*, vol. 254, pp. 930–936, (2007).
- [80] A. Lasagni *et al.*, “Rapid fabrication of pentaerythritol triacrylate periodic structures on large areas by laser interference patterning with nanosecond pulses,” *J. Appl. Phys.*, vol. 105(2), pp. 023101, (2009).
- [81] D. Yuan *et al.*, “Heteroepitaxial patterned growth of vertically aligned and periodically distributed ZnO nanowires on GaN using laser interference ablation,” *Adv. Funct. Mater.*, vol. 20, pp. 3484–3489, (2010).
- [82] Available: <http://www.laytec.de> (02/2014).
- [83] B. E. Warren, *X-ray Diffraction*. Reading, Massachusetts: Addison-Wesley Pub. Co., (1969).
- [84] W. Lee *et al.*, “Effect of thermal annealing induced by p-type layer growth on blue and green LED performance,” *J. Cryst. Growth*, vol. 287, pp. 577, (2006).
- [85] J. Limb *et al.*, “Comparison of GaN and $\text{In}_{0.04}\text{Ga}_{0.96}\text{N}$ p-Layers on the Electrical and Electroluminescence Properties of Green Light Emitting Diodes,” *J. Electron. Mater.*, vol. 36, pp. 426–430, (2007).
- [86] J. H. Ryou *et al.*, “Control of quantum-confined Stark effect in InGaN/GaN multiple quantum well active region by p-type layer for III-nitride-based visible light emitting diodes,” *Appl. Phys. Lett.*, vol. 92, pp. 101113-1–3, (2008).
- [87] E.-H. Park *et al.*, “The effect of silicon doping in the selected barrier on the electroluminescence of InGaN/GaN multiquantum well light emitting diode,” *Appl. Phys. Lett.*, vol. 90, pp. 031102-1–3, (2006).

- [88] J.-H. Ryou *et al.*, “Effect of silicon doping in the quantum well barriers on the electrical and optical properties of visible green light emitting diodes,” *IEEE Photon. Technol. Lett.*, vol. 20, pp. 1769–1771, (2008).
- [89] J. Zhang and N. Tansu, “Improvement in spontaneous emission rates for InGaN quantum wells on ternary InGaN substrate for light-emitting diodes,” *J. Appl. Phys.*, vol. 110, pp. 113110-1–5, (2008).
- [90] M. Suzuki and T. Uenoyama, “Electronic and optical properties of GaN-based quantum wells,” in *Group III Nitride Semiconductor Compounds: Physics and Applications*, B. Gil, Ed. New York: Oxford University Press, pp. 307–341, (1998).
- [91] H. Y. Lin *et al.*, “Direct evidence of compositional pulling effect in $\text{Al}_x\text{Ga}_{1-x}\text{N}$ epilayers,” *J. Crystal Growth*, vol. 290, pp. 225–228, (2006).
- [92] S. Zhou *et al.*, “Chemical composition and elastic strain in AlInGaN quaternary films,” *Thin Solid Films*, vol. 515, pp. 1429–1432, (2006).
- [93] S. Choi *et al.*, “Actual temperatures of growing surfaces of III-nitride-based materials depending on substrates and forced convection conditions in metal organic chemical vapor deposition,” *J. Appl. Phys.*, vol. 106, pp. 073512-1–6, (2009).
- [94] F. Brunner *et al.*, “Growth optimization during III-nitride multiwafer MOVPE using real-time curvature, reflectance and true temperature measurements,” *J. Crystal Growth*, vol. 298, pp. 202–206, (2007).
- [95] J. J. Zhu *et al.*, “Contribution of GaN template to the unexpected Ga atoms incorporated into AlInN epilayers grown under an indium-very-rich condition by metalorganic chemical vapor deposition (MOCVD),” *J. Crystal Growth*, vol. 348, pp. 25–30, (2012).
- [96] H. Xing *et al.*, “Memory Effect and Redistribution of Mg into Sequentially Regrown GaN Layer by Metalorganic Chemical Vapor Deposition,” *Jpn. J. Appl. Phys.*, vol. 42, pp. 50–53, (2003).
- [97] M. Notin *et al.*, “New experimental results and improvement of the modelization of the (Ga,Mg) system,” *J. Alloy. Comp.*, vol. 176, pp. 25–38, (1991).
- [98] C. B. Alcock *et al.*, “Vapor Pressure of the Metallic Elements,” *Can. Metall. Q.*, vol. 23, pp. 309–313, (1984).
- [99] E. Yablonovitch, “Inhibited spontaneous Emission in Solid-State Physics and Electronics,” *Phys. Rev. Lett.*, vol. 58, pp. 2059–2062, (1987).

- [100] Q. Xu *et al.*, “Fabrication of Large-Area Patterned Nanostructures for Optical Applications by Nanoskiving,” *Nano Lett.*, vol. 7, pp. 2800–2805, (2007).
- [101] M. Fujita *et al.*, “Simultaneous Inhibition and Redistribution of Spontaneous Light Emission in Photonic Crystals,” *Science*, vol. 308, pp. 1296–1298, (2005).
- [102] O. Painter *et al.*, “Two-Dimensional Photonic Band-Gap Defect Mode Laser,” *Science*, vol. 284, pp. 1819–1821, (1999).
- [103] K. Tadatomo *et al.*, “High Output Power InGaN Ultraviolet Light-Emitting Diodes Fabricated on Patterned Substrates Using Metalorganic Vapor Phase Epitaxy,” *Jpn. J. Appl. Phys.*, vol. 40, pp. L583–L585, (2001).
- [104] I. Schnitzer *et al.*, “30% external quantum efficiency from surface textured, thin-film light-emitting diodes,” *Appl. Phys. Lett.*, vol. 63, pp. 2174–2176, (1993).
- [105] M. R. Krames *et al.*, “High-power truncated-inverted-pyramid $(\text{Al}_x\text{Ga}_{1-x})_{0.5}\text{In}_{0.5}\text{P}/\text{GaP}$ light-emitting diodes exhibiting >50% external quantum efficiency,” *Appl. Phys. Lett.*, vol. 75, pp. 2365–2367, (1999).
- [106] S. Fan *et al.*, “High Extraction Efficiency of Spontaneous Emission from Slabs of Photonic Crystals,” *Phys. Rev. Lett.*, vol. 78, pp. 3294–3297, (1997).
- [107] M. Yamada *et al.*, “InGaN-Based Near-Ultraviolet and Blue-Light-Emitting Diodes with High External Quantum Efficiency Using a Patterned Sapphire Substrate and a Mesh Electrode,” *Jpn. J. Appl. Phys.*, vol. 41, pp. L1431–L1433, (2002).
- [108] A. Murai *et al.*, “Hexagonal pyramid shaped light-emitting diodes based on ZnO and GaN direct wafer bonding,” *Appl. Phys. Lett.*, vol. 89, pp. 171116-1–3, (2006).
- [109] C. F. Chu *et al.*, “Study of GaN light-emitting diodes fabricated by laser lift-off technique,” *J. Appl. Phys.*, vol. 95, pp. 3916–3922, (2004).
- [110] D. Yuan *et al.*, “The fabrication of vertically aligned and periodically distributed carbon nanotube bundles and periodically porous carbon nanotube films through a combination of laser interference ablation and metal-catalyzed chemical vapor deposition,” *Nanotechnology*, vol. 23, pp. 215303-1–8, (2012).
- [111] J. T. Chen *et al.*, “Laser-induced periodic structures for light extraction efficiency enhancement of GaN-based light emitting diodes,” *Opt. Express*, vol. 20(5), pp. 5689–5695, (2012).
- [112] T. N. Oder *et al.*, “III-nitride blue and ultraviolet photonic crystal light emitting diodes,” *Appl. Phys. Lett.*, vol. 84, pp. 466–468, (2004).

- [113] J. J. Wierer *et al.*, “InGaN/GaN quantum-well heterostructure light-emitting diodes employing photonic crystal structures,” *Appl. Phys. Lett.*, vol. 84, 3885–3887, (2004).
- [114] J. Y. Kim *et al.*, “Enhancement of light extraction from GaN-based green light-emitting diodes using selective area photonic crystal,” *Appl. Phys. Lett.*, vol. 96, pp. 251103-1–3 (2010).
- [115] A. Barra *et al.*, “Visible Light Control by GaN Photonic Band Gaps,” *Phys. Stat. Sol. (a)*, vol. 176, pp.747–749, (1999).

VITA

Jeomoh Kim was born in Jeonju, South Korea. He received his B.S degree in Metallurgical Engineering from Chonbuk National University, South Korea. He also received his M.S degree in Material and Science Engineering from Gwangju Institute of Science and Technology, South Korea. Currently, he is working towards his Ph.D. degree in Electrical and Computer Engineering at Georgia Institute of Technology, under the supervision of Professor Russell Dean Dupuis. His research interests include growth and characterization of III-nitride based electronic and photonic devices. He has authored and coauthored over 15 technical journal papers and 30 conference presentations, in the field of growth and characterization of semiconductor materials and devices.